



Terms and Conditions of Use of Digitised Theses from Trinity College Library Dublin

Copyright statement

All material supplied by Trinity College Library is protected by copyright (under the Copyright and Related Rights Act, 2000 as amended) and other relevant Intellectual Property Rights. By accessing and using a Digitised Thesis from Trinity College Library you acknowledge that all Intellectual Property Rights in any Works supplied are the sole and exclusive property of the copyright and/or other IPR holder. Specific copyright holders may not be explicitly identified. Use of materials from other sources within a thesis should not be construed as a claim over them.

A non-exclusive, non-transferable licence is hereby granted to those using or reproducing, in whole or in part, the material for valid purposes, providing the copyright owners are acknowledged using the normal conventions. Where specific permission to use material is required, this is identified and such permission must be sought from the copyright holder or agency cited.

Liability statement

By using a Digitised Thesis, I accept that Trinity College Dublin bears no legal responsibility for the accuracy, legality or comprehensiveness of materials contained within the thesis, and that Trinity College Dublin accepts no liability for indirect, consequential, or incidental, damages or losses arising from use of the thesis for whatever reason. Information located in a thesis may be subject to specific use constraints, details of which may not be explicitly described. It is the responsibility of potential and actual users to be aware of such constraints and to abide by them. By making use of material from a digitised thesis, you accept these copyright and disclaimer provisions. Where it is brought to the attention of Trinity College Library that there may be a breach of copyright or other restraint, it is the policy to withdraw or take down access to a thesis while the issue is being resolved.

Access Agreement

By using a Digitised Thesis from Trinity College Library you are bound by the following Terms & Conditions. Please read them carefully.

I have read and I understand the following statement: All material supplied via a Digitised Thesis from Trinity College Library is protected by copyright and other intellectual property rights, and duplication or sale of all or part of any of a thesis is not permitted, except that material may be duplicated by you for your research use or for educational purposes in electronic or print form providing the copyright owners are acknowledged using the normal conventions. You must obtain permission for any other use. Electronic or print copies may not be offered, whether for sale or otherwise to anyone. This copy has been supplied on the understanding that it is copyright material and that no quotation from the thesis may be published without proper acknowledgement.

Electronic Structure Study of Defects and Impurities in Oxide Semiconductors



Aurab Chakrabarty
School of Physics
Trinity College Dublin

A thesis submitted for
the Doctor of Philosophy in Physics

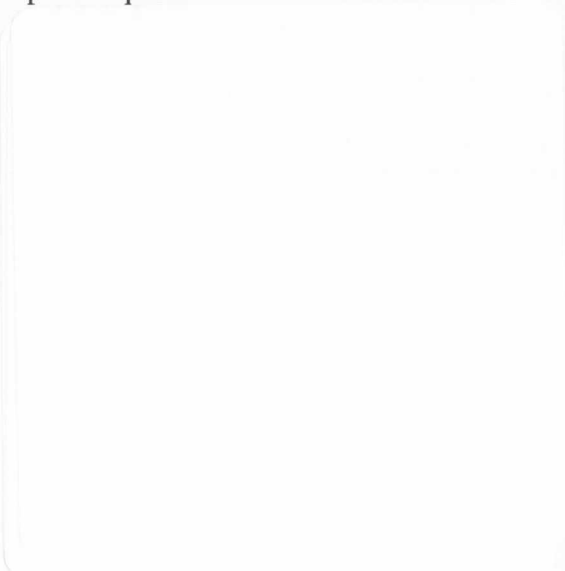
March 26, 2012



Thesis 9608

Declaration

I hereby declare that,

- a. This thesis has not been submitted as an exercise for a degree at this or any other University,
 - b. It is entirely my own work done with the help of the persons acknowledged here,
 - c. I agree that the Library may lend or copy the thesis upon request.
- 

I would like to dedicate this thesis to Nandini Kajuri whose caring guidance and love helped me all the way through my scientific career.

Acknowledgements

I would like to thank my supervisor Prof. Charles H. Patterson for his continuous effort and useful advice. His important guidance is the key ingredient to bring this report to the present condition. I also thank Dr. Satheesh Krishnamaurthy, Dr. Cormac McGuinness, Prof. J. M. D. Coey and Prof. Paul Attfield for useful discussions and Prof. Robert C. Barklie for EPR figures. I would like to acknowledge Trinity Centre for High Performance Computing (TCHPC) and Irish Centre for High End Computing (ICHEC) for the computer time provided. I convey my gratitude to Dr. Thomas Archer, Dr. Roman Kováčik, Mr. Jimmy Tang and Gilles Civario for technical supports and my group member and friend Ciaran McNamee for continuous support. I am thankful to my loving friends Anindya Mukherjee, Arnab Bhattacharya, Debadutta Deb, Kapildeb Dolui and Dr. Viviana Marzaioli for continuous encouragement and for being at my side through all ups and downs of my journey. I convey my regards to Dr. Shibshekhar Roy and Swagata Banerjee for their help and support.

I express a very special gratitude to my friends Bidraha Bagh and Dr. Partha Pratim Jana for being the 'role model' and passing important advices from across two continents.

Abstract

In this work, the crystal and electronic structures of defects and impurities in ZnO and Fe₃O₄ are studied using first principles calculations. B3LYP hybrid density-functional theory calculations were used with supercell method to evaluate electronic structures and formation energies of intrinsic vacancy defects oxygen (V_O), zinc (V_{Zn}) and zinc-oxygen pair (V_{ZnO}) vacancies. The magnetic exchange couplings of well-separated, singly negatively charged defects were also calculated and were found to be induced by a conduction band electron when the defect levels are partially filled, more than half-filling. Partially filled defects (above half-filling) with a large and positive Hubbard- U show a ferromagnetic interaction in a range exceeding 10 Å. Using this observation, an attempt is made to explain defect-related ferromagnetism observed in ZnO. The formation energies and the transition levels were estimated for oxygen (V_O), zinc (V_{Zn}) and zinc-oxygen pair (V_{ZnO}) vacancies in various charge states. Different methods were considered in the calculation of transition levels and Hubbard- U . A total energy method and a single particle eigenvalue method were applied to estimate the vacancy defect transition levels. A quantitative comparison has been made between the two methods. Relaxation of crystal structure was found to affect the formation energy and transition level values and was deemed necessary for estimating these quantities. Some literature values of U and the values obtained here with unrelaxed defect geometry are positive and large but U values are strongly dependent on relaxation. For all the three vacancies U becomes negative upon relaxation. The long-standing problem of anomalous photoluminescence observed in non-stoichiometric ZnO thin films was addressed by estimating the optical transition energies.

The electronic properties of Fe_3O_4 are governed by mixed valence hopping between Fe^{2+} - Fe^{3+} ions in its insulating phase at low temperature. Electronic structure calculations were carried out to study the effect of hole doping in magnetite using its low temperature lattice structure. Li-ferrite ($\text{Li}_{0.5}\text{Fe}_{2.5}\text{O}_4$) was found in some experiment to have a moderate band-gap semiconductor with large FM moment and is investigated here. First principles calculations predict that the small band-gap is due to the mixed valence hopping. This is quenched by dilute hole doping and is eliminated totally in $\text{Li}_{0.5}\text{Fe}_{2.5}\text{O}_4$. Substituting oxygen with nitrogen in Fe_3O_4 yields similar results with Li-doping. Small polaron states are observed upon hole doping in which holes localise at particular sites.

Contents

1	Introduction	1
1.0.1	Intrinsic defects in ZnO	5
1.0.2	Acceptor doped magnetite	10
2	Defects in oxide semiconductors: A brief literature review	12
2.1	Characterisation of vacancy defects	15
2.1.1	EPR and PAS studies of electron traps	16
2.1.1.1	Negative U defects	22
2.1.2	Role of defects in optical properties: Photoluminescence	23
2.1.3	First-principles calculations on oxide defects	23
2.2	Defect related ferromagnetism in oxides	28
2.2.1	The Magnetic Polaron and Impurity Band-Exchange Models	28
2.2.2	Hubbard model: Room temperature ferromagnetism	30
3	Computational Methods	35
3.1	Hartree-Fock and Density Functional Theory	35
3.1.1	Hartree Fock Theory	36
3.1.2	Density Functional Theory	38
3.2	B3LYP hybrid DFT functional	40
3.3	The CRYSTAL code	42
3.3.1	Localised orbital <i>vs.</i> plane-wave basis sets	44
3.4	The EXCITON code	45

4	Estimation of Defect Formation Energies and Transition Levels	47
4.1	Defect and impurity formation Energy	47
4.2	Defect transition levels	49
4.2.1	Transition level calculation using total energy	50
4.2.2	Transition level from single-particle eigenvalues	52
4.3	Computational errors and correction schemes	55
4.3.1	Effect of periodic boundary condition	55
4.3.2	Effect of relaxation	59
4.3.3	Effect of k-point sampling and basis sets	59
5	Intrinsic Vacancy Defects and Impurities in ZnO: Electronic and Crystal Structure	61
5.1	Electronic structure of the defects	64
5.1.1	Oxygen vacancy V_O	64
5.1.2	Zinc vacancy V_{Zn}	67
5.1.3	ZnO pair vacancy V_{ZnO}	68
5.1.4	Clustered vacancy defect V_{ZnO_3}	75
5.2	Effect of relaxation of crystal structure.	75
5.3	Impurity doping in ZnO	76
5.3.1	Transition metal doping	76
5.3.2	Electron doping with aluminum co-doping	80
5.4	Conclusion	81
6	Calculation of Defect Formation Energies, Transition Levels and Hubbard-U values	82
6.1	Formation energies	83
6.2	Defect transition levels	89
6.2.1	Transition levels from single particle eigenvalues	94
6.3	Calculation of Hubbard U	97
6.4	Conclusion	101

7	Interaction of Defect-trapped Electrons, Transition Metal Doping	102
7.0.1	Magnesium oxide (MgO)	108
7.1	Implication of Hubbard model of ferromagnetism	109
7.2	Interaction between defects and transition metal impurities	110
7.3	Conclusion	113
8	Effect of Acceptor Doping in Magnetite Below Verwey Transition	114
8.1	Acceptor doped magnetite	117
8.1.1	Lithium ferrite: $\text{Li}_{0.5}\text{Fe}_{2.5}\text{O}_4$ and $\text{Li}_{0.625}\text{Fe}_{2.375}\text{O}_4$	118
8.1.2	Nitrogen substituted magnetite $\text{Fe}_3\text{O}_{3.5}\text{N}_{0.5}$	121
8.2	Conclusion	123
9	Conclusions	124
9.1	Future Work	126
A	Details of Calculations	128
B	Basis Sets	130
References		156

List of Figures

2.1	Electron paramagnetic resonance (EPR) spectra of a powder ZnO sample. A. Before annealing, B. After annealing in vacuum, C. Annealed and exposed to air.	20
2.2	Schematic diagram of a bound polaron model. A net ferromagnetic moment is retained as long as the polaron wavefunction percolates. As the temperature rises, polaron radius decreases (Eqn. 2.10) and percolation ceases above the Curie temperature.	31
4.1	Schematic diagram explaining working formulae for transition level calculation. Top: hole-charged defect. The transition level $\epsilon(+/0)$ has been explained as the example. Bottom: estimation of transition level $\epsilon(-/0)$	53
4.2	Band gap of ZnO estimated using Eqn. 4.14. $L = V^{1/3}$. Calculations are made using LDA exchange implemented on the Quantum Espresso code. The value of band gap E_g extrapolates linearly to 0.11 eV for infinitely large supercell. This value of E_g is too low in comparison to experiment but is comparable to other LDA results (see text) that always underestimates the band gap.	58
5.1	Wurtzite unit cell of ZnO.	63
5.2	Band structures of bulk ZnO (left) and that of ZnO with a neutral oxygen vacancy (V_O) (right) in a wurtzite $3 \times 3 \times 3$ supercell. The wurtzite Brillouin zone and the k-path is shown at the bottom. Horizontal dotted lines show the Fermi level.	65

5.3	The bandstructures (top) and crystal structures (bottom) of V_O in different charge states for fully relaxed $3 \times 3 \times 3$ supercell. From left to right, V_O^0 , V_O^+ and V_O^{2+} respectively. For spin polarized systems, red lines show the majority spin and green/dashed lines show the minority spin states. Large pink spheres denote the Zn atoms and smaller red spheres denote oxygen atoms (Shown on bottom-left of figure). The small green dot denotes the vacancy site. Fermi levels are shown by horizontal blue dotted lines.	66
5.4	(Left) Band structure of V_{Zn}^- for both spins (red: majority, green:minority). (Right) The Γ -point wave function isosurface of V_{Zn}^- state immediately below the Fermi level (blue dotted line)	68
5.5	The bandstructures (top) and crystal structures (bottom) of V_{Zn} . From left to right, V_{Zn}^0 , V_{Zn}^- and V_{Zn}^{2-} respectively, fully relaxed $3 \times 3 \times 3$ supercell. For the spin polarized systems majority and minority band diagrams are plotted in the same figure. Note that the ground state of V_{Zn}^0 is a spin-triplet with two holes. The color scheme is the same as Fig. 5.3.	69
5.6	The two different possible configurations of V_{ZnO} , A: Radial and B: Axial.	70
5.7	The bandstructures (top) and crystal structures (bottom) of V_{ZnO} for a fully relaxed $3 \times 3 \times 3$ supercell. From left to right, V_{ZnO}^0 , V_{ZnO}^- and V_{ZnO}^{2-} respectively. For spin polarized systems, red lines show the majority spin and green/dashed lines show the minority spin states. The color scheme is the same as Fig. 5.3 and Fig. 5.5 . . .	71
5.8	The bandstructures (top) and crystal structures (bottom) of V_{ZnO} for a fully relaxed $3 \times 3 \times 3$ supercell. From left to right, V_{ZnO}^0 , V_{ZnO}^+ and V_{ZnO}^{2+} respectively. The color scheme is the same as Fig. 5.7. .	72
5.9	Change in crystal structure upon relaxation of lattice around V_{ZnO}^-	73

5.10 Wavefunctions for trapped electrons in V_{Zn}^- , V_{ZnO}^- , and V_{ZnO}^{2-} vacancies at the Γ point of the Brillouin zone. Trapped electron wavefunction in V_{Zn}^- (A) viewed along the c axis, (B) viewed perpendicular to the c axis. Trapped electron wavefunction in V_{ZnO}^- (C) viewed along the c axis. (D) perpendicular to the c axis. Same for V_{ZnO}^{2-} (E) along the c axis and (F) perpendicular to the c axis. Pink and yellow surfaces show +ve and -ve components of the iso-surface, respectively. The green surface is the inside of the pink surface. 74

5.11 Band structure of ZnO with a neutral (V_{ZnO_3}) defect (red/solid line) superposed with the triplet states of $V_{ZnO_3}^-$ (Green/dashed line) and $V_{ZnO_3}^{2-}$ (Blue/dotted line). The states for more highly charged states are shifted up but the shift is smaller than that for V_{ZnO}^{2-} . The Fermi levels for the three charge states are shown by horizontal dotted lines. Right: V_{ZnO_3} defects in a $4\sqrt{3}\times 2\sqrt{3}\times 2$ supercell. 76

5.12 The majority-spin bandstructures of V_O , V_{Zn} and V_{ZnO} , showing the change in dispersion and energy levels due to crystal lattice relaxation. The red solid lines are the relaxed levels and the dashed green lines are the levels with ideal geometry. Fermi levels for relaxed (red) and unrelaxed (green) structures are shown by blue and yellow dotted lines, respectively. 77

5.13 The minority-spin bandstructures of V_O , V_{Zn} and V_{ZnO} , showing the change in dispersion and energy levels due to crystal lattice relaxation. The red solid lines are the relaxed levels and the dashed green lines are the levels with ideal geometry. Fermi levels for relaxed (red) and unrelaxed (green) structures are shown by blue and yellow dotted lines, respectively. 78

5.14 Majority (left) and minority (right)-spin bandstructure of $Zn_{1-x}Co_xO$: $x=0.055$ with one V_{ZnO} defect (red) compared to $Zn_{1-x}Co_xO$ (green) without any defect. The Fermi level is shown by horizontal blue dotted line. 79

5.15	Majority (left) and minority (right) bandstructures of $V_{ZnO}^0 + Al_{Zn}$ (red/solid) comparing with V_{ZnO}^- (green/dashed) obtained using a fully relaxed $2\sqrt{3}\times 2\sqrt{3}\times 2$ supercell. The Fermi level does not change and is shown by blue dotted line. Note that a square k-path is used for this cuboid supercell.	80
6.1	Defect formation energies as a function of fermi level position for V_O , V_{Zn} and V_{ZnO} . These two diagrams show formation energies for a $3\times 3\times 3$ supercell when the crystal structure is unrelaxed (top) and fully relaxed(bottom).	86
6.2	V_{ZnO} pair vacancy formation energies as a function of fermi level position compared with V_O and V_{Zn} . V_{ZnO}^- has a formation energy about 2 eV lower than the separated $V_O + V_{Zn}^-$	89
6.3	Estimation of band gap using total energies. Extrapolation towards infinitely large supercell has been shown by thin black line.	91
6.4	Comparison of transition levels obtained from total energy and single particle eigenvalue methods.	98
6.5	The transition energies $\epsilon(-/0)$ and $\epsilon(2 - /-)$ and the value of Hubbard-U for the V_{ZnO} defect with unrelaxed crystal structure. Values for different supercell sizes are plotted with respect to inverse of supercell size L. Value of the band gap E_g for infinitely large supercell ($L\rightarrow \infty$) is shown.	99
7.1	Estimation of U from different spin-population configurations of one (left) and three electrons (right) in two V_{ZnO} defects. Up and down arrows denote α and β spin populations. Length of the arrows vaguely depict population strength.	105
7.2	Wave function isosurface of V_{ZnO} defect-trapped electron in a $4\sqrt{3}\times 2\sqrt{3}\times 2$ supercell with two V_{ZnO} defects (marked V1 and V2) and two electrons in a relaxed crystal structure showing that in the ground state the two electrons reside on one vacancy and the other one remains empty. This implies a negative - U, otherwise, we should get both the defects half-filled (Heisenberg antiferromagnet).	107

8.1	Crystal structure of magnetite in the $P2/c$ cell below the Verwey transition temperature. Different iron sites are labelled.	115
8.2	Density of states of Fe_3O_4 with HF exchange parameters 20% and 15%. Respective band gaps and Fermi levels are also shown.	117
8.3	Majority and minority band structure of Fe_3O_4 with HF exchange parameter of 0.15. Dashed green line marks the fermi level.	118
8.4	Spin densities of pure magnetite (top) and lithium ferrite (bottom). Gold, cyan and silver spheres denote Fe, O and Li atoms, respectively. Note that the iron d -orbital-orientation has changed in $\text{Li}_{0.5}\text{Fe}_{2.5}\text{O}_4$	120
8.5	Majority and minority band structure of $\text{Li}_{0.625}\text{Fe}_{2.375}\text{O}_4$ (red) superposed on conventional lithium ferrite ($\text{Li}_{0.5}\text{Fe}_{2.5}\text{O}_4$) (green). $E(A)$ and $E(B)$ denote the Fermi levels for $\text{Li}_{0.625}\text{Fe}_{2.375}\text{O}_4$ and $\text{Li}_{0.5}\text{Fe}_{2.5}\text{O}_4$, respectively	121
8.6	Spin density of $\text{Li}_{0.625}\text{Fe}_{2.375}\text{O}_4$ viewed along the b -axis. The polaronic holes localised in an oxygen $2p$ -like orbital is shown as P1. The colour scheme is same as Fig. 8.4.	122
8.7	Majority(left) and Minority band structures of $\text{Fe}_3\text{O}_{3.5}\text{N}_{0.5}$ (solid/red) superposed on those of pure magnetite (green/dashed). Fermi levels are shown by $E_F(N)$ and $E_F(M)$ for $\text{Fe}_3\text{O}_{3.5}\text{N}_{0.5}$ and Fe_3O_4 , respectively.	123

Chapter 1

Introduction

In the material design for cutting edge electronic industry, oxide semiconductors attract a large share of the attention of scientists and engineers. These materials show a number of interesting properties such as large optical band gap with transparency, high photo-electric yield, metal-insulator transition and sometimes room-temperature ferromagnetism. Applications of these materials are quite diverse, including fabrication of microelectronic devices, energy from solar power, catalysis in chemical experiments and solid state sensors. Point defects such as vacancies and interstitials mediate dopant diffusion in semiconductors [1, 2] which is extremely important for the fabrication of various devices. The presence of a very small number of defects can affect the resistive [3] and photo-electric properties greatly [4, 5] and therefore is of great importance in fabricating photo-active devices such as light emitting diodes (LED) [6, 7, 8], waveguides [9] and sensors [10]. For example, zinc oxide (ZnO) is an optically efficient ultra-violet band gap semiconductor, but shows a green, yellow and blue photoluminescence when defects are present [5, 11].

Systematic experimental observations suggest that defects in semiconductors may have also a role in inducing or manipulating the magnetic properties [12, 13, 14, 15]. Following Dietl *et al* [12, 16], experimental studies carried out in the last decade show that oxides such as ZnO, tin oxide (SnO_2) or indium oxide (In_2O_3) can exhibit ferromagnetism (FM) if dilute amounts of transition metals (Mn, Fe, Ni, Co) [14, 15, 17] are present. A magnetic semiconductor is useful in spin-electronics or *spintronics*. Spintronics presents the possibility that the

spin-polarization of electrons can be used in electronic devices as an information carrier, hence leading to more compact and energy efficient devices. Wide band gap oxide semiconductors with a direct band gap, such as ZnO or copper aluminate (CuAlO_2), always have been in the centre of attention for this purpose. These materials are transparent and already are widely used as high-yield optical devices in the UV-visible range. Naturally there are great prospects for both optically and magnetically responsive semiconductor devices.

Some recent experiments show that the magnetism of the oxide semiconductors may not originate from dilute transition-metal (TM) doping but from their defects. ZnO and SnO_2 thin films were found to be FM, even without transition metal doping but in presence of high off-stoichiometry [18, 19]. On the other hand, FM was not found in TM (Co) doped ZnO thin films which were prepared with high crystallinity [20].

Since defects are so important for controlling these properties, experimental techniques have been developed to control the concentration of particular defects during growth of a sample. Manipulating the partial oxygen pressure of the growth chamber is the most common technique to control the concentration of oxygen vacancies or interstitials in a thin film sample produced by a method such as pulsed laser deposition (PLD) or molecular beam epitaxy (MBE). The cation vacancy / interstitial concentration can also be controlled by the metal vapour intensity of the molecular beam in an MBE method or by manipulating the initial stoichiometry in a chemical deposition method. However, it is nearly impossible to confirm the presence of a certain type of defect from experiments only and to identify a defect to be responsible for inducing one or more particular phenomenon such as photoluminescence signals or magnetism [21] which are not characteristic of the host material. It is important to have a detailed microscopic knowledge of the crystal and electronic structure of a defect in order to predict its role in certain phenomena. This can only be done using first principles simulations. Starting with some known experimental parameters such as the crystal structure parameters, first principles calculations can provide a detailed information on the atomic and electronic structure and electron dynamics of a system, based on quantum physics.

Density functional theory (DFT) developed by Kohn and Sham [22] can successfully describe the electronic structure of a system. DFT was used by Sato [13] to make the previously mentioned prediction of ferromagnetism in dilute TM doped semiconductors [12]. There are a number of questions regarding the accuracy of the simulation, but as the computational power and efficiency are growing exponentially, there is always opportunity for experimentation and development of techniques. At the present state of technology, a number of experiments ranging from atomic force microscopy (AFM) [23] to X-ray magnetic circular dichroism (XMCD) [24] can be virtually recreated by simulation. Almost any system, from bulk silicon [22] to composite nanostructures [25], can be simulated with a considerable level of accuracy using first principles methods. A primary concern of using a first principles method is that there is no single technique or algorithm that can be applied to all types of materials. So the scientific community has developed a number of different computer codes and algorithms for particular materials/systems.

The most exploited and effective method to date for simulation of electronic structure of materials is the DFT, mentioned previously. The original DFT proposed and implemented by Kohn and Sham has a very simple but effective assumption, namely the local density approximation (LDA) [22]. Details of this assumption and application of LDA are discussed in Chapter 4, but the idea is described briefly here. Solution of DFT is obtained by invoking an iterative algorithm to calculate the electronic structure and energies of a many-particle system. This is done by assuming the potentials acting on the electrons in a system are functionals of charge density, which is a function of position vector \mathbf{r} . The key potentials in the Schrödinger equation are the electron-nucleus electrostatic potential and the electron-electron coulomb and exchange potentials. The exact form of the exchange-correlation potential is unknown and derived using the LDA by assuming that it is a functional of the electron density and varies in the same way as in a homogenous electronic system. For narrow band gap or metallic systems, the electron-density does not change rapidly in real space and the approximation made in LDA is valid and reproduces the energy eigenvalues of these systems correctly. Therefore the corresponding density of states is in good agreement with experiment [22, 26]. As researchers pushed on the boundaries of

simulation of electronic systems, it was found that this simple approximation does not work for many electronic systems. For example in systems with interacting 3d orbital-electrons at the top of the valence band, electron dynamics is strongly correlated and charge density varies rapidly in space. LDA severely underestimates the correlation effect and therefore underestimates the band gap in those systems [27, 28, 29]. Several remedies for this problem have been provided by introducing new techniques such as LDA+U [29] (U is a Coulomb energy correction), generalized gradient approximation (GGA) [30], GGA+U [31] or the GW approximation (GWA) [32] etc. But the discovery of new phenomena and new experimental techniques in different novel materials presents a constant challenge to modeling and simulation of electronic structures.

HSE [33] and B3LYP [34, 35] density functionals provide hybrid exchange-correlation functionals based on the original DFT algorithm which are more accurate than LDA for strongly-correlated systems and wide band-gap semiconductors. B3LYP is a hybrid of DFT and Hartree-Fock (HF) methods and is an accurate tool for predicting the band gap and exchange coupling energies of magnetic semiconductor oxides [36, 37, 38]. Details of the B3LYP method and its implications are described in Chapter 4. In the present context, the role of intrinsic defects in the electromagnetic and absorption/emission properties of oxide semiconductors have to be identified using first-principles methods. This task presents a twofold problem to be solved. Firstly, a computational method that can describe the semiconductor oxides properly, *i.e.* estimate the band-gap, magnetic exchange energies and the defect formation energies with reasonable accuracy which is determined by results in agreement with experiments. Computation of electronic structures becomes more challenging when defects are involved. Defects reduce the symmetry, making computation expensive regarding computer-time and also make the convergence of the calculations difficult. Some defects tend to toggle the system between metallic and non-metallic depending on Fermi level [39]. Therefore the choice of computational technique and functional to study defect systems is crucial. However, we have already noted that B3LYP hybrid DFT is reliable in this respect. In the current work, B3LYP hybrid DFT has been used for almost all calculations and the results are in good agreement with comparable experiment results [39].

The second part of the problem is to interpret these results such that one or more defect structures can be identified as being responsible for a particular defect related phenomenon. The primary focus of this thesis is on the effect of particular defects and impurities on the electronic structure of oxides and interpreting some of the experimental observations made on defect related oxides. Predictions are made for microscopic electronic structures of possible defects that may appear in an oxide.

Electronic structures of zinc oxide (ZnO) and magnetite (Fe_3O_4) have been computed in this work with relevant defects and impurities. The formation energies of the defects in ZnO were calculated from the total energy calculations for supercells with various intrinsic vacancy defects in order to find out the naturally occurring defects, from a thermodynamic point of view. Electron transition levels were calculated between the same defect levels with different occupancy. An estimate of the optical transition energy can be made from these calculations and thus the defects responsible for any photoluminescence signals those are not characteristic to the host material, can be identified. This phenomena is explained in detail in the next section.

A different phenomenon is addressed in Chapter 9. The effects of acceptor impurities on the band-gap, magnetic moment and the electronic structure of magnetite (Fe_3O_4) have been investigated using B3LYP hybrid DFT.

More detail on the problems tackled in this work and the methodologies used in solving them are outlined in the following sections.

1.0.1 Intrinsic defects in ZnO

ZnO shows anomalous photoluminescence [5, 11] and paramagnetism [15, 40, 41] when defects are present in the sample. There are reports of yellow, green and blue photoluminescence in ZnO thin film samples [11, 40]. Another interesting phenomenon observed in off-stoichiometrically grown ZnO thin-films is room temperature ferromagnetism (RTFM). RTFM was observed when a dilute amount of transition metal is doped [15, 17, 42, 43] and even in undoped ZnO [18, 19] with intrinsic defects from off-stoichiometry. Since no local ferromagnetic order associated with the transition metal ions was observed and the samples render

non-magnetic when grown with perfect stoichiometry [20, 44], this phenomenon is also often attributed to intrinsic defects [15, 36, 43, 45]. Similar experimental observations were made on other metal oxide thin films such as HfO₂ [46, 47], TiO₂ [47, 48], In₂O₃ [47] and SnO₂ [49].

As discussed previously, the microscopic structure of the defect responsible for a particular experimental observation must be known in order to prepare a recipe for successful reproduction. At the present state of technology, determination of the exact microscopic and electronic structure of a defect is not possible from the experiments mentioned above. However, some experiment can give us more information on the nature of the defects. Electron paramagnetic resonance (EPR) and positron annihilation spectroscopy (PAS) experiments show that some defects act as electron traps. An electron trapping defect with a single electron trapped can retain a finite spin moment and act as a paramagnetic centre. Evidence of single-electron-trapping defects in ZnO was found in a recent EPR experiment. EPR on ZnO powder yielded a resonance with a g -factor close to that of a free electron [50]. The resonance intensity increases on vacuum annealing of the sample and greatly reduces in air exposure [50]. This phenomenon is commonly attributed to electrons trapped in vacancies formed on surfaces. This is also observed in HfO₂ and ZrO₂ [51, 52]. PAS experiments also have given evidence of electron traps in ZnO [53]. These electron traps are also known as F-centres, from the German word *Farbezentrum* or colour-centre. This name was chosen because in many transparent semiconducting oxides, electron trapping defects add energy levels in the spectrum that take part in optical recombination [54, 55]. Notably, these oxides are n-type in normal growth conditions [56]. The frequently occurring oxygen vacancy is thought to be a source of electrons [42, 43, 44, 57] but extensive doping is also done by doping aluminum (Al) [44] or nitrogen [58], in order to produce a measurable n-type or p-type conductivity. When heavy electron/hole doping is involved, there is a possibility of magnetism from exchange of itinerant electrons without defect involvement [59, 60]. But some experimental results suggest that the contribution of defects to the magnetism of these oxides may be greater than the exchange of itinerant electrons. Kaspar *et al* [20] showed that if defects are not present, *i.e.* for pure and stoichiometric Co-doped n-type ZnO, magnetism cannot be observed and therefore must be associated with defects.

In this work, the intrinsic vacancy defects oxygen vacancy (V_O), zinc vacancy (V_{Zn}) and ZnO Schottky pair vacancy (V_{ZnO}) were investigated. The electronic structure, formation energies at different charge states, values of transition levels and Hubbard- U values [61] were estimated. The significance of these quantities is explained in the next paragraph. These three intrinsic vacancy defects were chosen for the following reasons: point defects such as vacancies and interstitials have low formation energies and therefore are the most abundant defects in oxides [55]. The II-VI oxides such as ZnO grow oxygen deficient with large concentrations of oxygen vacancies if the oxygen partial pressure of the growth chamber is not maintained to at least 1mBar [17]. Cation interstitials and anti-sites are created in an oxygen-poor growth environment but these defects have higher formation energies [62, 63] and also do not act as electron-traps or paramagnetic centres. Interstitials and antisite defects are therefore not the primary focus of this work. Cation vacancies can be controlled in growth techniques such as the MBE. Aggregation of V_O and V_{Zn} will form a V_{ZnO} Schottky vacancy if the formation energy of a Schottky vacancy is lower than that of two separate V_{Zn} and V_O vacancies. Occurrence of a Schottky pair vacancy or more complex cluster vacancies resulting from further aggregation of vacancies in a highly off-stoichiometric condition was investigated in this work. Such defects will host a number of energy levels and may act as electron traps.

V_O and V_{Zn} are donor and acceptor-type defects respectively. V_O can occur in three charge states, i.e. 0, +1 and +2, while V_{Zn} can take up 0, -1 and -2 charge states [62, 64]. V_{ZnO} is a neutral vacancy with respect to dangling charges in the defect and can trap both holes and electrons, giving it a charge state range -2, -1, 0, +1, +2 [39]. All the charge states of these vacancies may not be stable with respect to dissociation into other charge states. For positive values of Hubbard- U [61] one vacancy is needed to be more stable at its +1 or -1 state than its +2 or -2 state. We already know from the literature that the V_O^+ state is unstable and that V_O is a negative- U defect [36, 64]. Different charge states of these defects were investigated with both ideal, unrelaxed and relaxed geometries. There is a large change in electronic structure observed upon relaxation. Formation energies and transition levels of these three vacancy defects were calculated for both relaxed and unrelaxed ideal geometries in order to confirm stability of the defect

in one or other charge state. Large alterations in the values of formation energy were noted upon relaxation, even though the relaxation energies are relatively small with respect to the change in transition levels and the relaxation is quite localized around the vacancy site. Transition levels between charge states were calculated from the difference in their formation energies. These estimations of formation energies and transition levels are made using total energies from hybrid DFT self-consistent-field calculations. However, another method is also used to calculate transition levels from energy eigenvalues of the charged defect states. The methods are discussed in detail in Chapter 3 and the results from the two methods are compared in Chapter 6, where we can see that they agree roughly with each other, as well as with other published work, when the crystal structure is relaxed. The deviations between the results obtained from the two different methods are small but significant, if comparison is made with photoluminescence experiments. The possible corrections that can be applied are also discussed.

Hubbard- U values for these defects were calculated from differences in transition levels [61, 64]. Large changes in U -values were found as the crystal structure was relaxed. This is because of the alteration of the crystal structure upon relaxation around the defect site as the defect occupancy is changed.

The Hubbard- U value for V_{ZnO} was also calculated from the energy difference between two different spin configurations of a 3/4 filled V_{ZnO} vacancy pair. A large supercell with two V_{ZnO} vacancies 11 Å apart was chosen for this purpose. In a 3/4 filled system electrons trapped in defect sites 11 Å apart were found to interact with each other. The U -value found from the two methods are in agreement with each other. This method gives us useful information about long range defect-defect interaction. However, this method requires large supercell calculations and is extremely expensive in computer time, especially when lattice relaxation is necessary with different spin configurations. Hence, these calculations were not repeated for the estimation of U for V_O and V_{Zn} .

A similar set of calculations were carried out for magnesium oxide (MgO) to estimate the value of Hubbard- U for the MgO pair vacancy (V_{MgO}), following Ricci *et al*'s [65] prediction that electron-trapping MgO pair vacancies may frequently occur in MgO thin film surfaces and act as paramagnetic centres. Also, there is a report of observation of room temperature FM in MgO thin films [66]

which may occur from defect-defect interaction. V_{MgO} was found in this work to have large U -value and moderate bandwidth.

A model for defect-defect interaction is proposed in this work. A defect may trap one or two electrons in an energy level lying in the band gap of the host system. This energy level can be represented by the solution of a single-band Hubbard model. Based on a single band Hubbard model, different 3D lattice structures (simple cubic, fcc and bcc) were studied in the past using different finite temperature computational algorithms, such as high temperature series expansion (HTSE) [67] and quantum Monte Carlo (QMC) [68]. Magnetic phase diagrams from these calculations suggest that electron-trapping defects with a large Hubbard- U and moderate bandwidth will retain a parallel-spin configuration between the defect-trapped electrons at finite temperature when the defect-level is partially filled, away from half filling.

The interaction between defect and transition metal (TM) ions substituted for Zn in ZnO is investigated here. This is done by substituting up to two Co^{2+} ions at various distances from the defects. The interaction between a Co^{2+} ion and defect-trapped electron is large when the Co^{2+} ion is at nearest neighbour's distance from the defect. The mechanism of the interaction depends on the wavefunction of the trapped electron in the defect.

The effect of crystal structure relaxation was also tested with TM doping. Due to the similarity between ionic sizes of Co and Zn, there is hardly any displacement around the substituted Co^{2+} ion. We will see in Chapter 7 that the deep 3d filled states in Co rise up in the energy spectrum upon relaxation that yields stronger coupling with the defect state.

As discussed previously, ZnO thin films also exhibit a number of photoluminescence anomalies in the presence of defects [5]. ZnO has an ultraviolet (UV) region direct band gap of 3.4 eV [56], but green, yellow and blue photoluminescence was observed in ZnO thin films with various degree of defects [6, 11]. Once again, there is a huge debate and speculation on the details of the structure of the defect responsible for the different luminescence colours [69, 70, 71]. The optical transition energies for the defect energy levels have to be calculated very precisely. Conventional LDA/LDA+U computational methods underestimate the defect transition levels and therefore new techniques such as hybrid DFT or GW

must be adopted [72]. In this work, a brief commentary has been made on the estimation of optical transition energies from the defect transition levels and the role of various defect transitions are discussed.

1.0.2 Acceptor doped magnetite

The electronic structure of acceptor type impurities doped in magnetite (Fe_3O_4) was studied using a similar DFT scheme. Fe_3O_4 shows a number of interesting phenomena such as ferrimagnetism, a metal-insulator transition, charge order and mixed valence hopping [73]. The metal-insulator transition, known as the Verwey transition [74], occurs around 123 K. Below the transition temperature the crystal structure distorts from cubic symmetry [74]. The structure in the insulating state was investigated [75] and evidence was found for charge ordering by X-ray diffraction [73] and muon spin spectroscopy [76]. The iron atoms in Fe_3O_4 are divided between tetrahedral (known as the A-sites) and octahedral (B-sites) sites. Since Fe exists in a Fe^{2+} and Fe^{3+} mixed valence state on octahedral sites, hopping of the charge carriers between Fe^{2+} and Fe^{3+} gives little electrical conductivity [75, 77] below the Verwey transition. Neutron diffraction experiments reveal that the electronic spin on Fe^{3+} ions in tetrahedral sites are aligned antiparallel to that on the octahedral Fe^{3+} ions and only the moments from Fe^{2+} ions give a net ferrimagnetic moment [73]. Hole-doping oxidises Fe^{2+} to Fe^{3+} which increases the magnetic moment and quenches mixed-valence hopping simultaneously. Substituting half of the Fe^{2+} ions on tetrahedral sites in magnetite by lithium yields lithium ferrite ($\text{Li}_{0.5}\text{Fe}_{2.5}\text{O}_4$). The substitution of Li preserves the lattice order and $\text{Li}_{0.5}\text{Fe}_{2.5}\text{O}_4$ has the same crystal structure as Fe_3O_4 [78]. Some experiments found $\text{Li}_{0.5}\text{Fe}_{2.5}\text{O}_4$ to be a moderate band gap semiconductor at room temperature and has a higher energy associated with spin polarized photoelectrons than that of pure magnetite [78]. With a high concentration of oxygen vacancies, Li-ferrite shows strong magnetization of about $2.5\mu_B$ per formula unit at room temperature [79].

Hole doping causes quenching or termination of this mixed-valence hopping in various degrees, depending on doping concentration. Li ferrite was studied in this work using the low temperature structure. Different site substitutions were

considered in order to find out the energetically most favourable substitution site. In $\text{Li}_{0.5}\text{Fe}_{2.5}\text{O}_4$ all Fe^{2+} ions are oxidised and the Fe^{2+} -d bands governing mixed-valence hopping, vanish and a moderate optical band gap of 2.55 eV opens up. A spin-split polaronic band can be introduced by overdoping of Li which can give rise to p-type conductivity in low temperature by small polaron hopping. The excitation probabilities and magnetic moments are manipulated by substituting oxygen with nitrogen ($\text{Fe}_3\text{O}_{3.5}\text{N}_{0.5}$) which also removes mixed valence hopping bands depending on substitution site. The geometry remains quite unaltered comparing to Li-ferrite as N atoms substitute O atoms.

Chapter 2

Defects in oxide semiconductors: A brief literature review

The role of defects in modifying the photo-electric and magnetic properties of oxides were briefly described in the introductory chapter. Here we will go into more detail to discuss the state of research in this field and the relevance of defect study in oxide semiconductors. Although many types of defects, such as surface defects and stacking faults, may impact properties of oxides but point defects play a particularly important role, even when very dilute as they modify several important physical properties. A detailed understanding of the defect structure responsible for a particular experimental observation has been obtained in very few cases [55]. The main objective of this chapter is to illustrate the progress that has been made in understanding the electronic and structural properties of oxide defects and to show how this knowledge can be applied to engineer materials properties. The development of higher-precision instrumentation for materials characterization, improved processing methods with the ability to control chemistry and structure on a near-atomic scale, and improved computational tools capable of considerably more realistic modeling are the key foci of the research in this field. Since we are interested in point defects in particular, emphasis has been given to experimental and computational results obtained for point defects in oxides.

A brief discussion is made on the thermodynamics of creation and stabilisation of defects, describing their dependence on temperature, atmosphere, and

composition. We then examine how these defects can impact properties (e.g., electrical, optical or magnetic) and how these properties can be experimentally analyzed and evaluated. We discuss spectroscopic experimental results, dealing with defect systems and then the computational interpretation and predictions.

The key types of intrinsic point defects in oxides are vacancies, interstitials and antisites. A vacancy is removal of an atom. In an oxide, MO, vacancies can be of both cationic (V_M) and anionic (V_O). Ions may occupy interstitial crystallographic sites and give interstitial defects (M_i , O_i) or occupy lattice sites of an ion of different species, leading to antisites (M_O : ion M occupying O lattice site or vice versa, O_M). Extrinsic defects include donor or acceptor impurities (D_M , A_O) and less common impurity interstitials (D_i). The notation used here to describe defects is known as the Kröger-Vink notation [80]. The original Kröger-Vink notation describes the charge state of a defect by putting \times , \bullet , and $/$ in the superscript to describe neutral, positive and negative charges, respectively (e.g. V_O^\times , V_O^\bullet and V_O' represent neutral, singly positively and negatively charged oxygen vacancies respectively). In this work, we use 0, + and - , respectively, for simplification.

At high growth temperatures, point defects are mobile and they may collide to create pairs or cluster defects. A pair defect may be more stable than separate defects from a thermodynamic point of view [55, 81]. Pair defects include the Schottky pair vacancy ($V_M - V_O$), Frenkel ($V_M - M_i$) and anti-Frenkel ($O_i - V_O$) defects. The probability of formation of a defect can directly be estimated from a reciprocal function of formation energy which is the energy cost to create a defect. A detailed explanation of the significance and methods for estimation of formation energies is given later in this chapter and in Chapter 4. In general the possibility of occurring of a particular type of defect may be anticipated from the host crystal structure and the growth condition of an oxide. For example, a Schottky defect has more probability of occurring than a Frenkel defect in a close-packed structure because the energy required to pack one interstitial ion into the lattice is high unless the gas pressure of that particular ion during growth is very high.

Basic chemical thermodynamic principles determine which types or species of defect dominate. At equilibrium, at a given temperature and pressure, the free

energy should follow,

$$\Delta G = \Delta H - T\Delta S < 0 \quad (2.1)$$

where, H and S are the enthalpy and entropy, respectively, and T is the absolute temperature. ΔS can be represented from the probability relation $\Delta S = k\ln W$ where W is the thermodynamic probability and depends on the description of entropy. The entropy change may be divided into two parts $\Delta S = \Delta S_V + \Delta S_C$ where, ΔS_V is the change in vibrational entropy and ΔS_C denotes the configurational entropy change induced by the formation of the defect. The two quantities can be estimated from the probability equation. The vibrational entropy change,

$$\Delta S_V = xk_B \ln \frac{\nu}{\nu'} \quad (2.2)$$

where, x is number of neighbours of the defect and ν and ν' are the vibrational frequencies corresponding to bulk lattice and the lattice with the defect, respectively. The configurational entropy change is given by,

$$\Delta S_C = k_B \ln P \quad (2.3)$$

where, P represents the number of ways n defects may be distributed in a lattice of N atoms (therefore over $N+n$ sites).

Hence, solving for n , by minimising ΔG in Eqn. 2.1, we have,

$$n \approx N e^{\Delta S_V - \Delta H/k_B T} \quad (2.4)$$

Thermodynamics gives us information about which defect will dominate at equilibrium but in practice the concentration of a particular type of defect is increased deliberately by controlling growth atmosphere and target stoichiometry in growth techniques such as pulsed laser deposition (PLD). In PLD or other modern-day growth methods such as molecular beam epitaxy (MBE), oxygen partial pressure P_{O_2} is a key parameter in controlling stoichiometry. Since it is important to have a predictive knowledge of the concentration of defects at any given temperature, a simple model can be established, based on thermodynamics and defect chemistry, such that the concentration of any defect can be represented as a function of P_{O_2} and temperature T. Duncan [82] and Huggins [83] have shown that an isothermal

plot of defect concentration with respect to P_{O_2} can be very useful in growth design. Tuller and Bishop [84] have shown that from such a diagram, drawn using experiments on Gd doped CeO_2 , the concentration of oxygen vacancies can be expressed as $[V_O^{2+}] \propto P_{O_2}^{-1/6}$ [84]. This relationship becomes $[V_O^{2+}] \propto P_{O_2}^{-1/4}$ for higher oxygen partial pressure, where the cation vacancies dominate. This is important from the application point of view. Given that all other stoichiometric parameters are fixed, measurable quantities which arise from the conduction of vacancy electrons such as electrical conductivity, can be written as a function of P_{O_2} and temperature T .

2.1 Characterisation of vacancy defects

In the previous chapter it was noted that the structural and electronic properties of defects can not be easily obtained from experiment, and require theoretical models and first principles simulations. High-resolution transmission electron microscopy (HRTEM) has nearly reached the atomic scale in the last decade [85]. However, point defects still need to be identified and characterised using indirect methods. Defects in oxides are mostly investigated using a range of spectroscopy experiments. Absorption and emission spectroscopies of different types [5] can be used to measure the densities of states of defect energy levels. These quantities are directly comparable to first-principles simulation results. Magnesium and zinc oxide are two of the most investigated oxides on which these techniques have been used [11, 86, 87, 88, 89]. Results were interpreted using first-principles methods and a number of density functionals and algorithms [21, 39, 63, 64, 65, 90]. In this chapter we discuss some of these experimental results and corresponding theoretical models that help to understand the role of defects in modifying properties of semiconductors.

New electronic states introduced by defects can be identified by techniques such as photoluminescence (PL) spectroscopy [11], sometimes generated by high energy electron irradiation [86]. Characterisation of defect charging and electron-trapping behaviour can be understood using electron paramagnetic resonance (EPR) [41, 55] and positron annihilation spectroscopy (PAS) [89, 91]. These techniques help to identify defects which act as paramagnetic centres.

Intrinsic defects are thought to take part in high T_C (Curie-temperature) ferromagnetism (FM) observed in non-magnetic oxides such as ZnO [18, 19], SnO₂ [19] and In₂O₃ [17, 18, 92] and dilute magnetic semiconductors (DMS) Zn_{1-x}Co_xO, Sn_{1-x}Fe_xO₂ ($x = 4-7\%$) [15, 93]. FM is detected using magnetic hysteresis [17] and X-ray magnetic circular dichroism (XMCD) [44] with off-stoichiometric oxide samples. Several theoretical models are proposed to explain the role of defects in this phenomenon and require highly accurate first-principles calculations of several measurable parameters such as magnetic moment and exchange constant, in order to test these models.

The formation energy of a defect and the transition level between different charge states are the parameters computable from first-principles simulations. They can be used to interpret the experimental results. The formation energy of a defect is the energy cost to create that defect in a system in a particular charge state and can not be measured directly. It represents the probability of formation of a particular type of a defect. One recent report by Kim and Kang [94] reports techniques to estimate the formation energy of the oxygen vacancy in ZnO from photoluminescence (PL) experiments.

The transition level (TL) between the two charge states of a defect is another parameter which is computable from first principles. The optical recombination energy can be calculated from transition levels and can be directly compared with the results from PL experiments.

In the rest of this chapter we will discuss in more detail, first the experimental results for EPR, PAS and PL, dealing with defect systems and then the first principles calculations and predictions. In this work we have investigated defects in ZnO, so this literature review is mainly focussed on ZnO defects. ZnO is one of the most studied wide-gap oxides both in theory and experiment. Models for defect-driven high- T_C ferromagnetism in intrinsic oxide semiconductors and DMS are also discussed.

2.1.1 EPR and PAS studies of electron traps

Some defects trap electrons in localized states. Vacancy defects often act as electron traps [55] and dominate absorption/emission spectra of the material

2.1 Characterisation of vacancy defects

in the band gap energy range. This may cause coloration of the material and therefore electron trapping vacancy defects are sometime known as colour centres or more commonly F-centres after the German term *farbezentrum* (colour centre).

In an EPR experiment the paramagnetism of an unpaired charge can be observed when the sample, either single crystal or powder, is put in a magnetic field which splits the otherwise degenerate spin states. The unpaired spin can move between energy levels by either absorbing or emitting electromagnetic radiation of energy $\epsilon = h\nu$, such that the photon energy is equal to $g\mu_B B_0$. g is the Landé g -factor and B_0 is the magnitude of the external magnetic field. This leads to the fundamental equation of EPR spectroscopy [95],

$$h\nu = g\mu_B B_0 \quad (2.5)$$

Typically, EPR measurements are made in the GHz frequency range (9 - 10 GHz), with fields B_0 corresponding to around 4 Tesla. EPR spectra can be obtained by varying the magnetic field B_0 for a fixed frequency ν . The Landé g -factor is a 3×3 tensor. For an axially symmetric defect wavefunction such as V_O in ZnO, the unique elements of the tensor are g_{\parallel} and g_{\perp} . This gives further information about the environment of the unpaired charge. For example, if a paramagnetic centre is occupied by a lone electron in an s-like hydrogenic wavefunction with nearly spherical symmetry, the g -tensor is expected to be isotropic with g -value close to the free electron value, 2.0023.

EPR g -factors for defects in ZnO and other oxides are given in Table 2.1.

The first column of Table 2.1 shows the possible paramagnetic centres assigned in the respective publication. These assignments are made on the basis of the growth stoichiometry of the samples and may not describe exact structural information of the defect. The V_O^+ is a spin-1/2 state and is found unstable with respect to dissociation into V_O^0 and V_O^{2+} [36, 39, 64]. Therefore it is unlikely to be found in n-type ZnO. The signal thought to be corresponding to V_O^+ in ZnO is only observed at low temperature and after illumination in optically detected EPR (ODEPR) experiments [41, 96, 97, 98]. The V_O^+ EPR signal disappears after

2.1 Characterisation of vacancy defects

Table 2.1: EPR g-factors for ZnO, ZrO₂, HfO₂, MgO and CaO

Defect	spin	g_{\parallel}	g_{\perp}	g
ZnO				
V _O ⁺ ¹	1/2	1.9945	1.9960	
V _{Zn} ⁻ ¹	1/2	2.0024	2.0124	
Zn _i ⁺ ¹	1/2	1.9605	1.9595	
Powder F-centre ²	1/2			2.0027
HfO ₂ powder				
H4 centre ³	1/2			2.0025
ZrO ₂ powder				
Z4 centre ³	1/2			2.0028
MgO				
F ⁺ centre ⁴	1/2			2.0023
F ₂ centre ⁴	1/2			2.0008
F ₂ centre ⁵	1/2	2.0004	2.0012	
CaO				
F ⁺ centre ⁴	1/2			2.0001
F ₂ centre ⁵	1/2	1.9995	1.9980	1.9980

sample annealing to over 400°C [41].

The V_{Zn} vacancy in ZnO is an acceptor defect with a deep defect level [62]. The neutral V_{Zn} vacancy was reported to have a spin 1 triplet ground state by Galland and Hervé [101]. As neutral V_{Zn} charged by one electron to V_{Zn}⁻, it undergoes a Jahn-Teller distortion. The single hole in V_{Zn}⁻ may be localised on an oxygen ion with $g_{\parallel} = 2.0024$ and $g_{\perp} = 2.0193$ [96, 101]. The g-tensor symmetry suggests that V_{Zn}⁻ wavefunction is axially symmetric. We will see in Chapter 5 that it is the oxygen-2p orbitals neighbouring a V_{Zn} that host the electron.

The zinc interstitial in ZnO, Zn_i, is a spin 1/2 defect in the Zn_i⁺ state. EPR

¹Ref. [96]

²Ref. [50]

³Ref. [88]

⁴Ref. [99]

⁵Ref. [100]

2.1 Characterisation of vacancy defects

signals with $g_{\parallel} = 1.9605$ and $g_{\perp} = 1.9595$ are assigned to Zn_i^+ by Vlasenko and Watkins [96]. An EPR signal with both components of g close to 1.96 is commonly observed in ZnO and, according to a number of publications, is associated with a shallow donor defect. This defect is labeled as effective mass (EM) defect [90, 96, 102]. Zn_i interstitial is one possible candidate for this shallow donor defect [102].

EPR g -factors for oxides other than ZnO also show paramagnetic electron traps. EPR resonances observed in HfO_2 , ZrO_2 and ZnO powders occur almost at the free electron g -factor, 2.0023. The resonance peaks are sharp with line-widths as narrow as 2G at 9.8 GHz when HfO_2 and ZrO_2 powders are annealed in vacuum to temperatures between 300° and 750°C for two hours [88].

Fig. 2.1 depicts the result of an EPR experiment done on ZnO powder [50]. The resonance peak shown has a g -factor of 2.0027 ± 0.0002 , which is close to that of a free-electron and it has a symmetric line shape. Resonance intensity increases upon vacuum annealing and reduces fast on air exposure. The rapid decrease in the resonance peak upon air exposure suggests that the unpaired electron is trapped in such a defect that reduces in ambient atmosphere. This is thought to be oxygen vacancy defect that absorbs oxygen from the air, and so probably is on the surface of the sample. A sharp and symmetric resonance peak was obtained for a powdered sample, where the crystalline grains are randomly distributed. This may indicate that the unpaired electron associated with the resonance signal has a spherically symmetric s -like orbital. A similar annealing effect on EPR spectra was observed for HfO_2 and ZrO_2 [52, 88].

Defects in alkaline earth metal oxides are also extensively studied using EPR. g -factors for oxygen deficient MgO and CaO has been found to be 2.0023 and 2.0001, respectively [99]. EPR signals associated with these g -factors were assigned to the $V_O^+ F^+$ centre which, unlike in ZnO, is thought to be a stable state [99]. EPR signals from MgO powders heated above 400°C show a reduction in the F^+ line at $g = 2.0023$ and appearance of a new line at $g = 2.0008$, which was assigned to an F_2^- -centre [99]. Similar phenomena were observed for CaO, which, upon annealing, also shows an F_2^- -centre peak with a g -factor of 1.9995 [100]. The F_2^- -centre may be assigned to an anion-cation divacancy [65, 99]. At high annealing temperature the defects are mobile and may congregate to form a

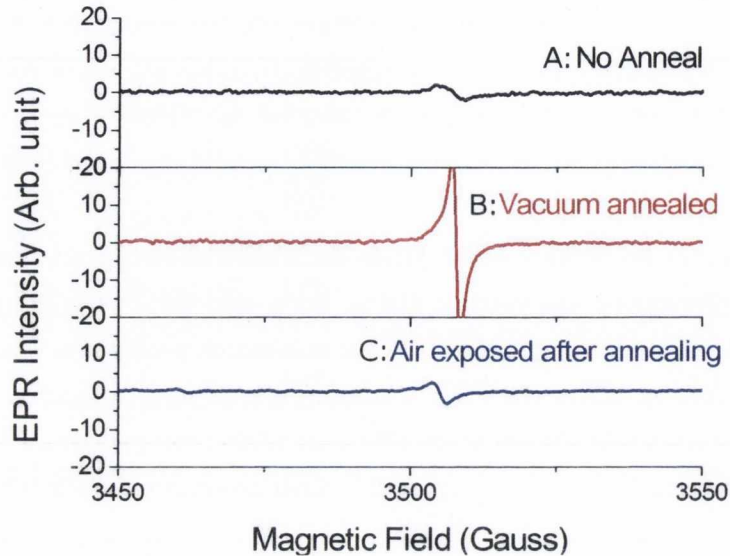


Figure 2.1: Electron paramagnetic resonance (EPR) spectra of a powder ZnO sample. A. Before annealing, B. After annealing in vacuum, C. Annealed and exposed to air.

divacancy. We show in Chapter 6 that the formation energy of a ZnO divacancy V_{ZnO} is 2 eV lower than separate V_{Zn} and V_O vacancies. Ricci *et al* [65] have argued that electron-trapping MgO divacancy defects would congregate on the surface of the sample due to a further lowering of formation energy.

Positron annihilation spectroscopy (PAS) is another tool used to characterise F^- -centres. The principle of this technique is that if positrons are injected into a solid body, they will annihilate upon meeting electrons and emit γ -ray photons. The interaction can be written as,



The two γ -photons which are emitted, are detected. An artificial radioactive light element such as ^{22}Na is commonly used as the positron source. The intensities of incident and emitted positrons are detected to calculate the annihilation rate λ and positron lifetime τ ($\lambda = \tau^{-1}$). The lifetime of the incident positron will depend on the electron density in its path. By comparing the fraction of positrons

2.1 Characterisation of vacancy defects

that have a longer lifetime to those that annihilate quickly, insight can be gained into the voids or the defects of the structure. Typically if there is a void (vacancy defect) in an oxide semiconductor sample, the positron lifetime increases by $\tau_V \approx 1.2\tau_b$ where τ_b is the positron lifetime in the bulk material [103]. The average value of τ_b for semiconductors is 200 - 300 picoseconds. An important advantage of PAS of semiconductors is its sensitivity to the charge states of positron traps (charged vacancy defects). Remarkably different temperature dependencies of trapping rates may be observed if the defect is charged positively, negatively or is neutral.

PAS is quite extensively used in characterising defects in ZnO. Tuomisto *et al* [89] reported from PAS studies on as-grown and electron-irradiated ZnO that the V_{Zn} vacancy is a dominant acceptor defect and can account for almost all of the acceptor centres in n-type ZnO. It is commonly believed that the n-type nature of as-grown ZnO and a number of oxides arises from high oxygen vacancy concentrations, if not grown under an oxygen partial pressure [17] (of at least 1 mBar for ZnO). Tuomisto *et al* argued that in a Zn-poor growth condition, n-type conductivity arises from residual hydrogen impurities. In more recent PAS studies on ZnO, V_{Zn} was expected to be mostly in a double-negative-charge state [89, 104]. The V_O defect was expected to be a deep donor when induced by electron irradiation, having an ionisation level about 100 meV below the conduction band edge [104]. Shining monochromatic light on the samples during the positron annihilation measurements at low temperature leads to the conclusion that both irradiation induced V_{Zn} and negative-ion-type defects have ionisation levels close to 2.3 eV below the conduction band [104]. The negative-ion-type defects were suggested to be oxygen interstitials (O_i) or oxygen antisites (O_{Zn}) [104].

Another recent PAS study along with an optical transmission study by Selim *et al* [62] supports the earlier evidence of V_O being a deep donor and V_{Zn} a dominant acceptor defect. Optical transmission experiments suggest that the red or orange coloration in ZnO annealed at 1100°C originates from transitions between V_O defect states. In the same study, formation of Zn_i was found unlikely to occur, even in Zn-rich growth conditions. Creation of V_{Zn} was observed after irradiating with 2 MeV O^+ ions [105]. Formation of vacancy clusters is observed at higher irradiation fluences. ZnO divacancies and vacancy clusters are expected

to be formed by aggregation of irradiation induced single vacancies [91, 105]. These complex defect clusters are charge-neutral, suggesting that they are V_{ZnO} divacancies, which is an intrinsic charge neutral defect.

2.1.1.1 Negative U defects

When a defect traps more than one electron, the electrons exert Coulomb repulsive forces on each other. This introduces a finite energy cost to add one additional electron to an already half-filled defect state. This energy cost is the on-site Coulomb repulsion energy or Hubbard- U . For a bivalent metal oxide such as ZnO or MgO, a cation defect or a Schottky pair defect can trap up to two electrons. The energy cost of adding a second electron to such a defect already occupied by one electron is U . A combination of lattice and electronic relaxation in some defects allows a second electron to be added to the defect, accompanied by a lowering of the energy. The Hubbard- U values are negative for these defects and they are known as negative- U defects [64]. We have mentioned previously that the oxygen vacancy V_O in ZnO was found in first principles calculations to be such a defect. The singly positively charged (V_O^+) state of this defect was found to be unstable with respect to dissociation into V_O^0 and V_O^{2+} [36, 39, 64]. A negative- U defect can be identified from PAS experiments on as-grown and electron-irradiated samples [104]. It was also suggested that the V_{Zn} defect was a negative- U defect, as PAS reveals that V_{Zn} prefers to be in a double-negative-charge state after electron irradiation [89, 104]. Identification of a defect as negative- U is important for certain issues. A negative- U defect with an unpaired charge is not stable and cannot act as a paramagnetic centre. This is particularly important in explaining the role of defects in DMS and intrinsic ferromagnetism in oxide semiconductors. In Section 2.2 of this chapter we shall discuss different models to explain the role of defects and we will see that a singly-charged defect is essential for almost all the models. In a negative- U defect the doubly-occupied defect energy level is deeper than a singly-occupied level and the transition $\epsilon(2 - /-)$ will have a lower value than the $\epsilon(-/0)$ transition. Transition levels are calculated from first principles calculations and the value of U is given by, $U = \epsilon(2 - /-) - \epsilon(-/0)$. The techniques for estimation of these quantities are discussed in Chapter 4.

2.1.2 Role of defects in optical properties: Photoluminescence

Since defect levels lying in the band gap of a semiconductor may dominate optical transitions in that energy range, tailoring defect concentrations is immensely important for transparent semiconductors such as ZnO, GaAs, GaN and CuAlO₂. For example, ZnO is a UV-bandgap semiconductor but off-stoichiometric samples emit green, yellow and red photoluminescence [5, 11, 40, 106, 107, 108]. The green luminescence peak is associated with an energy of ~ 2.4 eV and is often attributed to electron-hole recombination of transitions from donors, Zn_i or V_O⁺, to deep acceptors V_{Zn}⁻ [106, 109]. This requires both V_O and V_{Zn} to appear in the sample. The yellow emission energy ~ 2.2 eV was assigned by several groups to the radiative recombination of a delocalized electron close to the conduction band edge with a deep trapped hole in the O_i center [40, 107]. In a recent publication, Heo *et al* [11] suggested that the green emission is related to donor-deep acceptor V_{Zn}⁰ → V_{Zn}⁻ transitions and the yellow to donor-deep acceptor V_O → O_i⁻ (negatively charged oxygen interstitial) transition. The yellow luminescence is also observed in the presence of the extrinsic acceptor impurities: Al, H, Li and N [110]. A red/orange coloration [62, 108] is observed in Zn-rich samples annealed at high temperature and was attributed to V_O defects by ODEPR experiments mentioned previously [62]. This coloration is reversible and the samples become transparent upon annealing in O-vapour.

Studenikin *et al* [106] observed a shift from green to blue (2.5 eV) in the ZnO photoluminescence spectrum using a high-intensity laser pulse. Some first-principles calculations assign this signal to the (-/0) or (2-/-) transition of the antisite defect O_{Zn} [111]. This defect has a high formation energy and therefore it is argued that it can only form after under high-intensity laser treatment [111].

2.1.3 First-principles calculations on oxide defects

First-principles calculations using a number of different functionals have been carried out for defects in ZnO. Some of these methods were discussed in Chapter 1 and more detail is given in Chapter 3. A defect system can be simulated by using the crystal structure parameters of the bulk system obtained using x-ray

diffraction experiments and removing an atom from it. Supercell methods are most commonly used in these calculations. A supercell is a large crystal cell created by multiplying the conventional unit cell. A unit cell cannot be used by itself for a defect study. If an atom is removed or substituted in a conventional unit cell, which typically consists of 2 to 10 atoms, the symmetry is heavily disturbed and poorly represents a point defect. Therefore the supercell method is useful here. Being periodic over larger dimensions, it gives the scope of looking into the long-range perturbation due to a defect. The supercell size should be large enough so that the defect concentration is typically 1% or lower, even if only one single atom is modified. Since a supercell is repeated in space, any defect created in the supercell repeats along all directions. This leads to unwanted interactions between the defect and its periodic images, which contribute to the total energy. This problem becomes more prominent when charged defects are involved. The image charges interact in all periodic dimensions and contribute to the total energy. Correction schemes are required to remove the unwanted energy contribution which may be as large as 0.5 eV for small supercells with approximately 40 atoms [55]. This problem and related corrections are discussed in detail in Chapter 4.

In first-principles calculations with supercells one can calculate the total energy of the supercell and charge populations on each atomic site. The charge density is obtained as a function of real space position vector. Eigenvalues of the Kohn-Sham operator can be plotted as the function of wavevector to generate the band structure. Electronic wavefunctions associated with the defects can also be visualised.

Two important quantities related to defects that first-principles calculations can predict are formation energy and transition level. We discuss the significance and estimation techniques of these two quantities in Chapter 4. Kohan *et al* [64] have formulated formation energy of a defect from first-principles total energies of supercells containing a defect and bulk. A defect formation energy is the energy cost to create a defect and comparison of formation energies of different defects gives information on the relative thermodynamic probability of formation of a defect. Comparing formation energies of a single defect in different charge states yields the transition level. A transition level of a defect between two charge states

2.1 Characterisation of vacancy defects

is the value of the Fermi level at which the formation energies for the two different charge states become equal [64].

Transition levels are important parameters in the characterisation of a defect. We mentioned that the value of the Hubbard- U parameter can be estimated from the transition levels. Lany and Zunger [69] have shown that the optical recombination energies associated with defects can be estimated from transition levels and hence the results from the photoluminescence experiments can be directly interpreted. The green luminescence at 2.4 eV is often attributed to the $V_O (+/0)$ transition [69] from first-principles calculations.

Vidya *et al* [111] have recently estimated the same quantities, using PAW-GGA. The results suggests that the green luminescence should be attributed to a V_{ZnO} divacancy rather than a V_O single vacancy. One concern regarding prediction of the optical recombination energy from the transition levels is the accuracy of the value should be high so that the error is lower than at least 0.1eV. This is because the width of most of the PL peaks are in the order of ~ 0.1 eV. Also the energy difference of a green and a yellow signal is ~ 0.2 eV. Occasionally it has been observed that the results differ much more than this error limit whenever a different functional is adapted [21, 63] and certain corrections must be applied.

One of the main concerns regarding first-principles calculations on wide band gap oxide semiconductors is the band gap problem. As we mentioned before, although conventional local density approximation (LDA) is frequently used in first-principles simulations, for large gap oxides and strongly correlated systems, LDA predicts an incorrect electronic structure. LDA assumes that the energy functional for any system varies in the same way as that in a homogenous electron gas (Details of the fundamentals of density functional theory and LDA are discussed in Chapter 3). LDA incorporates an artificial self interaction of electrons and also lacks the derivative discontinuities of the exchange-correlation potential with respect to occupation number [112]. This results in underestimation of the band gap. The presence of defects makes the calculation more complicated as the electron density varies rapidly at or near the defect site. Due to the band gap problem, the defect states are incorrectly described and the formation energy of defects include a large error, especially for charged defects [21].

A number of algorithms and correction schemes have been proposed to solve this problem such as LDA+U [113, 114], the generalised gradient approximation (GGA) [30], GGA+U [113], self-interaction correction (SIC) schemes [115], atomic-SIC [45] and hybrid Hartree-Fock-DFT [34]. A combination of two different methods is used sometimes. Rinke *et al* [116] combined LDA and GW methods to study self-interstitial defects in silicon. LDA was used for the crystal structure relaxation of a large supercell calculation and GW was used for charged defects at fixed geometries. This is a very useful way of performing defect calculations with large supercells quickly. LDA is a fast algorithm but leads to incorrect defect states. GW perturbative method, on the other hand, is theoretically more elegant but computationally very expensive. Adding GW at the end of a large supercell structural calculation using LDA, makes the whole process significantly faster and more accurate as well. The only drawback of combined methods like this is that, these methods do not take into account the fact that the structural changes may be affected by charging of a defect. We will show in Chapter 5 and 6 of this thesis that charging of defects does have a large effect on structural changes and therefore combined methods may not always be applied.

Anisimov *et al* [114] have applied a finite Coulomb U to the basic LDA functional. This approximation can predict the band-gap of these system correctly [64, 114]. In this approach, the electrons are divided into two subsystems consisting of localised d and f states and delocalised states [113]. The localised states are modelled by introducing a Coulomb repulsion term U , similar to the Hubbard- U in the Hamiltonian where the delocalised states are modelled by standard LDA. This method focuses on correcting the band gap in agreement with experiments by adjusting U but may lead to other errors [117]. When defects are introduced, LDA+ U leads to incorrect energy levels for the defect states [36, 64, 118] and the value of U must be estimated for each of the different defects.

Another method often used to correct the band gap error of LDA is the self-interaction correction (SIC) [115]. This method introduces a correction term in the Hamiltonian to explicitly remove the electron self-interaction induced by LDA. The implementation of this method to periodic solids is not straight-forward and computationally expensive.

2.1 Characterisation of vacancy defects

The band gap problem in semiconducting oxides can be corrected by introducing a non-local exchange in hybrid density functionals. Hybrid functionals include Hartree-Fock-like exchange in the exchange-correlation functional. This significantly improves the predictions of certain parameters such as atomisation energies, bond lengths and vibrational frequencies [34]. We discuss the philosophy behind the development of hybrid functionals and the techniques used to counter the band gap problem in Chapter 3. Here different results related to oxide defects studied by a number of groups using hybrid functionals are described.

The band gap predicted by hybrid functionals can be adjusted to agree with experiment by tuning the amount of non-local/exact exchange used in the exchange-correlation functional. Fixing the band gap might lead to incorrect prediction of other physical parameters such as bond-lengths or vibrational frequencies. Hence the method must be evaluated on the basis of experience with a number of materials [119]. The calculation of non-local exchange is computationally expensive and therefore large supercell calculations can not be easily performed.

Oba *et al* [63] have examined hydrogen interstitials and oxygen vacancies in ZnO using HSE [33] hybrid functionals with finite-supercell corrections and observed significant improvements over LDA and LDA+U methods. For example, The band gap was calculated to be 3.4 eV which is close to the experimental value of 3.47 eV [56]. LDA underestimates the band gap to ~ 0.2 eV [64]. The 2+/0 thermodynamic transition level of the oxygen vacancy V_O is estimated to be 1.2 eV below the conduction band minimum (CBM) whereas uncorrected LDA/GGA yields ~ 0.1 eV and band gap corrected values (LDA+U/GGA+U) values are around 2.2 eV [64]. The hybrid result is supported by photoluminescence experiments [11, 111]. The formation energy of V_O was estimated to be ~ 1 eV in contrast to an unusually large value of 3.7 eV yielded by LDA+U calculations.

The B3LYP hybrid functional [34] was used in a study on V_O and a much deeper transition level for 2+/0 of 3 eV below the CBM [36] was reported. Agoston *et al* [120] studied V_O in ZnO, In_2O_3 and SnO_2 to compare results between LDA/GGA and hybrid functionals. The results indicated that band gap underestimation in LDA/GGA can lead to incorrect physical conclusions of the role of defects as a source of n-type conductivity. For ZnO, hybrid functional calculations suggest that only a small fraction of the donor level electrons induced

by V_O vacancy-type defects are activated at ambient temperature [120]. n-type conductivity is therefore predicted to be caused by photo-excitation or hydrogen impurities. A long decay time has been observed for photo-conductivity in ZnO [120], which is supported by calculations, which show a large relaxation associated with V_O vacancy defect. For In_2O_3 and SnO_2 , the V_O vacancy was found to be a shallow donor defect with a low formation energy under oxygen deficient growth conditions and may be contribute to n-type conductivity [21, 120].

2.2 Defect related ferromagnetism in oxides

It is widely believed that defects play a role in the ferromagnetism which is observed in many experiments with non-magnetic oxides and in dilute magnetic semiconductor oxides (DMS) [15, 18, 92, 93]. Dietl *et al* [12] predicted that a very dilute impurity of transition metal in non-magnetic semiconductors can lead to room-temperature ferromagnetism. Different models are proposed in order to explain ferromagnetism in DMS's. Experimental studies found evidence to suggest that the ferromagnetism of DMS is related to defects and impurities in thin film samples [14, 15]. In the case of oxides, the oxygen vacancy defect is thought to be responsible and the models proposed to explain ferromagnetism in these materials involve a role for the oxygen vacancy in ferromagnetism [15, 92]. In recent years there have been reports of room-temperature ferromagnetism in undoped oxide films [18, 19]. The results hint that the source of the magnetic moment does not lie in transition metal impurities present in the oxide, but in the defects and demand a model that can describe the mechanism of defect-related magnetism in oxide semiconductors, transition metal doped or not. Some of the models that are relevant to this work are described in the following sections. The new model proposed in this work is also discussed.

2.2.1 The Magnetic Polaron and Impurity Band-Exchange Models

In dilute magnetic semiconductors it is believed that unpaired charge carriers bound to a defect by electrostatic interactions may have an exchange overlap with

2.2 Defect related ferromagnetism in oxides

dilute transition metal (TM) ions in their vicinity and form spin-polarised bound magnetic polarons (BMP) [15]. In practice, vacancy defects are created while annealing sample films in high vacuum. The vacancy traps an unpaired charge carrier and binds neighbouring anti-parallel spin TM d -states by s - d -exchange into a BMP [15, 93]. It is found from positron annihilation spectroscopy (PAS) that vacancy defects are quite efficient in trapping charge carriers, depending on the electrostatic environment [104]. According to the impurity band exchange model [15], the polaron wavefunction can be described as a hydrogenic wavefunction given by,

$$\psi(r) \sim \frac{1}{\sqrt{a_B^3}} e^{-r/a_B} \quad (2.7)$$

where $a_B = \epsilon(m/m^*)a_0$, is the confinement radius, ϵ , m , m^* and a_0 are the static dielectric constant, the absolute mass, effective mass of the polaron, and the Bohr radius, respectively.

The Hamiltonian that governs the interaction between the spin of the donor level and the impurity magnetic moments is given by [15, 121],

$$H = - \sum_i J |\psi(r)|^2 a_0^3 \mathbf{S}_i \cdot \mathbf{s}(\mathbf{R}_i), \quad (2.8)$$

where \mathbf{S}_i is the TM spin located at \mathbf{R}_i , coupling with the carrier spin density $\mathbf{s}(\mathbf{r})$ by local exchange coupling J . The temperature dependence of polaron percolation can be easily established. Using Eqn. 2.7 and 2.8, we have, at thermodynamic equilibrium [121],

$$k_B T = |J| (a_0/a_B)^3 (\mathbf{S} \cdot \mathbf{s}) e^{-2R_p/a_B} \quad (2.9)$$

where,

$$R_p(T) = (a_B/2) \ln \{ \mathbf{s} \cdot \mathbf{S} |J| (a_0/a_B)^3 / k_B T \}, \quad (2.10)$$

i.e. the radius of the hydrogenic donor electron state at temperature T [121]. The radius of the donor state is important since the impurity spins that are at a distance $r \leq R_p$ from a localized carrier tend to align anti-parallel with the localized carrier spin. Since the TM impurity moment originates from a number

of unpaired electrons in d-orbitals and is larger than the carrier spin-moment, the net moment is always ferromagnetic. The localized donor state must interact with many TM cations ($\nu > 10$ [15]) in order to stay spin polarized. Eqn. 2.10 implies that at certain temperature, the donor electronic wavefunctions become too small to percolate and ferromagnetic order breaks down.

The Curie temperature has been estimated to be,

$$T_c = \sqrt{[\mathbf{S}(\mathbf{S} + 1)\mathbf{s}^2 n x_d \delta / 3] J \omega_c / k_B}, \quad (2.11)$$

where x_d is the doping concentration, n is the donor electron concentration, δ is the defect density ratio ($\delta = n_{vacancy}/n_{oxygen}$) and ω_c is cation volume fraction (typically 6%) [15].

When the donor state is delocalized, the expression for T_c becomes

$$T_c = [\mathbf{S}(\mathbf{S} + 1)\mathbf{s}^2 n x_d \delta / 3] J^2 \omega_c^{2/3} / k_B \epsilon_F, \quad (2.12)$$

However the value of T_c is reduced below 1K for a practical example [15].

The model clearly suggests that the donor electron density should be large in the vicinity of a TM impurity in order to increase the Curie temperature. The donor electrons are required to be redistributed largely over the impurity sites (Fig. 2.2).

Pemmaraju *et al* [45] suggested another model based on coupling between Co^{2+} ion-oxygen vacancy pairs in $\text{Zn}_{1-x}\text{Co}_x\text{O}$. Atomic self-interaction corrected (ASIC) DFT was used in the calculation of the electronic structure of $\text{Zn}_{1-x}\text{Co}_x\text{O}$. A two-centre model is proposed where the substituted Co^{2+} ions couple antiferromagnetically with an oxygen vacancy (V_O) nearby and form a $\text{Co}^{2+} - V_O$ pair. These pairs can interact at long range and produce a net ferromagnetic moment. Monte Carlo simulations have been carried out at finite temperature to show that this model is consistent with room temperature ferromagnetism [45].

2.2.2 Hubbard model: Room temperature ferromagnetism

The Hubbard model is a simplification of the many body problem. There is a simple assumption that, out of a number of levels, only one band plays a dominant role in the ground state properties [61]. The Hamiltonian for the Hubbard

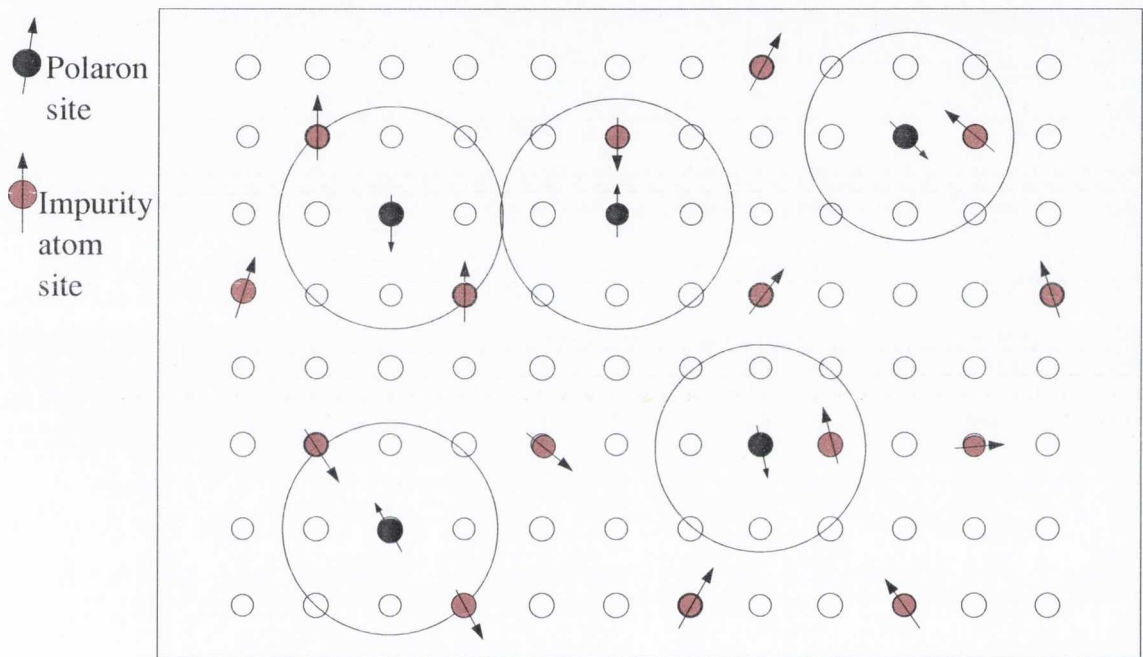


Figure 2.2: Schematic diagram of a bound polaron model. A net ferromagnetic moment is retained as long as the polaron wavefunction percolates. As the temperature rises, polaron radius decreases (Eqn. 2.10) and percolation ceases above the Curie temperature.

model contains only two terms. A term diagonal in the states i , counting doubly occupied levels which is multiplied by a positive energy U and represent the on-site Coulomb repulsion. Another term is off-diagonal and accounts for inter-site fermion hopping, multiplied by a hopping parameter t_{ij} . The second quantized Hamiltonian in the Hubbard model is given by,

$$H = - \sum_{i,j,\sigma} (t_{ij} - \mu) c_{i\sigma}^\dagger c_{j\sigma} + \frac{1}{2} U \sum_{i,\sigma} n_{i\sigma} n_{i-\sigma}, \quad (2.13)$$

where c^\dagger and c are fermion creation and annihilation operators respectively, t , μ , and U are the hopping parameter, the chemical potential and on-site Coulomb repulsion. The number operator is $n_\sigma(\mathbf{r}) = c_{i\sigma}^\dagger(\mathbf{r})c_{i\sigma}(\mathbf{r})$. The model was first applied to a 1D hydrogen chain [61]. With perfect half-filling, in the limit of negligible on-site repulsion ($U \ll t$), it yields a metallic band. It yields a Heisenberg antiferromagnet in the other extreme limit $U \gg t$.

Nagaoka [122] did a rigorous analytical derivation to prove that for very large U in lattice sites ordered in simple cubic (SC), body centered cubic (BCC), face centered cubic (FCC), or hexagonal closed packed (HCP) lattices, a finite spin may be observed for electrons $n = N+1$. N is the number of sites. The theorem also requires $t > 0$ as a necessary condition, t being the hopping parameter. The theorem proves that in this condition the maximum total spin can be given by $S_{max} = n/2$.

For most of the defects in wide band-gap systems, the defect state lies in the band gap of the energy-band diagram. A defect state like this can be described by a Hubbard Hamiltonian of the form in Eqn. 2.13. If such a band exhibits large U and moderate bandwidth, then at partial-fillings of the defect band greater than half-filling, the state will trap one electron completely and another electron partially, which will hop between defect sites and yield a ferromagnetic polarization between all defect sites. This is because the kinetic term in Eqn. 2.13 always favours a FM-aligned system, such that the partially-bound electron can roam freely through all sites.

Magnetic phase diagrams for the Hubbard model as a function of band occupation and temperature have been calculated by several groups. High temperature

series expansion (HTSE) [67], spectral density approach (SDA) [123], dynamic mean field theory (DMFT) [124] and quantum Monte Carlo (QMC) [68] calculations predict systems with parallel-spin orientation at finite temperatures which depend on lattice structure and band filling. These phase diagrams suggest that, a finite-spin solution can be obtained at fractional band-fillings greater than half-filling. A necessary condition for a solution where partially filled sites are aligned parallel is that the ratio between the on-site Coulomb repulsion and hopping parameter (U/t) should be greater than a critical constant, which depends on the lattice structure. For example, SDA calculations show that for a SC lattice, a U/W ratio, W being the bandwidth, greater than unity is essential to retain a net finite spin for temperature $> 300\text{K}$ [123].

The Hubbard model and the simple cubic phase diagrams can be used to explain ferromagnetism in an ordinary cubic lattice. It is postulated in this work that defects with large U can interact and retain a parallel-spin configuration at finite temperatures [68, 122]. The hopping parameter can be determined from the bandwidth (W) of the defect band. A moderate bandwidth of the defect level is desirable. A very small bandwidth will not allow the electrons to hop between neighbouring defect sites, which is essential for long range interaction, and a large band width will reduce the U/W factor which should fall in the ferromagnetic region in the phase diagram. This model has the potential to explain the experimentally observed room temperature ferromagnetism in transition-metal doped [15, 43] and intrinsic semiconductor oxides [18] as a defect-related phenomenon.

A similar model has been presented by Bouzerar *et al* [92] for finite systems. The Hubbard parameters of the correlated oxygen states were calculated for different oxides. The unrestricted Hartree Fock (UHF) method was used in their calculations. The Curie temperature was calculated from the exchange constants and they predict room temperature ferromagnetism at a low defect/impurity concentration.

The real deviation between theory and practice is that in all these algorithms, calculations are made assuming a lattice ordering, mainly cubic. But the defect sites in oxide thin films are not on a lattice and it is impossible to predict the exact defect geometry and the effect of disorder on the phase diagram.

However, recent work by Nielsen and Bhatt [125] which considered both ordered and disordered lattices in Hubbard model, showed that within Nagaoka's conditions ($U/t \rightarrow \infty$ and $n = N+1$), a parallel-spin configuration is favourable. The phase diagrams obtained in this work also suggest that the $U/t \rightarrow \infty$ condition may not be strictly obeyed and for large but finite U/t , partially filled disordered systems away from half-filling can retain a finite spin.

Chapter 3

Computational Methods

3.1 Hartree-Fock and Density Functional Theory

The density functional method described in the Thomas-Fermi model [126, 127] paved the way for the density functional theory (DFT) proposed by Hohenberg and Kohn [128] for effectively simulating quantum mechanical problems using computers. The central concept of this theory is to describe the electronic structure of a particular system by calculating the electron density $n(\mathbf{r})$ as a function of position vector \mathbf{r} . This is done by reducing the many-body problem of interacting electrons in a static potential to a problem with non-interacting particles moving in an effective potential. This potential is calculated as a functional of the charge density function. The mathematical approach is explained below. For the last half century, the basic concept of DFT remained the same but the accuracy of the computations significantly increased as new algorithms and functionals became available. As the speed of the computers increased exponentially in the last few years, computational techniques such as parallel computing opened up the scope for extensive and more realistic simulations. Modern day simulation does not only calculate charge density and total energy but can also reproduce the results of a wide range of experiments such as atomic force microscopy (AFM) [23] or X-ray magnetic circular dichroism (XMCD) [24].

DFT simplifies the many-body problem by reducing the dimensionality. A

system of N non interacting particles has $3N$ degrees of freedom. DFT reduces the number of degrees of freedom to 3 since it requires only the total density functional $\rho(\mathbf{r})$, which minimises a total energy functional. This is achieved by solving a self-consistent field matrix eigenvalue problem which can be solved by only order of M^3 operations (M is the number of independent electronic wave functions and is in the order of N). Since there are many assumptions involved and the calculations are not exact in most many-body simulations, results often deviate from experimentally obtained results. Thus the assumptions which need to be carefully considered depend on the electronic structure of the material. New calculation algorithms and correction schemes are being devised by computational physicists in order to keep up with the experimental data produced. The calculation scheme adopted in this work is described in the following sections. Comparison with experimental results has been made and the computational parameters have been chosen on the basis of experience and a number of literature reviews.

3.1.1 Hartree Fock Theory

The Born-Oppenheimer approximation is considered for calculating fixed ionic geometry calculations since this approximation removes the necessity of calculating the nuclear wavefunction by assuming that the nuclei are frozen in their respective atomic sites. Hence the kinetic energy term for the nuclei can be dropped and time-independent Schrödinger equation can be written as,

$$(\hat{T} + \hat{V}_{ee} + \hat{V}_{ext})\psi(x_1, \dots, x_N) = E\psi(x_1, \dots, x_N) \quad (3.1)$$

Where ψ is the many particle wavefunction and the operators are the kinetic energy,

$$\hat{T} = -\frac{1}{2} \sum_{i=1}^N \nabla_i^2, \quad (3.2)$$

the external potential energy,

$$\hat{V}_{ext} = \sum_{i=1}^N v(\mathbf{r}_i), \quad (3.3)$$

3.1 Hartree-Fock and Density Functional Theory

where $v(\mathbf{r}_i)$ are the Coulomb potentials on i -th electron. The electron-electron repulsion is given by,

$$\hat{V}_{ee} = \frac{1}{2} \sum_{i \neq j}^N \frac{1}{|\mathbf{r}_i - \mathbf{r}_j|} \quad (3.4)$$

\mathbf{r} is the electronic spatial coordinate.

The ground state energy is obtained by minimizing the total energy functional using the variational principle. As electrons are fermions, the total wave function must be antisymmetric with respect to the interchange of any two of the electrons. Thus the total wavefunction ψ can be represented as the antisymmetric linear combination of the wavefunction of the i -th electron ϕ_i , given by the Slater determinant,

$$\psi = \frac{1}{\sqrt{N!}} \begin{vmatrix} \phi_1(\mathbf{r}_1) & \phi_1(\mathbf{r}_2) & \dots & \phi_1(\mathbf{r}_N) \\ \phi_2(\mathbf{r}_1) & \phi_2(\mathbf{r}_2) & \dots & \phi_2(\mathbf{r}_N) \\ \vdots & \vdots & \ddots & \vdots \\ \phi_N(\mathbf{r}_1) & \phi_N(\mathbf{r}_2) & \dots & \phi_N(\mathbf{r}_N) \end{vmatrix} \quad (3.5)$$

Hence, the interaction between two particles yields two contributions due to the antisymmetric nature of the wavefunction:

$$\langle \psi | \hat{V}_{ee} | \psi \rangle = E_C[\psi] + E_x[\psi]. \quad (3.6)$$

The two terms are direct (Coulomb) and exchange integrals respectively,

$$E_C[\phi] = \frac{1}{2} \sum_{\sigma} \sum_{i,j} \int d^3r \int d^3r' \frac{\phi_{i\sigma}^*(\mathbf{r}) \phi_{j\sigma}^*(\mathbf{r}') \phi_{i\sigma}(\mathbf{r}) \phi_{j\sigma}(\mathbf{r}')}{|\mathbf{r} - \mathbf{r}'|} \quad (3.7)$$

$$E_x[\phi] = -\frac{1}{2} \sum_{\sigma} \sum_{i,j} \int d^3r \int d^3r' \frac{\phi_{i\sigma}^*(\mathbf{r}) \phi_{j\sigma}^*(\mathbf{r}') \phi_{i\sigma}(\mathbf{r}') \phi_{j\sigma}(\mathbf{r})}{|\mathbf{r} - \mathbf{r}'|} \quad (3.8)$$

In 3.8 the sum over σ is restricted to *parallel spins* and each of the functions $\phi_i(\mathbf{r})$ satisfies a one electron Schrödinger equation. This is called the Hartree-Fock approximation (HFA). Eqn. 3.1 is solved in a self-consistent procedure.

The Hartree-Fock approximation involves explicit exchange interactions between all occupied orbital wavefunctions and excludes the self-interaction of electrons, therefore bringing down the energy eigenvalues of the filled levels. In HFA, the Coulomb repulsion is completely unscreened. This yields a band gap which usually overestimates the experimental band gap (For some strongly correlated systems HF yields a much better value of band gap). Overestimation of the band gap by the HFA is a major disadvantage and since it includes explicit exchange calculation between all basis orbitals, it is expensive in computation as well.

3.1.2 Density Functional Theory

DFT includes exchange and correlation effects. Modern DFT, introduced by Kohn [22, 128], is based upon two theorems:

- 1 . The electron density $n(\mathbf{r})$ in the ground state is a functional of the external potential $V_{xc}(\mathbf{r})$
- 2 . The exchange-correlation potential $V_{xc}(\mathbf{r})$ is a unique functional of the density $n(\mathbf{r})$. [128]

The total energy of the full, many-body problem of interacting fermions is expressed as a functional of the charge density $n(\mathbf{r})$ defined by,

$$n(\mathbf{r}) = \sum_i^{\text{occupied}} \int |\phi_i(\mathbf{r})|^2 d\mathbf{r} \quad (3.9)$$

Assume a set of normalised Kohn-Sham orbitals ϕ_i , which are solutions to a set of single-particle Schrödinger equations, known as Kohn-Sham equations

$$\left[-\frac{\hbar^2}{2m}\nabla^2 + V_H(\mathbf{r}) + V_{xc}(\mathbf{r})\right]\phi_i = \epsilon_i\phi_i \quad (3.10)$$

V_H represents combined electron-nuclear potential and electron-electron Coulomb potential. V_{xc} is the exchange-correlation potential.

In practice, the functional containing exchange and correlation effects is not known exactly (HFA explicitly calculates exchange using Eqn. 3.8 and may be

3.1 Hartree-Fock and Density Functional Theory

included in the DFT algorithm. This is known as an exact-exchange functional. The exact correlation functional, on the other hand, can be calculated exactly for the homogeneous electron gas only) Kohn and Sham [22] applied a simple local density approximation (LDA) to the limiting case of a slowly varying electron density, for which the exchange-correlation energy is given by:

$$E_{xc}^{LDA}[n] = \int d\mathbf{r} n(\mathbf{r}) \epsilon_{xc}[n] \quad (3.11)$$

and

$$V_{xc} = \frac{\delta E_{xc}^{LDA}[n]}{\delta n(\mathbf{r})}, \quad (3.12)$$

where ϵ_{xc} is the exchange-correlation energy per particle of a homogeneous electron gas with density $n(\mathbf{r})$. LDA becomes a self-consistent procedure by minimising the total energy. Convergence of this self-consistent procedure is achieved by the variational property of the total energy functional

$$\frac{\delta E}{\delta n} = 0 \quad (3.13)$$

given that,

$$\int n(\mathbf{r}) d^3r = N \quad (3.14)$$

where N is number of electrons.

We have discussed in Chapter 2 that LDA tends to underestimate the energy gap in solids, especially for strongly correlated electron systems [27, 28, 29] where Hartree-Fock overestimates it. In LDA, spurious self-interaction is nearly cancelled in the total energy integration but it is included in orbital-independent one-electron potential [29] which reduces the energy gap. The Van der Waals interaction, which originates from correlated motions of electrons caused by Coulomb interactions between distant atoms cannot be described properly by LDA or any other mean-field approach. Hence for strongly correlated electron systems like FeO, CoO, CaCuO₂ or La₂CuO₄ as well as the wide gap oxides such as ZnO [36, 64] and CuAlO₂ [129], LDA fails to predict the correct ground state for the

magnetic systems and the energy gaps of all wide gap systems are severely underestimated [27, 28]. Anisimov et al [29] later augmented the LDA by a finite Coulomb repulsion U . LDA+ U yields more accurate values of energy levels in strongly correlated systems, but it still tends to underestimate transition levels of charged defects in ZnO [90].

3.2 B3LYP hybrid DFT functional

Since DFT calculations show a trend of underestimating the energy gap in strongly correlated systems, and Hartree-Fock calculations overestimate it, a solution was sought in hybrid HF/DFT methods. B3LYP hybrid DFT involves the Lee Yang Parr (LYP) correlation functional [130], the Becke3 [34] exchange functional and Vosko-Wilks-Nussair (VWN) correlation functional [131], along with traditional LDA and HF exchange. The B3LYP functional is quite successful in strongly correlated systems. We have discussed before that the inclusion of self-interaction in LDA leads to the underestimation of the band gap in correlated systems. The reason for this success lies in the reduction of self-interaction by the introduction of HF exchange along with the use of a better correlation-functional that takes dynamical correlation effects into account. This results in larger exchange splitting and better prediction of magnetic moments in spin-polarised materials [132]. The main concept of this functional is that it incorporates combinations of Hartree-Fock exchange and conventional density functional approximations to exchange with weights that sum to unity. These weight factors are determined from linear least square fits to the results of thermochemistry experiments [132, 133]. The least squares fit was based on a large database [119] created by computation on organic molecules. Although organic molecules have much different electronic structures than wide-gap oxides, surprisingly the fit works quite accurately for oxides also. Comparison with experiment shows that measurable quantities such as band gap, energy levels, lattice parameters and magnetic exchange coupling constants are in good agreement with experiments. The order of error in these quantities are as follows. Band gap: O(0.1 eV) [36, 38], lattice parameters: O(1%) [132, 134, 135], vibrational frequencies: O(10 cm⁻¹) [136, 137] for systems such as ZnO, CaCuO₂, Fe₃O₄, BaTiO₃ and a number of oxides.

B3LYP is not the best functional for metallic systems [138] due to the lack of a proper description of free-electron-like systems with a significant itinerant character [139, 140], but for wide band gap systems and strongly correlated electron systems it yields much better results for measurable parameters described before. Other hybrid functionals such as PBE0 [30], HSE [33, 141] and B3PW91 [142] are also found to be free of the band-gap related problem which LDA experiences [143] but are inaccurate in describing metallic systems for the same reason as B3LYP [140]. Hafner [140] and Paier [139] have shown that when it comes to description of solid state properties such as lattice parameters and bulk moduli of wide-gap systems, the performance of B3LYP is slightly worse than HSE or PBE0, but, having three tunable empirical parameters allows B3LYP to achieve high accuracy in multiple properties with a single calculation [140].

The total exchange correlation functional in B3LYP is given by:

$$E_{xc} = (1 - A)(E_x^{LDA} + BE_x^{Becke}) + AE_x^{HF} + (1 - C)E_c^{VWN} + CE_c^{LYP} \quad (3.15)$$

where, A, B and C are weight parameters. Experience with a range of oxides [38, 132, 144, 145, 146] shows that the particular choice of conventional density functional approximation used in combination with the Hartree-Fock exchange does not change predicted values for exchange constants by a large amount [37]. On the other hand, experience shows that band gaps of oxides are more accurately predicted with weights for Hartree-Fock exchange around 0.2 [36, 38, 132, 144, 145, 146]. Undoubtedly B3LYP estimates a very good result in agreement with experiment for ZnO. The band gap of ZnO predicted by B3LYP, 3.2 eV [36, 39], is in reasonably good agreement with experiment, 3.47 eV [56]. In this work the lattice parameters are predicted to be 3.28 Å and 5.27 Å in comparison to experiment values of 3.25 Å and 5.21 Å, respectively [56].

The B3LYP functional with HF weight of 0.2 is used throughout the current work (in some calculations LDA is used in order to compare with other published work using LDA). In the case of magnetite in its low temperature insulating state the band gap is overestimated by conventional B3LYP [137] (0.9 eV). It is shown that a lower HF weight yields a band gap closer to the experimental gap (Chapter 8). A HF weight factor of 0.15 yields a band gap of 0.4 eV compared to the experimental value of 0.15 eV. However it is a subject of concern that whether

manipulating the HF weight factor to correct the band gap will lead to wrong prediction of other key parameters such as lattice and exchange parameters. In the case of magnetite in low temperature, lattice parameter predicted using HF weight of 0.15 are in better agreement with experiment than using the standard 0.2 [137].

3.3 The CRYSTAL code

The CRYSTAL [147] code used in this work, uses a Gaussian orbital basis to expand wavefunctions. CRYSTAL treats each crystalline orbital (CO), $\psi_i(\mathbf{r}, \mathbf{k})$, as a linear combination of Bloch functions, $\phi_\mu(\mathbf{r}, \mathbf{k})$, defined in terms of local functions, $\varphi_\mu(\mathbf{r})$ (namely atomic orbitals, AOs).

$$\psi_i(\mathbf{r}, \mathbf{k}) = \sum_{\mu} a_{\mu,i}(\mathbf{k})\phi_{\mu}(\mathbf{r}, \mathbf{k}) \quad (3.16)$$

According to Bloch's theorem, the orbital wavefunctions of periodic systems with lattice vector, \mathbf{T} can be written as $\psi(\mathbf{r} + \mathbf{T}) = \psi(\mathbf{r})e^{i\mathbf{k}\cdot\mathbf{T}}$. \mathbf{k} is the wavevector and is the Fourier conjugate of the position vector \mathbf{r} . The mathematical form of these functions are given by,

$$\phi_{\mu}(\mathbf{r}, \mathbf{k}) = \sum_{\mathbf{T}} \varphi_{\mu}(\mathbf{r} - \mathbf{A}_{\mu} - \mathbf{T})e^{i\mathbf{k}\cdot\mathbf{T}} \quad (3.17)$$

\mathbf{A}_{μ} denotes the coordinate of a nucleus in the zeroth lattice cell on which φ_{μ} is centered and summed over all lattice vectors \mathbf{T} . The local functions are expressed as linear combinations of n individually normalized Gaussian functions G characterized by the same centre, with fixed coefficients d_j and exponents α_j defined in the input:

$$\varphi_{\mu}(\mathbf{r} - \mathbf{A}_{\mu} - \mathbf{T}) = \sum_j^n d_j G(\alpha_j, \mathbf{r} - \mathbf{A}_{\mu} - \mathbf{T}) \quad (3.18)$$

where,

$$G(\alpha_j, \mathbf{r} - \mathbf{A}_{\mu} - \mathbf{T}) = e^{-\alpha_j(\mathbf{r} - \mathbf{A}_{\mu} - \mathbf{T})^2} \quad (3.19)$$

Hence the initial density $n(\mathbf{r})$ can be computed from the wavefunctions $\psi_i(\mathbf{r}, \mathbf{k})$ using Eqn. 3.9 as a function of \mathbf{r} for fixed values of \mathbf{k} known as k-points. The k-points are sampled from the Brillouin zone corresponding to the lattice cell. Monkhorst and Pack [148] proposed a method of choosing a set of k-points. It is a rectangular grid of evenly spaced points of dimensions $N_x \times N_y \times N_z$. The accuracy of the calculation is dependent on the density of sampling. The optimum grid size can be established from a convergence test where the total energy is plotted with respect to increasing number of k-points. Generally, the total energy decreases rapidly and then oscillates with decay as the number of k-point increases. When the oscillation amplitude reduces below a certain tolerance limit, k-point convergence is deemed to be achieved.

The self consistent field calculation of DFT requires diagonalisation of the eigenvalue equation 3.10 which gives the eigenvalues $\epsilon_i(\mathbf{k})$ as continuous functions of \mathbf{k} . When the diagonalisation is numerically computed, the density of the 3-dimensional k-point grid is a deciding factor in the accuracy of the eigenvalues $\epsilon_i(\mathbf{k})$. On the other hand increasing the number of k-points will increase the required computer-time as a function $T = 3^N \times T_{diag}$ where T is the required time that will increase by increasing the number of k-points by N. T_{diag} is the time needed for diagonalisation of the eigenvalue matrix at a single k-point. An optimum value for the k-point density must be observed, obtained from k-point convergence test, in order to obtain the best results. CRYSTAL uses parallel computing techniques and in a computer cluster system it distributes the diagonalisation of the eigenvalue matrix to different computing processors for different k-points. This speeds up the computation by a large amount.

Another important issue regarding the computational technique is the choice of basis set. The dependency of the accuracy of computation on different basis sets is discussed in Chapter 4. The basis sets used here for different atomic orbitals of different elements are generated by CRYSTAL authors and others, which are available online at <http://www.crystal.unito.it>

3.3.1 Localised orbital *vs.* plane-wave basis sets

It was mentioned before that CRYSTAL uses localised orbital Gaussian basis sets. Some simulation codes such as VASP (Vienna Ab-initio Simulation Package) [149] and Quantum Espresso [150] use plane-wave orbital basis sets of the form

$$\phi_{n\mathbf{k}}(\mathbf{r}) = u_n(\mathbf{r})e^{i\mathbf{k}\cdot\mathbf{r}} \quad (3.20)$$

where,

$$u_n(\mathbf{r}) = \sum_{\mathbf{K}} C_{n,\mathbf{K}} e^{i\mathbf{K}\cdot\mathbf{r}} \quad (3.21)$$

\mathbf{K} is a reciprocal lattice vector. Hence the wavefunctions are given by,

$$\phi_{n\mathbf{k}}(\mathbf{r}) = \sum_{\mathbf{K}} C_{n,\mathbf{K}} e^{i(\mathbf{k}+\mathbf{K})\cdot\mathbf{r}} \quad (3.22)$$

The main advantages of using a plane-wave basis sets are:

1. A plane-wave basis set, used in combination with a pseudopotential (an effective-core potential) in a calculation is faster than an all-electron localized-orbital basis set. This is because the pseudopotential removes the necessity of calculating the core charge density.
2. A plane wave basis is independent of atomic sites, and therefore the calculations of forces on atoms are computationally less demanding.
3. A plane-wave basis is parameterised only by a cutoff energy and it converges in a smooth and monotononic manner to the desired wavefunction and it does not exhibit basis-set superposition error (BSSE). BSSE arises from the overlapping of neighbouring-site localised orbitals which effectively increases the number of basis sets per atomic site and contributes to the total energy.

The main disadvantages of plane-wave basis sets are:

1. In a plane-wave basis set the number of orbital wavefunctions is very large and therefore calculation of an exact exchange using this basis is extremely expensive in computer time. This is because the exchange matrix elements have to be computed between every set of pairs of orbital wavefunctions. This is very important for the current work since a Hartree-Fock-LDA hybrid DFT method is adopted.

2. A plane wave has to use a pseudopotential to describe the core electrons of a small ion such as oxygen and tend to be concentrated very close to the atomic nuclei. This results large wavefunctions and density gradients near the nuclei which are not correctly described by a plane-wave basis set, unless a very high energy cutoff, and therefore a small wavelength, is used.

Despite of the fact that the advantages of using a plane-wave basis clearly supersedes its disadvantages, localised-orbital basis sets are used in this work for the following reasons,

1. A localised orbital basis features a lower number of wavefunctions in comparison to its plane-wave counterpart (in the order of magnitude of the number of atomic orbitals of a corresponding atom) and is most suited for the current work as the hybrid Hartree-Fock exchange functionals are involved.

2. A localised orbital basis set can describe the core potential in an exact all-electron wavefunction which is important for small-core atoms such as oxygen so one does not have to worry about basis set convergence problem for small-core systems.

The main disadvantages of localised orbital basis sets are:

1. Unlike the plane-wave basis sets, the localised orbital basis sets are not parameterised to only the energy cutoff and has to be explicitly described for all different species of atoms. Transferability of these basis sets are therefore questionable and have to be tested before using in a modelling of a new material.

2. BSSE is a major drawback of localised orbital basis sets. This can be corrected by computing the error by repeating all the calculations using a mixed (overlapped) basis set, and the error is then subtracted a posteriori from the uncorrected energy [151]. The mixed augmented local orbital basis sets are formed by introducing *ghost orbitals*, basis set functions which have no electrons or protons centered on interstitial sites.

3.4 The EXCITON code

The EXCITON code, developed by the electronic structure theory group in the School of Physics, TCD [152] takes the wavefunctions generated by CRYSTAL as input and can produce contour maps and 3-D visualizations of the electronic

structure in periodic systems. Wave function isosurface plots shown in this thesis to visualize bound polarons and other electronic states were drawn using EXCITON and the visualization interface of the XCrysDen [153] code was used.

Chapter 4

Estimation of Defect Formation Energies and Transition Levels

4.1 Defect and impurity formation Energy

Defects and impurities dominate a number of important properties of semiconductors. Concentrations of intrinsic defects, as well as dopants, are therefore controlled in the growth of semiconductor devices in order to achieve certain technical applications. Defects and impurity dopants make the material either n- or p-type, and also control recombination rates and contribute to optical absorption and luminescence [5]. For wide-band-gap semiconductor materials, knowledge of defect levels and transition probabilities is particularly important, as the control over the conductivity and emission colours are the key to optoelectronic device design.

In this work formation energies of intrinsic defects in ZnO are computed and defect transition energies are estimated using LDA and B3LYP Hybrid DFT computation techniques discussed in Chapter 3. The importance of these quantities and their interpretations are discussed in Chapter 2. The formation energy represents the energy cost associated with a particular defect formation in a solid. In this case we focus on intrinsic point defects, so the formation energy will be the energy required to remove (vacancies), add (interstitials) or swap (antisites) an atom in a solid. Correct estimation of formation energies from first-principles methods has been extensively studied by several groups and the simplest way to

4.1 Defect and impurity formation Energy

calculate a formation energy is from the total energy difference of supercells of the bulk material and one containing a defect. A number of correction factors are to be applied to the result and are discussed in this chapter. The mathematical expression of the formation energy of a defect is given by

$$E^f(X^q) = E_{Tot}(X^q) - E_{Tot}(Bulk) - \sum_i n_i \mu_i + q(E_F + E_V + \Delta V) \quad (4.1)$$

where X^q denotes a vacancy X with charge state q , n_i is the number of types i added to ($n_i > 0$) or removed from ($n_i < 0$) the supercell. $E_{Tot}(Bulk)$ and $E_{Tot}(X^q)$ are total energies from supercell calculations for the bulk crystal cell and the same cell with defect X , respectively. E_F and E_V are the fermi and valence band maximum levels. μ_i are the chemical potentials of the corresponding types and ΔV is a correction due to a charged supercell [118]. The chemical potential of each species can be estimated from the total energy calculation in its native state. In the case of ZnO, under typical growth conditions, we assume that the chemical potential of Zn at the ZnO growth interface is equal to that of Zn in the solid metallic state and can be approximated to the total energy of a Zn atom in metallic Zn. The chemical potential for O relative to the standard chemical potential of O, μ_O^\ominus , in the oxygen molecule can be calculated by adding the free energy of dilution to μ_O^\ominus ,

$$\mu_O = \mu_O^\ominus + \frac{\partial G}{\partial n_i} = \mu_O^\ominus + kT \ln \frac{P}{P^\ominus} \quad (4.2)$$

From general thermodynamic principles $\Delta G = \Delta H - T\Delta S$ and $H = U + PV$. P is the oxygen partial pressure during growth. Under typical oxide thin film growth conditions, the oxygen pressure in the growth chamber is in the range 10^{-2} to 10^{-1} mBar [17]. Thus at a typical film surface temperature of 500°C , the oxygen atom chemical potential decreases 0.6 to 0.8 eV below that at standard temperature and pressure (STP). From the theoretical approach, the critical conditions assumed for bulk ZnO to be bound together and be stable are given by,

$$\mu_O[O_2] < \mu_O < \mu_O[O_2] + \Delta H_f(ZnO) \quad (4.3)$$

$$\mu_{Zn}[Zn_{metal}] < \mu_{Zn} < \mu_{Zn}[Zn_{metal}] + \Delta H_f(ZnO) \quad (4.4)$$

The chemical potentials can thus be estimated from the expressions below.

$$\mu_{\text{O}} = \frac{1}{2}E_{\text{tot}}(\text{O}_2) + \Delta H_f(\text{ZnO}), \quad (4.5)$$

$$\mu_{\text{Zn}} = E_{\text{tot}}(\text{Zn}) + \Delta H_f(\text{ZnO}) \quad (4.6)$$

The O_2 molecule is in its spin triplet ground state and Zn in a bulk metallic state with the HCP crystal structure. The enthalpy of formation $\Delta H_f(\text{ZnO})$ for bulk ZnO is estimated from the expression,

$$\Delta H_f(\text{ZnO}) = E_{\text{tot}}(\text{ZnO})_{\text{Bulk}} - \left[\frac{1}{2}E_{\text{tot}}(\text{O}_2) + E_{\text{tot}}(\text{Zn}) \right] \quad (4.7)$$

This is basically the energy that binds bulk ZnO. This energy needs to be included in the chemical potential of a particular ion in bulk when the material is grown in an atmosphere where that particular ion species is less abundant than the others. In this context we assume thin films prepared in an oxygen-poor atmosphere, so Eqn. 4.5 is essential but in Eqn. 4.6 the enthalpy is not needed to be added with the total energy of Zn in its bulk metallic state to obtain the chemical potential. With two different exchange-correlation functionals used (LDA and B3LYP) and a number of specific basis sets, the enthalpy value for ZnO is estimated between -3.6 eV (B3LYP) and -4.1 eV (LDA), compared to an experimental value of -3.5 eV [154].

Calculations done using supercell methods and containing a charged defect always include unwanted contributions from images of charges created from the periodic boundary condition. Charged supercell calculations also introduce a compensating uniform background charge [155] that interacts and contributes further to the total energy. The necessary correction required to nullify any unwanted contribution is discussed later in this chapter.

4.2 Defect transition levels

The defect transition level is the position of fermi level at which the formation energies of a defect in its two different charge states become equal. It represents a measurement of the energy cost of changing the defect occupation from one charge

state to another. In standard notation transition energy between two charge configuration of a level is denoted by $\epsilon(q'/q)$ where q and q' are two different charge states of the defect. For a single-band the charge configurations are +2, +1, 0, -1, -2 depending on the electrostatic environment of a particular defect. Transition levels are obtained by comparing formation energies of a defect in two distinct charge states and solving for the fermi-level position at which they become equal. From Eqn. 4.1, the difference in total energy when a supercell containing a defect X changes its charge state from q to q' , is given by,

$$E^f(X^q) - E^f(X^{q'}) = E(X^q) - E(X^{q'}) + (q - q')(E_F - E_V) \quad (4.8)$$

where, the total energies of two charged states q and q' of a system with a defect X are given by $E(X^q)$ and $E(X^{q'})$ respectively. When the fermi level is at the defect transition level, the LHS of Eqn. 4.8 becomes zero. Hence the transition level $\epsilon(q'/q)$ can be defined by,

$$\epsilon(q'/q) = E_v + \frac{E(X^q) - E(X^{q'})}{q' - q} \quad (4.9)$$

Defect transition levels are estimated from both the total energies and from the one-particle eigenvalues of differently charged defect systems. Both methods are discussed in the following sections.

4.2.1 Transition level calculation using total energy

In the total energy method, total energies are calculated using DFT in supercell method and the difference between the total energies of two distinct charge states of a level replaces the term $E(X^q) - E(X^{q'})$ in Eqn. 4.9. Here the absolute value of the associated valence-band maximum (VBM) E_V is unknown, so the reference level is set to the VBM by subtracting the total energy difference of same two distinct charge states in bulk supercell of same size. The working formula to calculate transition levels from total energies is given by,

$$\epsilon(q'/q) = ([E_{tot}(X^q) - E_{tot}(X^{q'})] - [E_{Bulk}^q - E_{Bulk}^{q'}]) / (q' - q) \quad (4.10)$$

where $E_{tot}(X^q)$ is the total energy of the supercell with defect X with charge state q and E_{Bulk}^q is the same bulk supercell with same charge state. Eqn. 4.10 is associated with a donor-type defect where the neutral state is doubly occupied and the vacancy is getting positively charged. The oxygen vacancy (V_O) is such a defect. In Eqn. 4.10, the transition level is calculated from the change in energy when a hole is created in a bulk crystal supercell and transferred to a similar supercell with a defect. This is a two-step procedure explained schematically in Fig. 4.1. The energy cost for the first step is associated with the last two terms ($E_{Bulk}^q - E_{Bulk}^{q'}$) in Eqn. 4.10, where an electron is removed from the bulk valence band. In the second step, the electron is moved to bulk VBM from the defect state and associated energy cost represents the first two terms ($E_{tot}(X^q) - E_{tot}(X^{q'})$). The latter sum of terms is the fermi-level position with respect to the VBM at which the defect changes charge state and is represented by $\epsilon(q'/q)$ in Eqn. 4.10.

In the case of an acceptor-type defect, the defect state is charged by an electron and the charge state q' is generally -1 or -2. The last two terms in Eqn. 4.10 are total energies of bulk systems with 0, 1 or 2 electrons in the conduction band. Thus subtracting their energy difference from the total energy difference of defect systems yields the transition level with respect to the conduction band minimum (CBM). In order to obtain the value of the transition level with respect to the VBM, the value of energy gap should be added to the expression, which is,

$$\epsilon(q'/q) = ([E_{tot}(X^q) - E_{tot}(X^{q'})] - [E_{Bulk}^q - E_{Bulk}^{q'}]) / (q' - q) + E_g \quad (4.11)$$

Where E_g is the energy gap, which also was calculated using the total-energy method as the difference of the ionization potential and electron affinity. Both are given by

$$\text{Ionisation potential (IP)} = E_{Bulk}^+ - E_{Bulk}^0 \quad (4.12)$$

$$\text{Electron affinity (EA)} = E_{Bulk}^0 - E_{Bulk}^- \quad (4.13)$$

$$E_g = IP - EA \quad (4.14)$$

The physical meaning of Eqn. 4.12 - 4.14 is that the band gap is estimated from the difference of energy costs to add or remove an electron to the system. The

additional electron occupies the lowest unoccupied level (CBM) of the host system while an electron that is being removed is from the highest occupied level (VBM). This does not imply that the band gap is associated with the ground state only. The band gap can theoretically be obtained from any other state (say VBM-1/CBM+1) by removing/adding two or more electrons but the computational error increases for reasons: **1.** Descriptions of excited state from DFT calculations is not accurate. **2.** Computational error may increase because it is difficult to converge wavefunctions for the metallic states which occur when one or more electrons are removed from the valence band or added to the conduction band. **3.** Periodic boundary conditions render image charges for charged systems and interaction of image charges contribute to the total energy. Hence the band gap calculated using this method has to be calculated using a large supercell or necessary corrections (*e.g.* by plotting the band gap with respect to inverse of supercell volume and extrapolating for infinitely large supercell) must be applied. The correction schemes are described later in this chapter.

The physical interpretation of Eqn. 4.10 and Eqn. 4.11 is explained using schematic diagram in Fig. 4.1. The difference in the estimation of transition levels between a negatively charged defect and a positively charged one is that in a negatively charged defect an electron is inserted into the empty CBM of the bulk in the first step. In the second step it is shifted to the defect state. This picture differs from the last one by the fact that in the second step the electron is transferred from the CBM to the defect state, (not the VBM) and thus the associated energy cost will be with respect to the CBM only. So if we apply Eqn. 4.10 in this case we will get the transition levels with respect to the CBM. This problem is solved by simply adding the energy-band gap value E_g which gives us the current form of Eqn. 4.11

4.2.2 Transition level from single-particle eigenvalues

Another approach to estimate the transition levels is using Janak's theorem [156] to obtain the energy difference term $E(X^q) - E(X^{q'})$ in Eqn. 4.9 from the single-particle eigenvalues of charged defect states. Janak has shown that single-particle

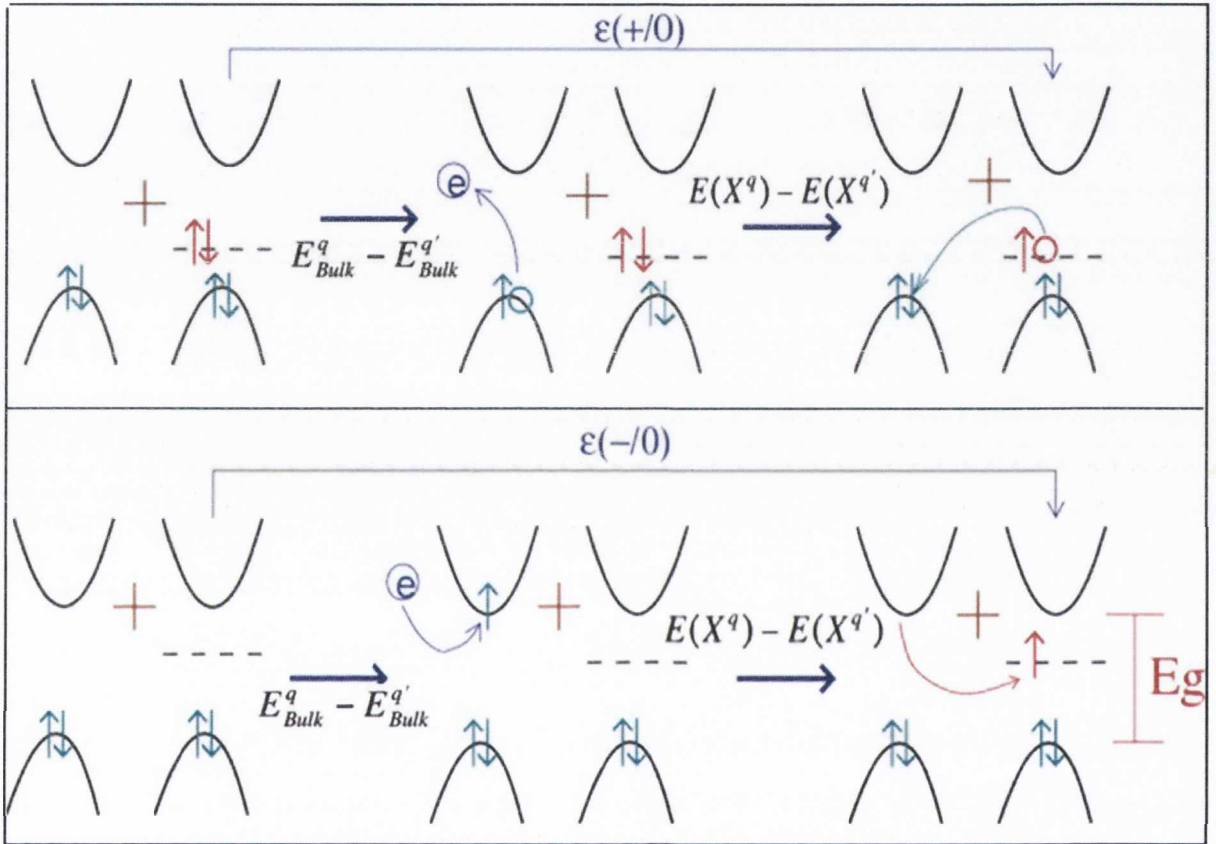


Figure 4.1: Schematic diagram explaining working formulae for transition level calculation. Top: hole-charged defect. The transition level $\epsilon(+/0)$ has been explained as the example. Bottom: estimation of transition level $\epsilon(-/0)$

eigenvalues can be obtained by taking the derivative of the DFT total energy with respect to the occupation number associated with that particular eigenvalue,

$$\frac{\partial E}{\partial n_i} = \epsilon_i \quad (4.15)$$

This identity is Janak's theorem and relates the eigenvalue of a state with the total energy of the whole system when the state is being occupied by an infinitesimally small charge. From this identity, the change in the ground state total energy E upon electron occupation of the lowest unoccupied molecular orbital (LUMO) (in other words the CBM) can be obtained. The change in the total energy upon charge occupation is what is needed for the calculation of transition levels and therefore can be estimated from the eigenvalues of the charging state. This is done by solving Eqn. 4.15 in the limit between the two states involved in the transition. In the case of populating a defect level, the total energy change can be derived by,

$$E(X^{q'}) - E(X^q) = \int_0^1 e_{h+1}(N+n)dn \quad (4.16)$$

where $e_{h+1}(N)$ is the eigenvalue of the lowest unoccupied state for the q -charge state defect and n is the number of electrons added. Eqn. 4.16 is simplified by taking just the two eigenvalues involved in the transition instead of integrating over all eigenvalues for fractional charge accumulation. Hence the numerical approximation is given by,

$$E(X^{q'}) - E(X^q) \approx \frac{e_{h+1}(N) + e_{h+1}(N+1)}{2} \quad (4.17)$$

The total energy differences associated with vertical transitions are estimated from the eigenvalue-shift at the Γ -point in the single particle band-structure calculation. It is shown in Chapter 6 that the transition energies calculated from both methods roughly agree with each other and with the values calculated by several other groups. Gallino *et al* [71] have shown that this approximation gives accurate results for transition levels in agreement with other published data. The

4.3 Computational errors and correction schemes

estimation of transition levels would be more accurate and appropriate if instead of obtaining the eigenvalue at the Γ -point only, it is averaged over all the k-points by integrating it over the k-point along the designated k-path. But this requires diagonalisation of the energy eigenvalues for a set of k-points sampled all over the Brillouin zone, which is computationally much more expensive than just diagonalizing only at the Γ -point. It is important that the k-point convergence of energy in the SCF calculation is achieved by sampling enough number of k-points. There is no variational principle governing the convergence with respect to the k-point mesh. This means that the total energy does not necessarily show a monotonic behavior and is oscillatory with increasing k-points. However in this case the total energy convergence is achieved to 10^{-7} Hartree for the SCF calculation and the eigenvalues are computed from the converged density matrix. The computation-time for calculating the eigenvalues for a number of k-points can be reduced by making the assumption that the dispersion shape is not changed much upon charging the system. Thus if the eigenvalue of only the Γ -point for the two bands responsible for transition (Eqn. 4.17) is considered, the error in the result may be too low to be considered. We will discuss this assumption on the basis of the results in Chapter 6.

4.3 Computational errors and correction schemes

There are a number of factors to be taken into consideration when computing formation energies and transition levels. The effect of periodic boundary condition was mentioned before. Apart from that, the effect of k-point sampling and basis sets are discussed here. Nieminen [21] has pointed out a few issues with first-principles calculations of defects that are also discussed here.

4.3.1 Effect of periodic boundary condition

In the case of a charged vacancy, the total energy of a periodic system with a charged defect includes contributions from interactions between the defect charge, and its images in neighboring unit cells generated from periodic boundary condition (PBC). In the computation algorithm of a charged system, a jellium back-

4.3 Computational errors and correction schemes

ground charge (uniform electron-gas-like charge) of opposite sign is inserted in order to keep charge neutrality. This background charge also interacts with its periodic images and contributes to the total energy, thus affecting the formation energies and transition levels. Using large supercells is one easy but expensive solution to this problem but this does not completely nullify the energy contribution due to PBC. The Makov-Payne correction scheme [155] provides an expansion for the finite-size corrections that relates the energy contribution due to PBC for a cubic supercell of size L to the isolated-defect limit ($L \rightarrow \infty$) as,

$$\Delta E = \frac{q^2 \alpha}{2\epsilon L} + \frac{2\pi q Q}{3\epsilon L^3} + O(L^{-5}) \quad (4.18)$$

where α is the Madelung constant, ϵ is the relative permittivity for the host bulk material, q is the net charge and Q is the quadrupole moment of the charge distribution. ϵ and Q are properties of the periodic density and the aperiodic density, respectively. Clearly, for larger values of L , ΔE will be smaller but for larger L the total energy calculation will be expensive. Maximum value of ΔE in the current work was found around 1-2 eV for the minimum of supercell size. Typically $\Delta E < 1\text{eV}$ is observed for the supercell sizes used here. Lany *et al* [70] used an approximation $L = V^{1/3}$ where V is the volume of the supercell but this may not be applicable for non-cubic supercells as the interaction between image charges is anisotropic for non-cubic supercells.

In this work supercells of size $L \times L \times L$ are used with $L = 2, 3$ and 4 containing 32, 108 and 256 atoms, respectively. There is scope for computational errors at both of the ends of supercell size. For a relatively small supercell the defect and its periodic images are much closer and experience higher interactions. Also in a small supercell the defect does not have much space to relax. In a very large supercell these problems are minimal but there are other problems such as large computational time and relatively lower k-point density for the DFT calculation. Hence we have to choose a supercell of medium size, optimizing for a low ΔE and moderately low computation time with a dense k-point mesh, such that the total energy converges. In this work, for ZnO, $L=3$ ($3 \times 3 \times 3$) supercell is used for most of the defect energetics calculations. This supercell is large enough to host multiple defects, has a ΔE of ~ 0.4 eV for the band gap. Although 0.4

4.3 Computational errors and correction schemes

eV is quite large in comparison to the band gap of 3.4 eV, the $3 \times 3 \times 3$ is the best supercell we can use in comparison to $2 \times 2 \times 2$ ($L=2$) and $4 \times 4 \times 4$ ($L=4$).

The parameters in Eqn. 4.18 can be determined by fitting the total energy difference between bulk and defect supercell ($E_X^q - E_{Bulk}^q$) against $1/L$ or $1/L^3$ but given that only three supercells are available the $1/L^3$ fitting is not possible with only three points on the graph. The formation energies and transition levels can be plotted against $1/L$ and fitted to a straight line. Extrapolation of that straight line to $1/L=0$, i.e. for infinitely large supercell size ($L=\infty$) ought to yield the corrected values. Correction of the band gap of ZnO estimated using Eqn. 4.14 is shown in Fig. 4.2. Fig. 4.2 shows linear extrapolation of band gap values calculated for different supercell sizes using LDA implemented on the Quantum Espresso code [150]. The corrected value of the band gap was found to be 0.11 eV, which is much smaller than the experimental value but in agreement with values estimated by other groups using LDA [64, 157]. The values shown in Fig. 4.2 is not used anywhere as results in this work. The purpose of this calculation is to show the usability of the Makov-Payne correction in a similar scenario.

There are a few other correction schemes developed, based on the Makov-Payne expansion. Hine *et al* [158] proposed that changing the shape of the supercell in addition to its size gives additional accuracy in the extrapolation. Changing the shape changes the Madelung constant α and can be negative also. The total energy can be plotted against $1/L$ and becomes a function of both L and α . Thus one can have data either side of $1/L=0$ for the supercells with $\alpha < 0$ [21]. In another recent study Freysoldt *et al* [72] suggested that for most of the defects Eqn. 4.18 requires large supercells, and since the significance of the higher order terms is unclear, the long-range tail of the bare Coulomb potential can be truncated to neglect the polarization beyond supercell lengths. Freysoldt *et al* suggested that the first order correction term in Eqn. 4.18 is given by

$$\Delta E^1 = \left(\frac{\pi}{6}\right)^{1/3} (1 - \epsilon^{-1}) \frac{q^2}{L} \quad (4.19)$$

This approach was tested in charged vacancies in diamond and GaAs [72].

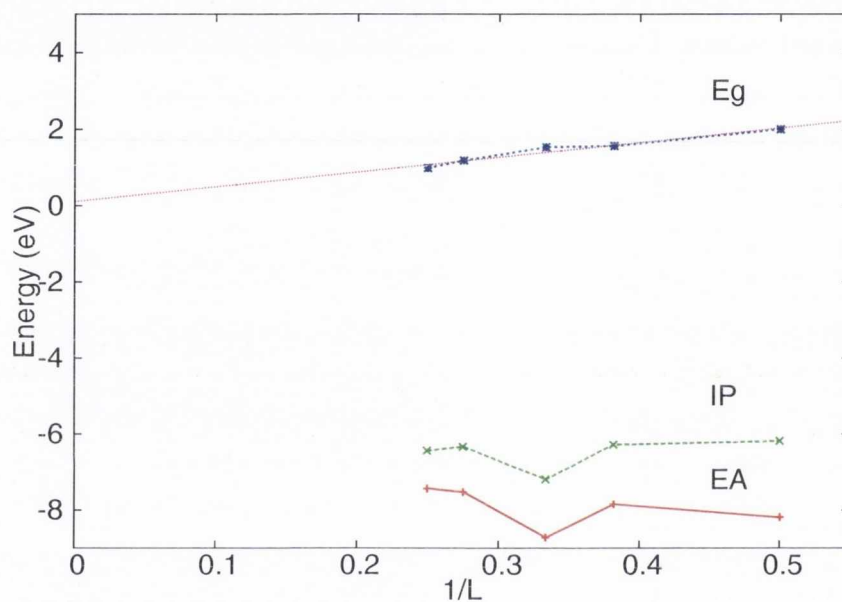


Figure 4.2: Band gap of ZnO estimated using Eqn. 4.14. $L = V^{1/3}$. Calculations are made using LDA exchange implemented on the Quantum Espresso code. The value of band gap E_g extrapolates linearly to 0.11 eV for infinitely large supercell. This value of E_g is too low in comparison to experiment but is comparable to other LDA results (see text) that always underestimates the band gap.

4.3.2 Effect of relaxation

Optimizing the geometry of the crystal by relaxing all degrees of freedom is an essential step to get the right formation energy and transition levels of defects. A full relaxation involves relaxation of lattice parameters and atomic positions. When a vacancy defect is created, depending on its charge state and electrostatic environment (donor/acceptor) it will exert a force on its surroundings until the lattice comes to equilibrium. The necessary relaxation energy is equal to the thermal energy associated with the process. The computational algorithm for geometry optimization is done by minimising the total energy with respect to optimal atomic positions. An initial guess of a model Hessian matrix [159] is assumed for the first relaxation step where the lattice parameters and bond-lengths are relaxed to a maximum of 10-15%. Pulay force [160] components on the crystal lattice are then calculated using the recent implementation of Hartree-Fock energy gradient [161] using a conjugate gradient algorithm proposed by Schlegel [159]. The atomic coordinates are replaced according to the forces. The density is calculated using DFT SCF calculation for each new set of atomic positions and the total energy is minimized. This process is repeated in an iterative way until the atomic displacements as well as the gradient of displacements minimizes below a certain level of tolerance, in the current work 10^{-4} Å.

In this work it has been shown that relaxation of the crystal lattice has a huge impact on the formation energies and transition levels of the defect states. This is because the Coulomb interaction between defect and surroundings depends on different charge state of the defect.

4.3.3 Effect of k-point sampling and basis sets

Different k-point sampling also influences the defect-defect interactions within the supercell. The convergence of different charge states varies with varying supercell size if the k-point sampling is not accurate [55]. Thus it affects the ionization levels most. It is of utmost importance that all the computation involved in a calculation of a single formation energy or transition level should have the same k-point mesh. When the supercell size changes, the k-point density changes accordingly. Therefore, if we intend to compare results from different-sized supercell

4.3 Computational errors and correction schemes

calculations, the k-point density should be same. This means we have to use more k-points in smaller real-space supercells and less k-points in large supercells. Note that a large supercell calculation with a dense k-point mesh can be extremely expensive. On the other hand, for the smaller supercells a dense k-point mesh is necessary to obtain the ground-state correctly. Especially for conducting systems, the localized-orbital-basis code CRYSTAL cannot determine the fermi-level at all if the k-point sampling is not dense enough. This makes the larger supercell calculation in conducting states difficult regarding choice of k-point sampling. For such cases the density of k-point mesh needed for the numerical integration for calculation of the fermi surface correctly must be higher than that which is needed for SCF diagonalisation. In this work a k-point mesh was used for the metallic systems denser by a factor of 2^3 than that is used in semiconducting systems. Details are given in Appendix A.

A number of basis sets was used in this work. Basis sets provide the initial guess for the Kohn-Sham orbitals. We have discussed the pros and cons of different basis sets in Chapter 3. In this work, the basis sets were chosen on the basis of convergence and minimum total energy.

When a vacancy defect was created, an empty basis set, otherwise known as a ghost atom [147], was placed in the vacancy site to ensure continuity in the real-space density. If one or more electrons are trapped in this vacancy, this initial guess improves convergence of the calculation. The prefactors and exponents of the Gaussian basis sets were tuned to obtain the lowest total energy for a constant crystal structure. Details of the basis sets used are given in Appendix B.

Chapter 5

Intrinsic Vacancy Defects and Impurities in ZnO: Electronic and Crystal Structure

In this chapter we discuss the electronic structures of intrinsic vacancy defects in ZnO. Intrinsic defects such as vacancies and interstitials are generally created in thin films by growth off-stoichiometry. There are a number of ways to manipulate a particular type of defect. Anion (oxygen in this case) vacancy concentration is directly related to the oxygen partial pressure of the growth chamber [17, 44]. Cation vacancies can be controlled in techniques such as molecular beam epitaxy (MBE) [11]. We have discussed the experimental techniques used to characterise the crystal and electronic structure of a defect in Chapter 2. Electron paramagnetic resonance (EPR) [50] and positron annihilation spectroscopy (PAS) [53] techniques can be used to probe the existence of electron trapping defects in ZnO. Yet it is not straightforward to assign a particular defect to a particular experimental observation and supporting evidence from first-principles calculations is required.

Intrinsic vacancy defects are chosen as the starting point of this work as they are related to interesting experimental observations described in Chapter 2 and are relatively abundant in samples [44, 62, 87]. A search is carried out for large - U electron trapping defects which may shed some light on the long-range interaction

between defects and the possibility that paramagnetic defects prefer a parallel-spin alignment. The Hubbard model described in Chapter 2 is applied and an attempt is made to explain ferromagnetism in these oxides [15, 18] in terms of defect interactions.

As discussed in the introductory chapter, the oxygen vacancy defect (V_O) is a negative U defect [36, 64] but is investigated in this work as it is probably the most abundant defect for films grown in low oxygen partial pressure [17, 43].

Other intrinsic vacancy defects are taken into consideration. The zinc vacancy (V_{Zn}) has been investigated in this work as a possible large- U electron trap. The zinc interstitial (Zn_i) has a high formation energy and under O-poor growth conditions has a low abundance [62]. Also Zn_i is not an electron trap [36]. The possible existence of complex cluster vacancies is also discussed. There is one positron annihilation spectroscopy (PAS) study by Zubiaga *et al* [53] where the presence of negatively charged ZnO pair vacancies was considered. Complex defects such as the ZnO pair vacancy (V_{ZnO}) and the ZnO_3 cluster vacancy (V_{ZnO_3}) have been investigated as possible candidates for large- U defects in this work.

Calculations done in this work suggest that pair vacancy and cluster vacancies are possible in these oxides and energetically more favourable than separate defects. When defects are created in an oxide due to off-stoichiometry during growth, they are mobile at high growth temperature [162] and, if energetically favourable, they can bind together to form cluster vacancies or congregate on the surface. Total energy calculations are made to determine the stability of complex defects V_{ZnO_n} for $n=1-3$. These calculations reveal that the total energy of a supercell with one negatively charged V_{ZnO}^- is lower by 1.9 eV than two separate V_O^0 and V_{Zn}^- vacancies. Considering the frequent observation that V_O are more abundant than V_{Zn} [62], if we continue to add more V_O to the neutral pair vacancy defect, V_{ZnO} , total energy calculations predict that a V_{ZnO} and a V_O are bound by 1.4 eV to form V_{ZnO_2} . If one more V_O is added to V_{ZnO_2} to form V_{ZnO_3} , the binding energy is 1.2 eV. Vacancy defects are surrounded by dangling bonds and when multiple cation and anion vacancies are created close to each other, electrostatic attraction between the anion and cation dangling bonds cause point defects to congregate to form cluster vacancies [55].

In this chapter, electronic band-diagrams along with the respective crystal structure of ZnO are presented for the three intrinsic vacancy defects V_O , V_{Zn} and V_{ZnO} in every possible charge-state they can attain. The band-diagram represents the energy spectrum of a system and for a system with a defect it can show the new energy level that appears when a defect is created. The dispersion of this level represents the bandwidth of the defect-trapped state and the transition energies can be calculated from the level shift upon charging the defect. The details of the estimation method have been discussed in Chapter 4. A supercell method is used in all of the computations with different supercells for different purposes. The wurtzite unit cell of ZnO is shown in Fig. 5.1. All the supercells are derived from this unit cell. Details of the calculations and supercells are given in Appendix A. The CRYSTAL DFT simulation package is used, which uses linear

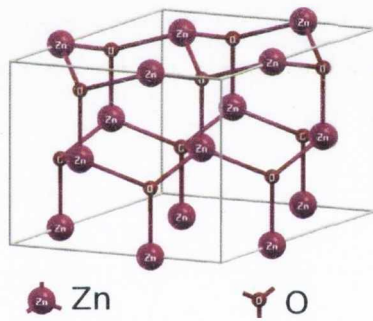


Figure 5.1: Wurtzite unit cell of ZnO.

combinations of Gaussian functions as localized orbital basis sets (See Chapter 3). The details of the basis sets used in this work are given in Appendix B. We will briefly discuss in this chapter the influence of basis sets on the electronic structure of a system.

Finally, the effects of Co and Al doping are discussed. Calculations on $Zn_{1-x}Co_xO$ ($x \sim 0.05$) supercells with or without vacancy defects are used to investigate anti-ferromagnetic Co-Co coupling in a ZnO host and coupling between defect-trapped electron and substituted Co^{2+} ions. Calculations on $Zn_{1-x}Al_xO$ ($x \sim 0.02$) supercells are used to investigate n-type doping of ZnO by aluminum.

5.1 Electronic structure of the defects

Total energy calculations are carried out for the intrinsic vacancy defects V_O , V_{Zn} , V_{ZnO} and V_{ZnO_3} . The final charge density was obtained with the total energy difference between SCF cycles below the tolerance of 10^{-7} Hartree. The density matrix from this SCF calculations was also used to generate the energy-band diagram for the corresponding system. The band diagrams are plotted for both the relaxed and unrelaxed crystal structures for each defect.

5.1.1 Oxygen vacancy V_O

The oxygen vacancy is found to be the most abundant defect in thin film ZnO samples as well as in other oxides prepared in a controlled atmosphere [17, 43]. Each neutral oxygen vacancy leaves behind two dangling electrons in the system which are thought to be a source of n-type conductivity observed in O-poor ZnO [163, 164]. The electronic band diagram of ZnO with one oxygen vacancy is shown in Fig. 5.2.

The crystal structures of the oxygen vacancy in different charge states are optimized by relaxing the atomic positions around their ideal coordinates. The technique was explained in detail in Chapter 4. Changes in crystal structure on relaxation are different for each charge state. The change in crystal structure is quite localized and relatively large displacements occur around the vacancy only. The band structure and corresponding crystal structures around the vacancy are shown in Fig. 5.3.

The oxygen vacancy has been investigated by several groups, both by experiment [5, 17, 164] and first principles groups [45, 64, 70, 157], so the electronic structure and characteristics of this defect are quite well studied. Experiments done with ferromagnetic ZnO thin films suggest a correlation between oxygen vacancy concentration and ferromagnetic moment. Samples prepared under low oxygen partial pressure have higher concentrations of oxygen vacancies. Venkatesan *et al* [17] have shown that as the partial oxygen pressure of the sample preparation chamber was increased, the ferromagnetic moment of respective samples decreased. This study was done on Co doped ZnO. Similar observations were

5.1 Electronic structure of the defects

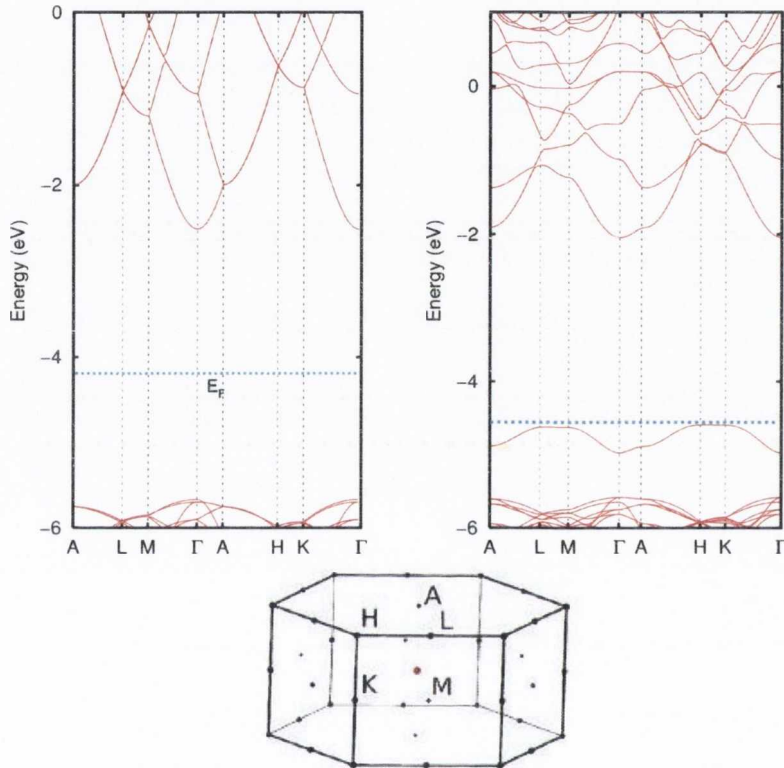


Figure 5.2: Band structures of bulk ZnO (left) and that of ZnO with a neutral oxygen vacancy (V_O) (right) in a wurtzite $3 \times 3 \times 3$ supercell. The wurtzite Brillouin zone and the k-path is shown at the bottom. Horizontal dotted lines show the Fermi level.

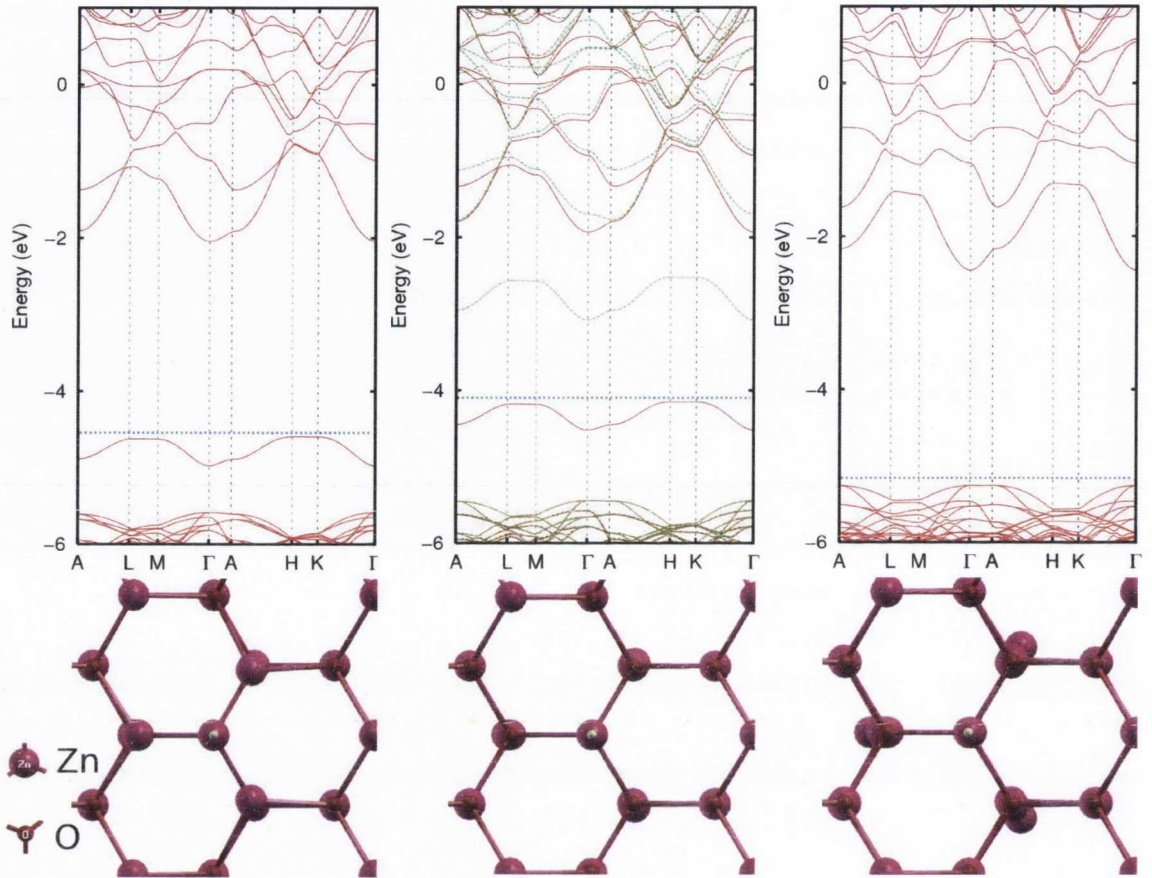


Figure 5.3: The bandstructures (top) and crystal structures (bottom) of V_O in different charge states for fully relaxed $3 \times 3 \times 3$ supercell. From left to right, V_O^0 , V_O^+ and V_O^{2+} respectively. For spin polarized systems, red lines show the majority spin and green/dashed lines show the minority spin states. Large pink spheres denote the Zn atoms and smaller red spheres denote oxygen atoms (Shown on bottom-left of figure). The small green dot denotes the vacancy site. Fermi levels are shown by horizontal blue dotted lines.

made in the case of undoped ZnO [18] and other oxides such as In_2O_3 or SnO_2 [18, 19].

However, V_O is found by several first-principles group to be a negative- U defect [36, 64], which we will confirm in the current work. Therefore in V_O , single electron occupancy is less favourable than a double or zero occupancy of the defect

level depending on electron concentration. We have discussed in Chapter 2 that the Hubbard model and theoretical models such as the impurity band exchange model [15] require a singly charged oxygen vacancy to be a magnetic centre in order to take part in magnetic interaction of these oxides. Since V_O is negative- U , and unable to act as a magnetic centre or a positive Hubbard- U F-centre, it may not take part in long - range defect-defect interaction and in ferromagnetism experimentally observed in oxygen-deficient ZnO thin films.

5.1.2 Zinc vacancy V_{Zn}

The Zn vacancy is rarer than the O vacancy in ZnO unless the sample is grown under high oxygen partial pressure [55]. We will see in the Chapter 6 that the formation energy of neutral V_{Zn} is $\sim 3-4$ eV greater than that of neutral V_O . Control of oxygen partial pressure in the deposition chamber for thin film preparation allows manipulation of oxygen vacancy population, but the concentration of cation vacancies cannot be manipulated so easily, except by a few techniques such as ion beam epitaxy [11]. The Zn vacancy (V_{Zn}) has a higher formation energy in ZnO but can be created during growth of thin films [62]. The electronic structure of V_{Zn} is described by the band structure diagram given in Fig. 5.5. Removing a Zn atom leaves two holes in the system and thus the vacancy can absorb up to two electrons. The ground state of the neutral Zn vacancy, V_{Zn}^0 , is a spin - 1 triplet state with two localised holes in it. The trapped electrons in V_{Zn}^- and V_{Zn}^{2-} are absorbed by dangling oxygen bonds and remain in O 2p-like orbitals. The wavefunction isosurface is shown in Fig. 5.4 for the defect energy band in its singly occupied (V_{Zn}^-) state. Trapping electrons in a localized p-orbital reduces the bandwidth of the defect band and the band appears with very small dispersion.

The relaxed crystal structure shows that the O atoms neighbouring the vacancy sites displace and move towards the vacancy site. The displacements of the O atoms are in the range of 0.2-0.5 Å. As depicted in Fig. 5.5, the displacement is largest in the neutral Zn vacancy V_{Zn}^0 . V_{Zn} can assume three charge states, V_{Zn}^0 , V_{Zn}^- and V_{Zn}^{2-} . The displacement gradually decreases as the vacancy is filled up

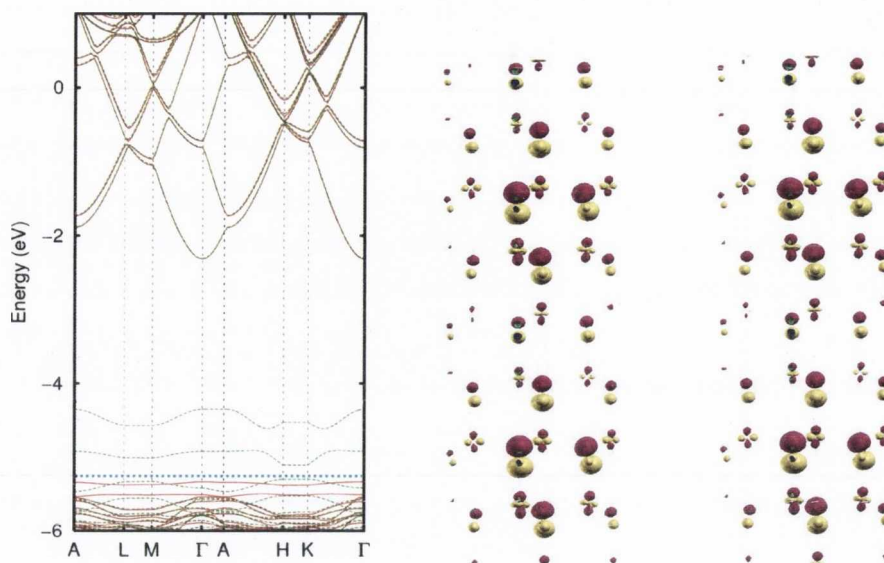


Figure 5.4: (Left) Band structure of V_{Zn}^- for both spins (red: majority, green:minority). (Right) The Γ -point wave function isosurface of V_{Zn}^- state immediately below the Fermi level (blue dotted line)

by electrons (Fig. 5.5). Calculations of transition levels between different charge states and U -value are shown in the Chapter 6.

5.1.3 ZnO pair vacancy V_{ZnO}

An anion-cation pair vacancy such as the ZnO pair vacancy can be formed in thin films during growth when the vacancies are mobile at high temperature. We have stated that the probability of a V_{ZnO} vacancy being created is larger than separate V_O and V_{Zn} vacancies. The existence of V_{ZnO} was also postulated in a positron annihilation spectroscopy experiment by Zubiaga *et al* [91]. There are two possible configurations of this defect due to the wurtzite structure. The first is where one Zn atom and its nearest neighbour O atom along the axial c direction are vacated together (V_{ZnO}^{Axial}). The second configuration is a V_{ZnO} vacancy where one Zn atom and its one of its three neighbouring O atoms in the direction parallel to the radial ab plane is vacated (V_{ZnO}^{Radial}). These two configurations are depicted in Fig. 5.6.

5.1 Electronic structure of the defects

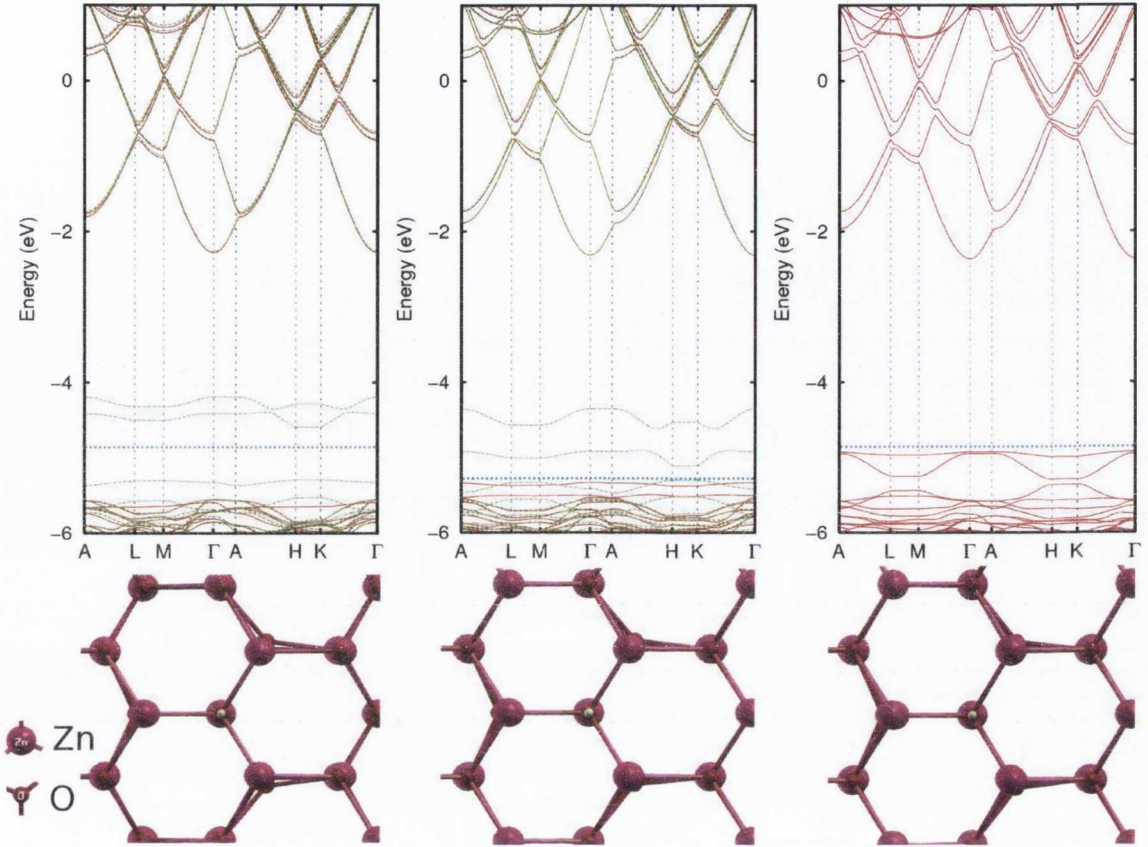


Figure 5.5: The bandstructures (top) and crystal structures (bottom) of V_{Zn} . From left to right, V_{Zn}^0 , V_{Zn}^- and V_{Zn}^{2-} respectively, fully relaxed $3 \times 3 \times 3$ supercell. For the spin polarized systems majority and minority band diagrams are plotted in the same figure. Note that the ground state of V_{Zn}^0 is a spin-triplet with two holes. The color scheme is the same as Fig. 5.3.

V_{ZnO}^{Axial} is energetically favoured over V_{ZnO}^{Radial} by a large energy (1.1 eV), hence V_{ZnO}^{Axial} is assumed to be much more abundant and has been used in all calculations discussed further. We will use the term V_{ZnO} instead of writing V_{ZnO}^{Axial} for simplicity. Majority and minority spin band structures of V_{ZnO} are shown in Fig. 5.7 and Fig. 5.8. The moderately large dispersion of the defect electron state over the Brillouin zone indicates that the wavefunctions of the defects in neighbouring cells overlap.

The bandstructures of V_{ZnO} for the different charge states are shown in Fig.

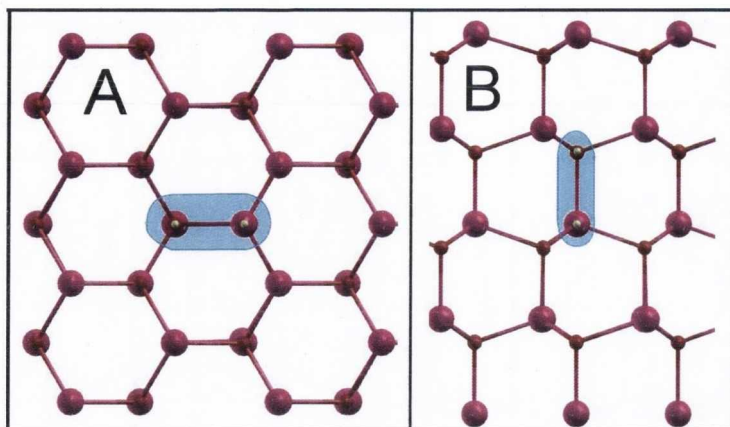


Figure 5.6: The two different possible configurations of V_{ZnO} , A: Radial and B: Axial.

5.7 and Fig. 5.8 for the relaxed geometries. The deformations of crystal structure due to relaxation are also shown for each charge state. As the aim of this work is to search for large- U defects that may take part in the ferromagnetism observed in these oxides, the singly charged defect state, here the V_{ZnO}^- state, is important. Hence this particular defect state demands more focus. Note that V_{ZnO} is a neutral defect with no dangling charge and therefore it can host the whole range of charges -2, -1, 0, +1 and +2. So there are these five possible charge states for V_{ZnO} , although positively charged V_{ZnO} would be rare in naturally occurring oxygen-poor n-type ZnO films and will entirely depend on a low Fermi level. Nonetheless, these states are considered here for completeness. The electronic band structures and the changes in crystal structure upon hole-doping in V_{ZnO} are displayed in Fig. 5.8. The dispersion of the V_{ZnO} defect band in its +1 and +2 states are similar to its -1 and -2 states but are shifted in energy. The energy associated with spin-degeneracy in hole-doped V_{ZnO} is much less than its electron-doped counterpart. We will see in the next chapter in the calculation of formation energies that these states are more stable than the singly charged states for respective Fermi levels.

The V_{ZnO}^+ vacancy is similar to V_{Zn}^- with respect to both crystal and electronic structure. The flat non-dispersive state in the band diagram of V_{ZnO}^+ originates from the dangling O-2p orbitals in a similar fashion as in V_{Zn}^- . V_{ZnO}^{2+} has a

5.1 Electronic structure of the defects

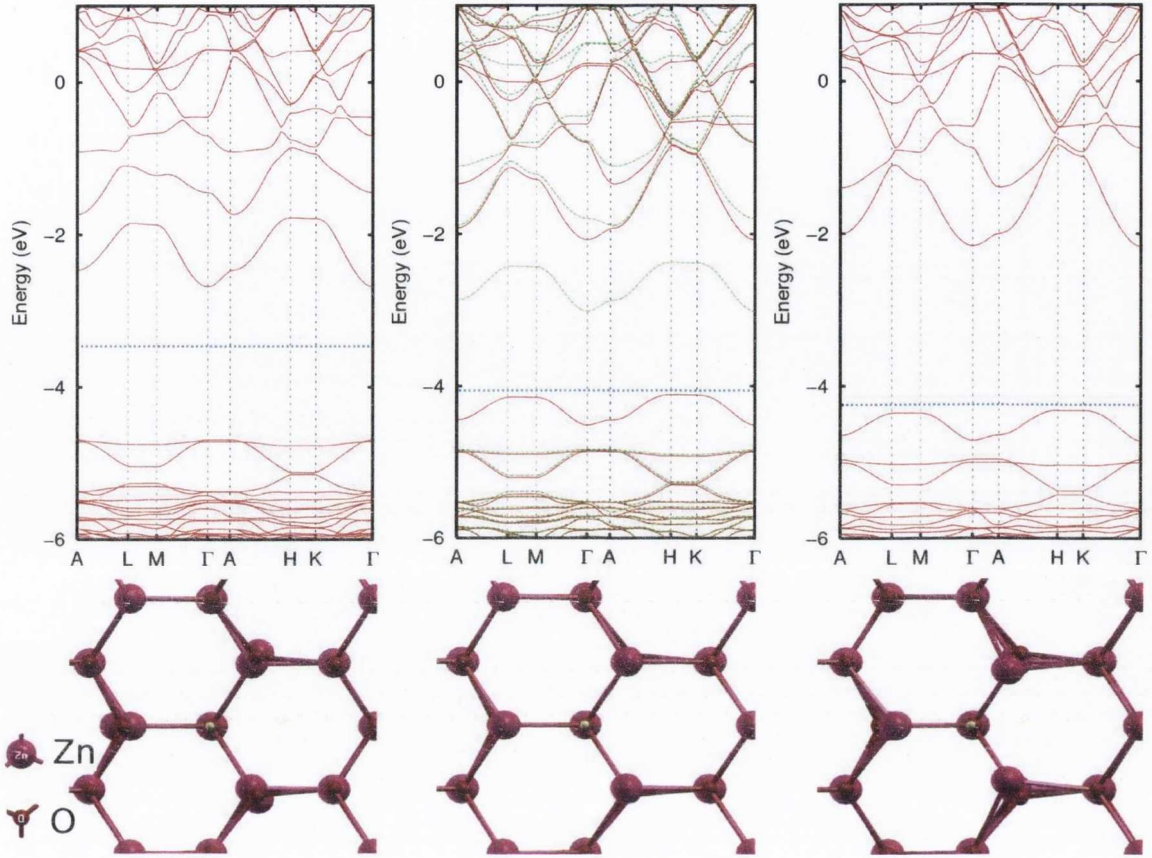


Figure 5.7: The bandstructures (top) and crystal structures (bottom) of V_{ZnO} for a fully relaxed $3 \times 3 \times 3$ supercell. From left to right, V_{ZnO}^0 , V_{ZnO}^- and V_{ZnO}^{2-} respectively. For spin polarized systems, red lines show the majority spin and green/dashed lines show the minority spin states. The color scheme is the same as Fig. 5.3 and Fig. 5.5

triplet ground state and is again similar to V_{Zn}^0 (Compare in Fig. 5.13, the major difference between V_{Zn} and V_{ZnO} is the M-shaped defect band characteristic of V_O).

The change of structure upon lattice relaxation around the V_{ZnO}^- is shown in Fig. 5.9. It can be seen that the Zn - Zn distances between Zn ions neighbouring the defect are reduced and a Zn_3 trimer is formed. The change in the overall structure away from the defect is small. The defect electrons partially fill 4s states of three Zn ions neighbouring to the defect, pulling them into the Zn_3

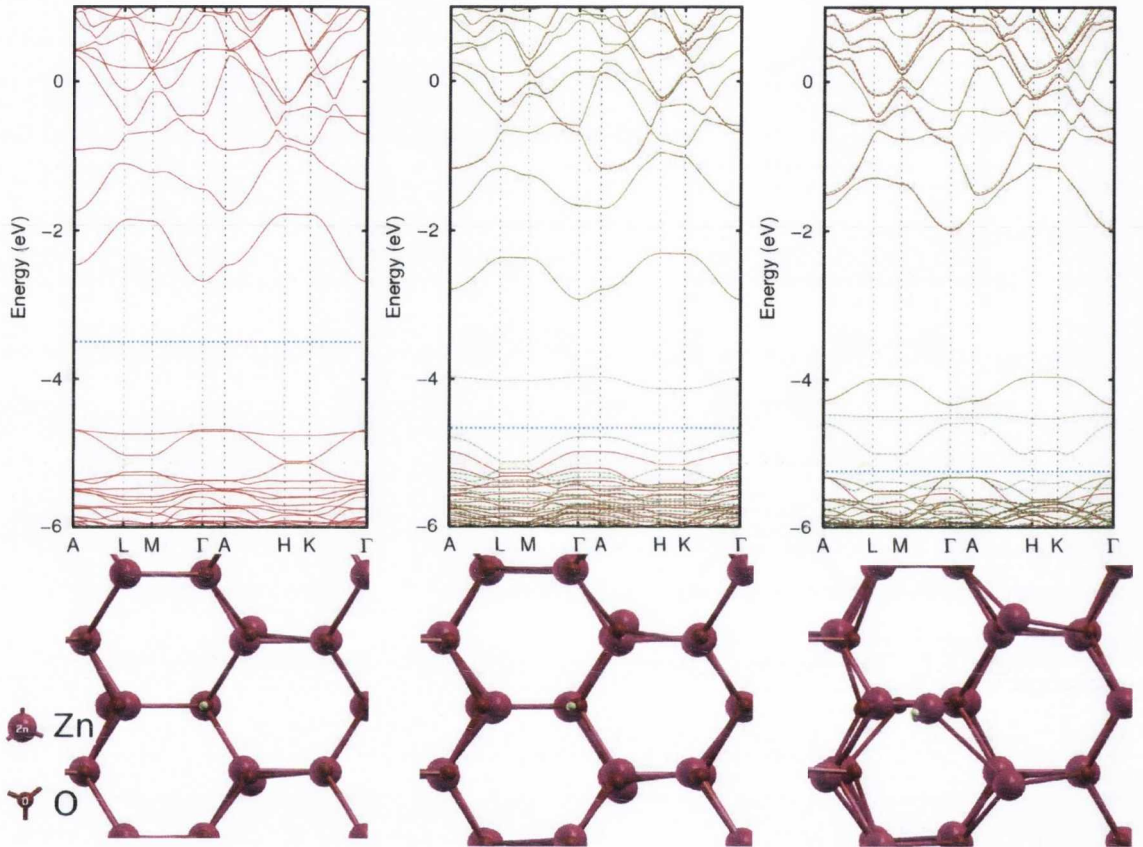


Figure 5.8: The bandstructures (top) and crystal structures (bottom) of V_{ZnO} for a fully relaxed $3 \times 3 \times 3$ supercell. From left to right, V_{ZnO}^0 , V_{ZnO}^+ and V_{ZnO}^{2+} respectively. The color scheme is the same as Fig. 5.7.

5.1 Electronic structure of the defects

trimer. The Zn-Zn distance shrinks from 3.25 Å to 2.62 Å and resembles closely that of metallic Zn (2.66 Å).

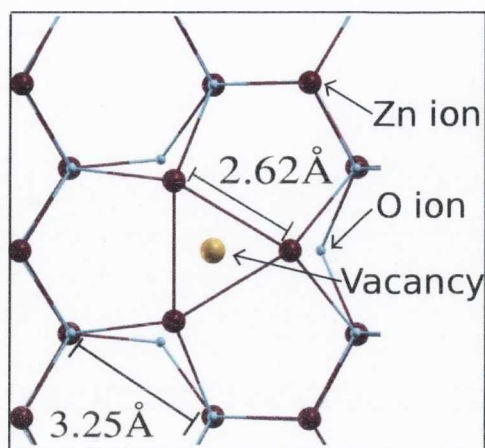


Figure 5.9: Change in crystal structure upon relaxation of lattice around V_{ZnO}^-

The cylindrical-shaped pair vacancy is stretched along its axis (c axis) when relaxed and the charge resides on the V_O end, localized in an s -like orbital on the Zn_3 colloid (Fig. 5.9). This s -like wave wavefunction can be seen in Fig. 5.10 where the wavefunction isosurface of the defect level at Γ point is plotted.

The defect possesses a total magnetic moment of $1 \mu_B$ associated with the localized electron cloud seen in Fig. 5.10. In a partially filled system, more than half filling this trapped electrons in V_{ZnO} can interact at ranges exceeding 11 Å when there are between one and two electrons per vacancy. In a large supercell with three electrons and two V_{ZnO} defects 11 Å apart, the electrons are partially trapped and they assume a spin parallel ground state. A large defect bandwidth of ~ 0.4 eV allows electrons trapped in this defect to interact at long range. Detail of defect-defect interaction of V_{ZnO} vacancy is discussed in Chapter 7. The trapped spin can also couple with a transition metal ion in its vicinity. The band diagram of Co-doped ZnO is shown in Fig. 5.14. The defect-defect and defect - Co exchange interactions are described in Chapter 7 and the exchange coupling constants are calculated.

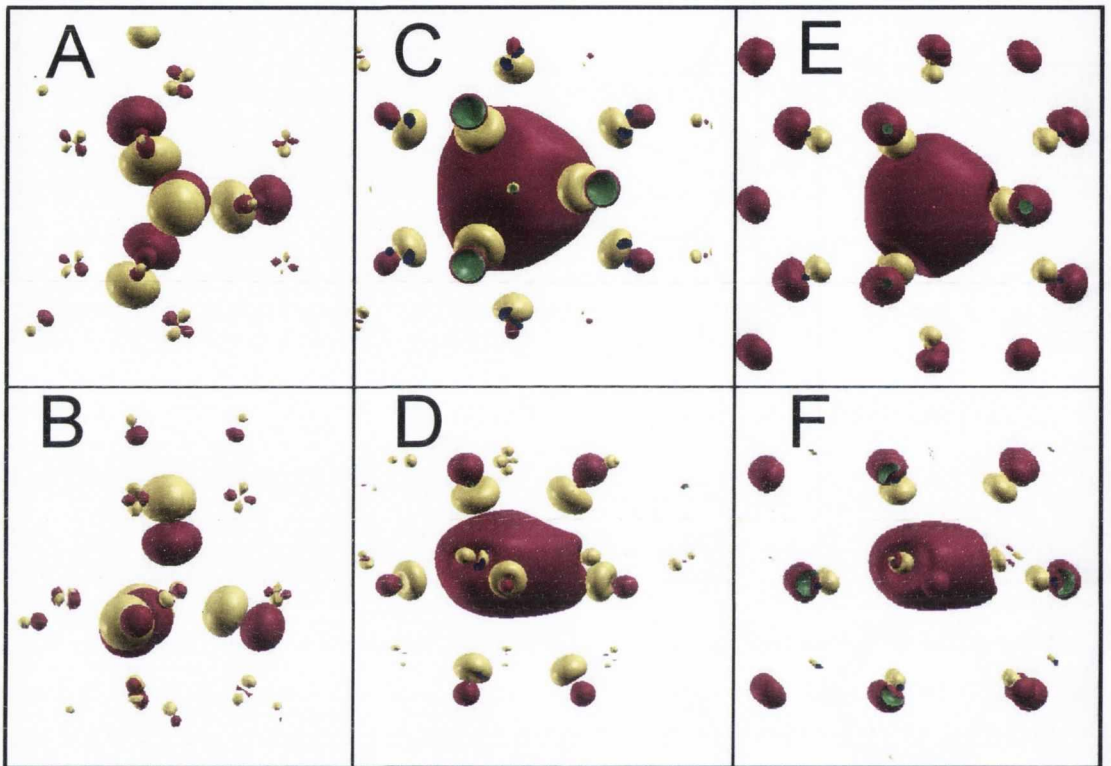


Figure 5.10: Wavefunctions for trapped electrons in V_{Zn}^- , V_{ZnO}^- , and V_{ZnO}^{2-} vacancies at the Γ point of the Brillouin zone. Trapped electron wavefunction in V_{Zn}^- (A) viewed along the c axis, (B) viewed perpendicular to the c axis. Trapped electron wavefunction in V_{ZnO}^- (C) viewed along the c axis. (D) perpendicular to the c axis. Same for V_{ZnO}^{2-} (E) along the c axis and (F) perpendicular to the c axis. Pink and yellow surfaces show +ve and -ve components of the isosurface, respectively. The green surface is the inside of the pink surface.

5.1.4 Clustered vacancy defect V_{ZnO_3}

Larger complex defects such as the ZnO_3 vacancy (V_{ZnO_3}) can trap two electrons in deep donor levels. The major difference between V_{ZnO} and V_{ZnO_3} is that V_{ZnO_3} is a much larger vacancy. V_{ZnO} is a neutral vacancy, but removing each additional oxygen atom gives two dangling electrons and therefore V_{ZnO_3} has four dangling electrons. The band structure of V_{ZnO_3} is shown in Fig. 5.11. The four dangling electrons have a spin-1 triplet ground state. The three bands related to the singlet (s1) and triplet (t1 and t2) are shown in Fig. 5.11 for different charge states. The singlet band has a lower energy while the triplets are degenerate at the Γ -point in the neutral charge state. When singly-negatively charged, the trapped electron fills one of the triplet orbitals to form a doublet but all three levels rise up in energy due to Coulomb repulsion. At partial filling, defects $\sim 11\text{\AA}$ apart show a parallel-spin ground state similar to V_{ZnO} .

Total energy calculations on the binding energies of complex defects were described previously and it was shown that the probability of formation of such a defect is higher than separated defects. Fig. 5.11 shows that V_{ZnO_3} cluster defects have a number of transition states and therefore it may support a number of optical transitions. Thus it is possible that this defect or other cluster defects of the form $V_{Zn_mO_n}$, $m < n$, may explain the interesting anomalies observed in the absorption and emission spectra of this material [5].

5.2 Effect of relaxation of crystal structure.

The crystal structure has to be relaxed whenever a defect calculation is concerned since the DFT total energy calculation does not take into account the uncompensated electrostatic interaction introduced by the defect. In the geometry relaxation procedure described in Chapter 4, the atomic coordinates are allowed to move from the ideal lattice sites and the new equilibrium is found by minimizing the total energy. Crystal structure relaxation has a large effect on the electronic structure of ZnO with intrinsic vacancy defects. Although the structure change is mainly localized in the neighbourhood of the vacancy, the effect of lattice relaxation is significant on the defect eigenvalues. The average change in

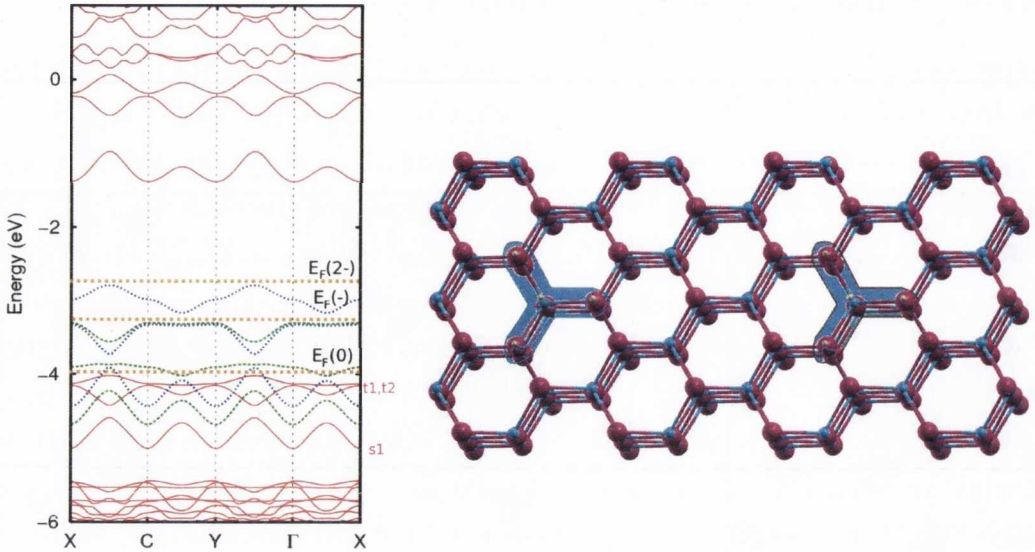


Figure 5.11: Band structure of ZnO with a neutral (V_{ZnO_3}) defect (red/solid line) superposed with the triplet states of $V_{ZnO_3}^-$ (Green/dashed line) and $V_{ZnO_3}^{2-}$ (Blue/dotted line). The states for more highly charged states are shifted up but the shift is smaller than that for V_{ZnO}^{2-} . The Fermi levels for the three charge states are shown by horizontal dotted lines. Right: V_{ZnO_3} defects in a $4\sqrt{3} \times 2\sqrt{3} \times 2$ supercell.

the crystal structure is small. One can see in Fig. 5.12 that the dispersion shape and position of only the defect band is changed upon relaxation. In Fig. 5.12 the band-diagrams of the filled levels of V_O , V_{Zn} and V_{ZnO} vacancies are shown where the red/solid lines and green/dashed lines denote the levels corresponding to relaxed and unrelaxed crystal structures respectively. The three different charge states of V_O and V_{Zn} and five different charge states of V_{ZnO} are shown.

5.3 Impurity doping in ZnO

5.3.1 Transition metal doping

Dietl *et al* [12] first predicted the possibility of a magnetic semiconductor by dilute transition metal (TM) doping in a wide band-gap semiconductor. How

5.3 Impurity doping in ZnO

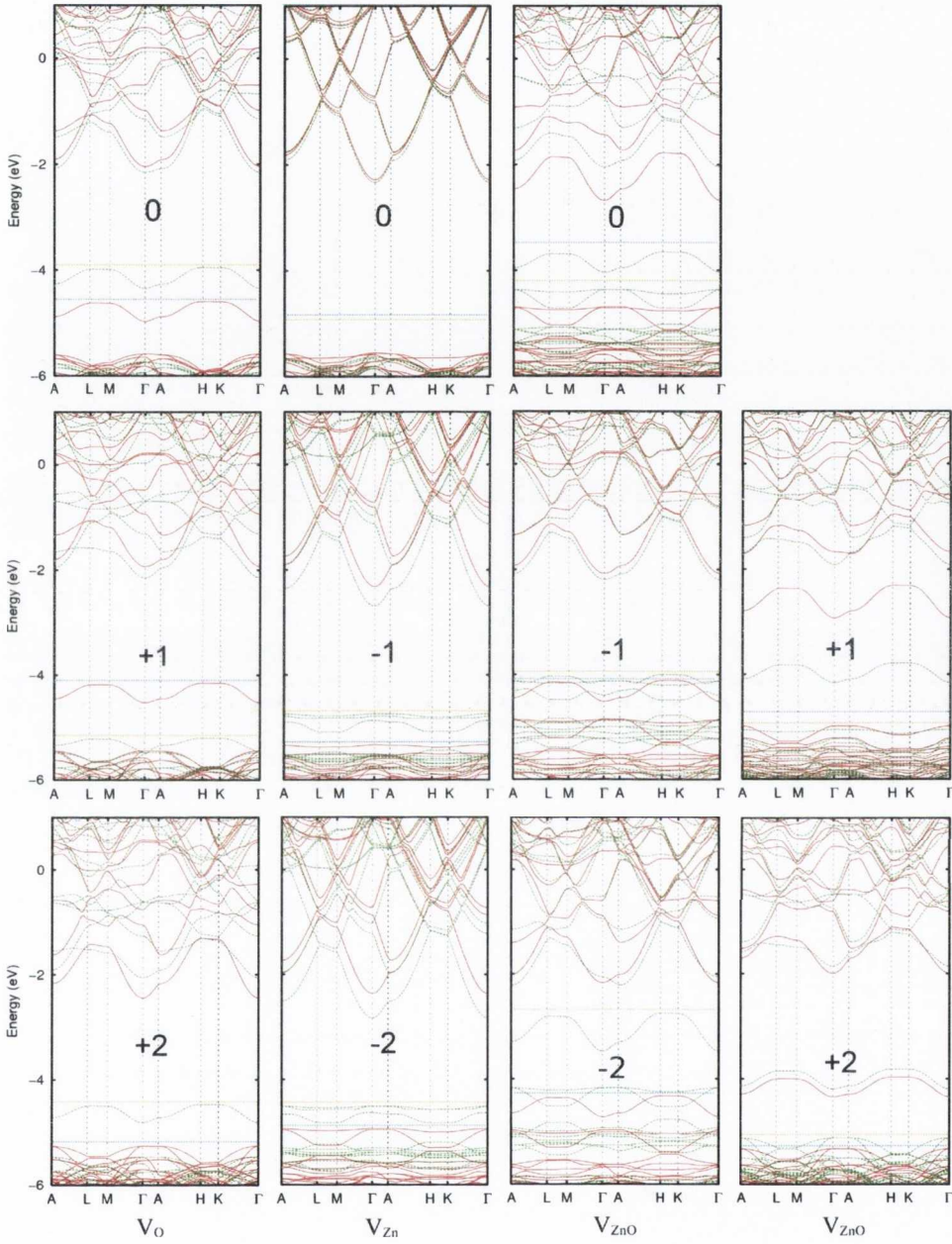


Figure 5.12: The majority-spin bandstructures of V_O , V_{Zn} and V_{ZnO} , showing the change in dispersion and energy levels due to crystal lattice relaxation. The red solid lines are the relaxed levels and the dashed green lines are the levels with ideal geometry. Fermi levels for relaxed (red) and unrelaxed (green) structures are shown by blue and yellow dotted lines, respectively.

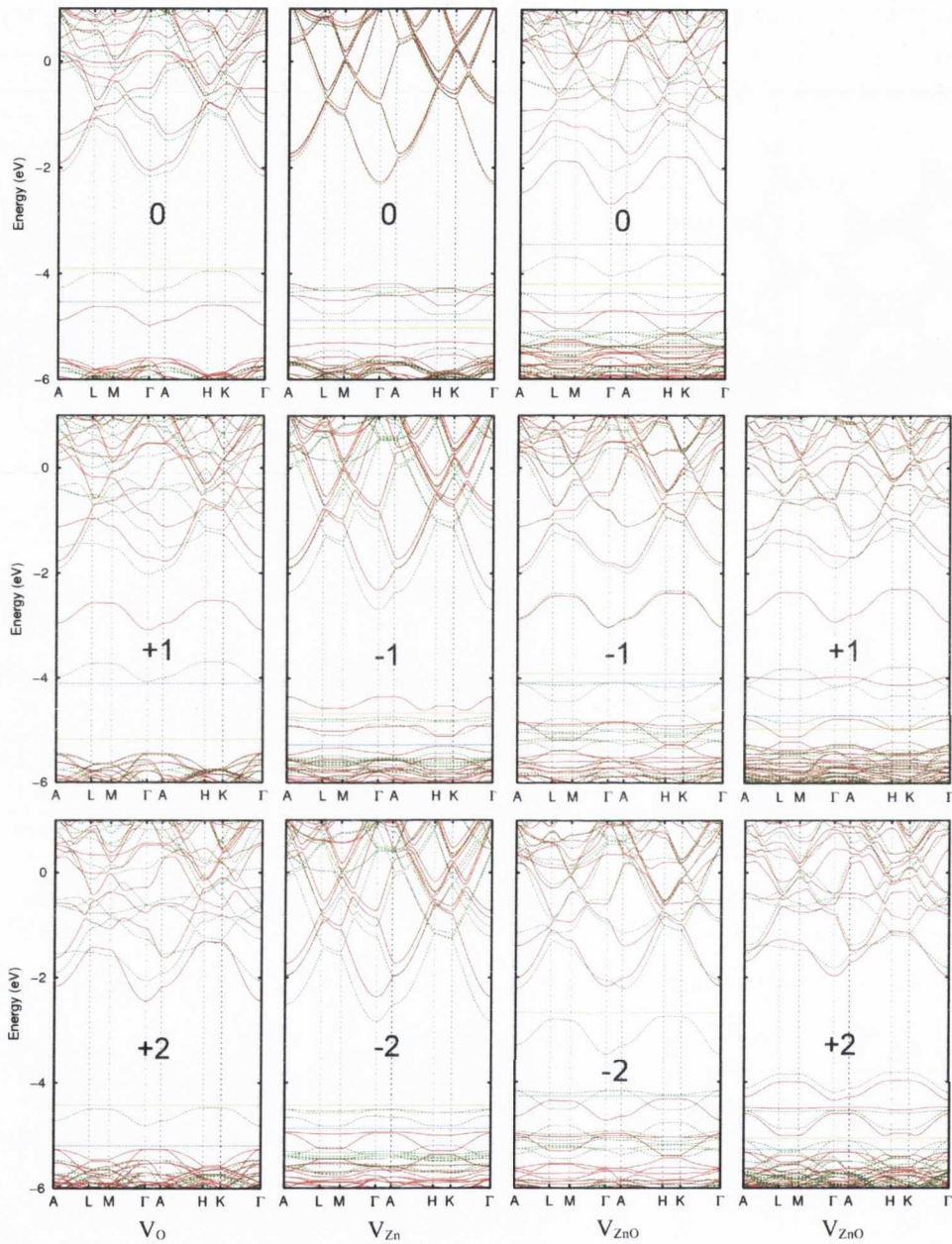


Figure 5.13: The minority-spin bandstructures of V_O , V_{Zn} and V_{ZnO} , showing the change in dispersion and energy levels due to crystal lattice relaxation. The red solid lines are the relaxed levels and the dashed green lines are the levels with ideal geometry. Fermi levels for relaxed (red) and unrelaxed (green) structures are shown by blue and yellow dotted lines, respectively.

5.3 Impurity doping in ZnO

room temperature ferromagnetism exists in nonmagnetic oxides with TM doped only by a very dilute amount (4 - 7 %), has been a highly debated subject [15, 20, 45, 59, 165]. Several different TM impurities were doped in ZnO and it was found that Co-doped ZnO thin films show the largest magnetic moment [17].

Here we present the electronic structure of $\text{Zn}_{1-x}\text{Co}_x\text{O}$ calculated using B3LYP. Calculation of exchange coupling constants between defect - Co and Co-Co and further discussion are given in Chapter 6. In the calculation of the electronic structure of $\text{Zn}_{1-x}\text{Co}_x\text{O}$, a $3 \times 3 \times 2$ supercell with 72 atoms was used. Substitution of two Zn atoms with Co atoms is used to calculate the exchange constant between Co atoms. This gives a Co concentration $x \sim 5.5\%$ which is similar to the concentration used in most DMS related experiments. The majority and minority bandstructures of $\text{Zn}_{1-x}\text{Co}_x\text{O}$ ($x = 5.5\%$) with one V_{ZnO}^- vacancy are shown in Fig. 5.14.

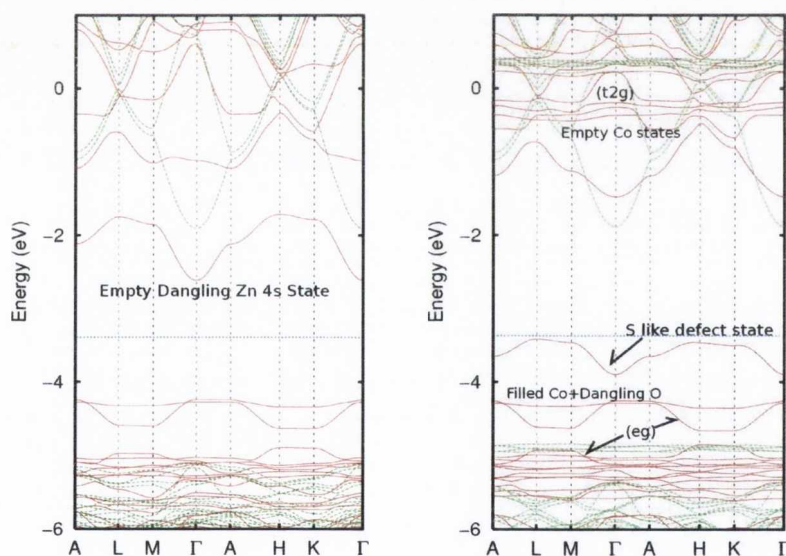


Figure 5.14: Majority (left) and minority (right)-spin bandstructure of $\text{Zn}_{1-x}\text{Co}_x\text{O}$: $x=0.055$ with one V_{ZnO} defect (red) compared to $\text{Zn}_{1-x}\text{Co}_x\text{O}$ (green) without any defect. The Fermi level is shown by horizontal blue dotted line.

The dispersion in the V_{ZnO} defect state does not change, there is a little shift in energy though. Crystal-field degeneracy splits Co-3d states. Here, the empty

t_{2g} states are about 5 eV higher than the filled e_g states. Note that the filled e_g states couple with the dangling O-2p states and the s -like defect state.

5.3.2 Electron doping with aluminum co-doping

We have discussed electron trapping in vacancies in n-type ZnO thin films. In these calculations electrons and holes were inserted in the supercell to create n-type or p-type environments which also lead to the creation of a compensating jellium of opposite background charge. In practice control of n-type doping is achieved by variable Al co-doping [44] in ZnO. In order to investigate whether Al doping will alter the electronic and crystal structure and the difference between pure electron-insertion and Al-doping, one Al atom is substituted for a Zn atom in a ZnO supercell with a V_{ZnO} defect.

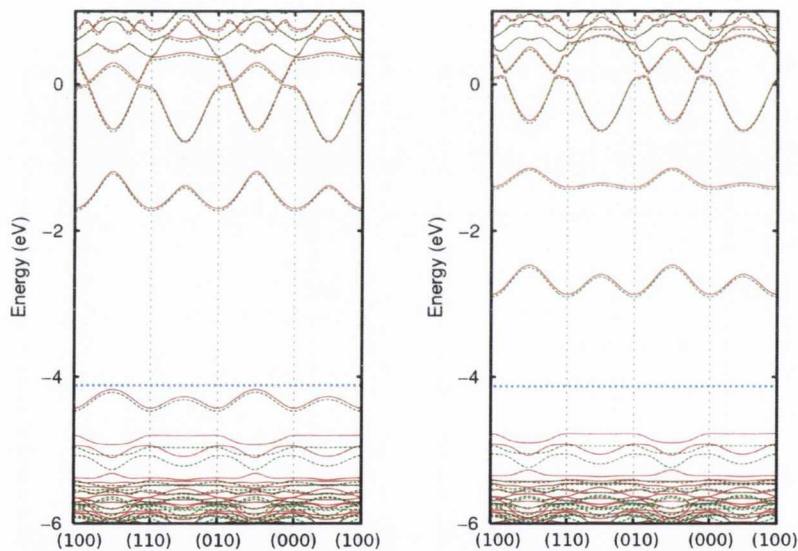


Figure 5.15: Majority (left) and minority (right) bandstructures of $V_{ZnO}^0 + Al_{Zn}$ (red/solid) comparing with V_{ZnO}^- (green/dashed) obtained using a fully relaxed $2\sqrt{3}\times 2\sqrt{3}\times 2$ supercell. The Fermi level does not change and is shown by blue dotted line. Note that a square k-path is used for this cuboid supercell.

Calculations suggest that when an Al atom substituted for a Zn atom, the extra electron resides in the vacancy. The crystal structure was relaxed and due

to the similar ionic size of Al and Zn, very little displacement is observed around the substitutional Al atom. In Fig. 5.15 the band-diagram of Al_{Zn} with V_{ZnO}^0 , is compared with the band diagram of a V_{ZnO}^- . Both of the calculations were done with relaxed crystal structures in a cuboid $2\sqrt{3}\times 2\sqrt{3}\times 2$ supercell. There are minimal differences between the energy levels on the both sides of the energy gap. This confirms that the electron donated by Al migrates to the vacancy and gets trapped, even when the Al_{Zn} substitutional site is fairly far away from the vacancy site (in this case 6.3\AA).

5.4 Conclusion

In this chapter, we have discussed the crystal and electronic structure of intrinsic vacancy defects oxygen vacancy, zinc vacancy and ZnO divacancy. The electronic energy levels were plotted against the wave-vectors and states dominating the electronic properties are identified. The wave function of the defects were simulated to characterise the defect and to understand the result of some EPR and PAS experiments. The V_{ZnO} vacancy was found to have a nodeless *s*-like wave-function associated with a moderately dispersive band with a bandwidth of ~ 0.4 eV. This defect can trap up to two electrons or up to two holes, enabling it to obtain five different charge states (-2 to +2). The transition levels between these charge states and value of Hubbard- U are calculated in the next Chapter.

The Zn vacancy, traps two electrons in a dangling O-2*p* state and has a smaller bandwidth of ~ 0.1 eV. The localised holes in the neutral V_{Zn} form a triplet ground state.

Lattice relaxation has a large effect on defect electronic structure. The overall change in crystal structure of the supercell is small, a defect may relax by up to $0.3 - 0.7\text{\AA}$ depending on the charge state of the defect. In the next chapter we will discuss the formation energies and transition levels of the defect and the effect of lattice relaxation on these quantities.

Chapter 6

Calculation of Defect Formation Energies, Transition Levels and Hubbard- U values

Electronic structures of the vacancy defects show that these intrinsic vacancy defects (V_O, V_{Zn} and V_{ZnO}) are capable of trapping electrons or holes depending on the fermi level of the system and that the V_O and V_{ZnO} defect energy levels have moderate bandwidth associated with a large s -like wavefunction. This implies that these trapped electrons may interact at long range limited by the spread of their wavefunction. Yet it is still unknown from these results whether these defects have a large Hubbard- U , so that they can support the model of room temperature FM proposed in Chapter 2. It is also unclear which of the defects would have a lower formation energy and in what charge state they are most likely to exist at certain fermi level. This last criterion is important for paramagnetism because a defect is required to be stable in a singly charged state in order to retain a finite magnetic moment and act as a paramagnetic centre. This is important also for photoluminescence as there are a number of transitions possible between different charge states of a defect and it is essential to know which transition is more probable than the others in order to identify a particular transition associated with a particular colour emission. The exact optical transition energies of the defect states can be estimated from the calculation of transition levels to identify roles of different defects as colour centres.

In this chapter we discuss the results from the defect formation energy and transition level calculations, from which estimates were made for Hubbard $-U$ and optical transition energies. Formation energy calculations have been carried out for each of the three defects V_O , V_{Zn} and V_{ZnO} . The formation energy of a defect gives an estimate of the stability of the defect and the probability of formation of a defect from a thermodynamic point of view. It is the energy cost for defect formation. Thus the lower the formation energy is, the higher the probability of forming a defect. The transition level on the other hand, is the energy cost to change the electron occupation of a defect level. This quantity reveals in which charge state the defect state is most likely to be found at a particular fermi level of the system. The Hubbard- U of a defect is the Coulomb repulsive energy cost to add an electron to an already half-filled defect level and therefore can be calculated from the transition levels. The importance and calculation techniques of these quantities were discussed in Chapter 4. It is important that the formation energies are calculated with the crystal structure of the system fully relaxed in the particular charge state of the defect that is being calculated. In Chapter 5 we have seen that there is a large effect of lattice relaxation on the local electronic and crystal structure of the defect. We will also discuss the importance of calculating the transition levels with unrelaxed structures from different methods along with the relaxed structures.

There is an alternate method of calculating the transition levels; from the electronic band diagram using Janak's theorem [156]. Both of the methods have been discussed in Chapter 4. The transition level values calculated from the two methods agree with each other in general but almost always there is a considerable difference between them. This anomaly is also discussed in this chapter.

6.1 Formation energies

Eqn. 4.1-4.7 were used to estimate the formation energies from total energy calculations. The results are given in Table 6.1. B3LYP was used in most of the calculations but LDA calculations were also carried out for some defects to compare the values with previous LDA calculation results.

6.1 Formation energies

Table 6.1: Formation energies for intrinsic vacancy defects compared to literature values. All values in this work are for relaxed geometries and obtained using the $3\times 3\times 3$ supercell. Oxygen poor growth conditions were assumed with $E_F = E_V$, all values are in eV.

Functional	V_O	V_O^+	V_O^{2+}	V_{Zn}	V_{Zn}^-	V_{Zn}^{2-}	V_{ZnO}	V_{ZnO}^-	V_{ZnO}^{2-}	V_{ZnO}^+	V_{ZnO}^{2+}
B3LYP ¹	0.5	-1.2	-3.7	7.5	8.1	8.7	4.2	6.6	8.4	3.6	3.4
HSE ²	1.0		-3.4	7.1	8.0	10.1					
GGA ³	1.0	0.3	-0.5	5.4							
LDA ¹	0.4			5.1			4.0				
LDA ⁴	0.0	0.2	-0.3		5.5	5.8	6.6				
LDA ⁵	1.5	0.8	-0.5	5.8	5.7	5.8					
LDA ⁶	0.7	0.6	-0.4	5.9	6.0	6.3					
LDA+U ⁶	1.3	0.8	-0.6	6.4	6.5	6.9					
GGA+U ³	1.7	0.7	-0.7	5.6	6.0	7.1					

Formation energy values previously computed by several other groups are also given in the table for comparison. We know that the hybrid functional used here gives quite an accurate estimate of the ZnO band gap and describes occupied levels more accurately than LDA for wide-gap oxides [36, 38, 132]. Thus it is expected that the formation energies as well as the transition energies obtained using the hybrid B3LYP functional will predict more accurate values than that obtained using conventional LDA. The values presented in Table 6.1 were calculated using a fully relaxed $3\times 3\times 3$ supercell. Details of the supercells used are given in Appendix A.

The transition levels are calculated using Eqn. 4.9. The formation energies of charged defects are related to the transition levels by Eqn. 4.8. The calculation of transition levels and the band gap are discussed in the next section. Formation

¹This work, all values correspond to calculation converged down to 10^{-3} eV, rounded off to 10^{-1} eV for comparison.

²Ref. [63]

³Ref. [166]

⁴Ref. [64]

⁵Ref. [167]

⁶Ref. [90]

energies are plotted against the fermi level position for all the defects in Fig. 6.1. These figures give an insight into the charging of the defect states and the occurrence of the defect level in a certain charged state at a certain fermi level. This is helpful in predicting the stability of each charge state for different vacancy defects. The defect should be stable in a singly charged state in order to act as a paramagnetic centre. These diagrams tell us whether the defect is likely to exist in a singly charged state or not. The solid lines show the formation energy of the defect states with respect to the fermi level while the dashed lines denote the same for unstable states.

The V_O^+ vacancy has been shown previously to be unstable [36, 64] and this is confirmed in this work (Fig. 6.1). Formation energies predicted in this work using B3LYP are close to the numbers obtained by Oba *et al* [63] using the HSE hybrid functional [33]. Again the values obtained in this work using LDA are similar to the values obtained by other groups using LDA. The formation energies of V_O^{2+} obtained by hybrid functionals are in the range -3.4 to -3.7 eV where the LDA values are of the range -0.3 to 0.7eV. Underestimation of the chemical potential of oxygen by around 3 eV makes a significant difference between the hybrid functional and LDA values. The formation energies of V_{Zn} and V_{ZnO} in different charge states are also underestimated, but not by as much as for V_O .

We have discussed the effect of relaxation of crystal structure on electronic structure before. It also has a large effect on the formation energy and transition levels of the charged vacancy defects. The change in crystal structure is large around the defect site and relatively very small elsewhere. The displacements in the atomic positions of the neighbours to the defect site are different for each charge state of the defect. As a result, the formation energy of each charge state, as well as the transition levels suffer large change upon relaxation. Fig. 6.1 depicts formation energies of the three vacancy defects with respect to Fermi-level. The unstable states are represented by a dotted line. When the structure is relaxed, the V_O^+ state rises and becomes unstable, thus agreeing with previous works [36, 64]. The upper limit of fermi level position at which V_O^{2+} exists, also increases from ~ 1.2 eV to ~ 2.3 eV. Also the V_{ZnO}^- state becomes unstable upon relaxation. One can see in Fig.6.1 that the dotted line representing V_{Zn}^- touches the solid line for V_{Zn}^0 and V_{Zn}^{2-} precisely at the point of the transition between

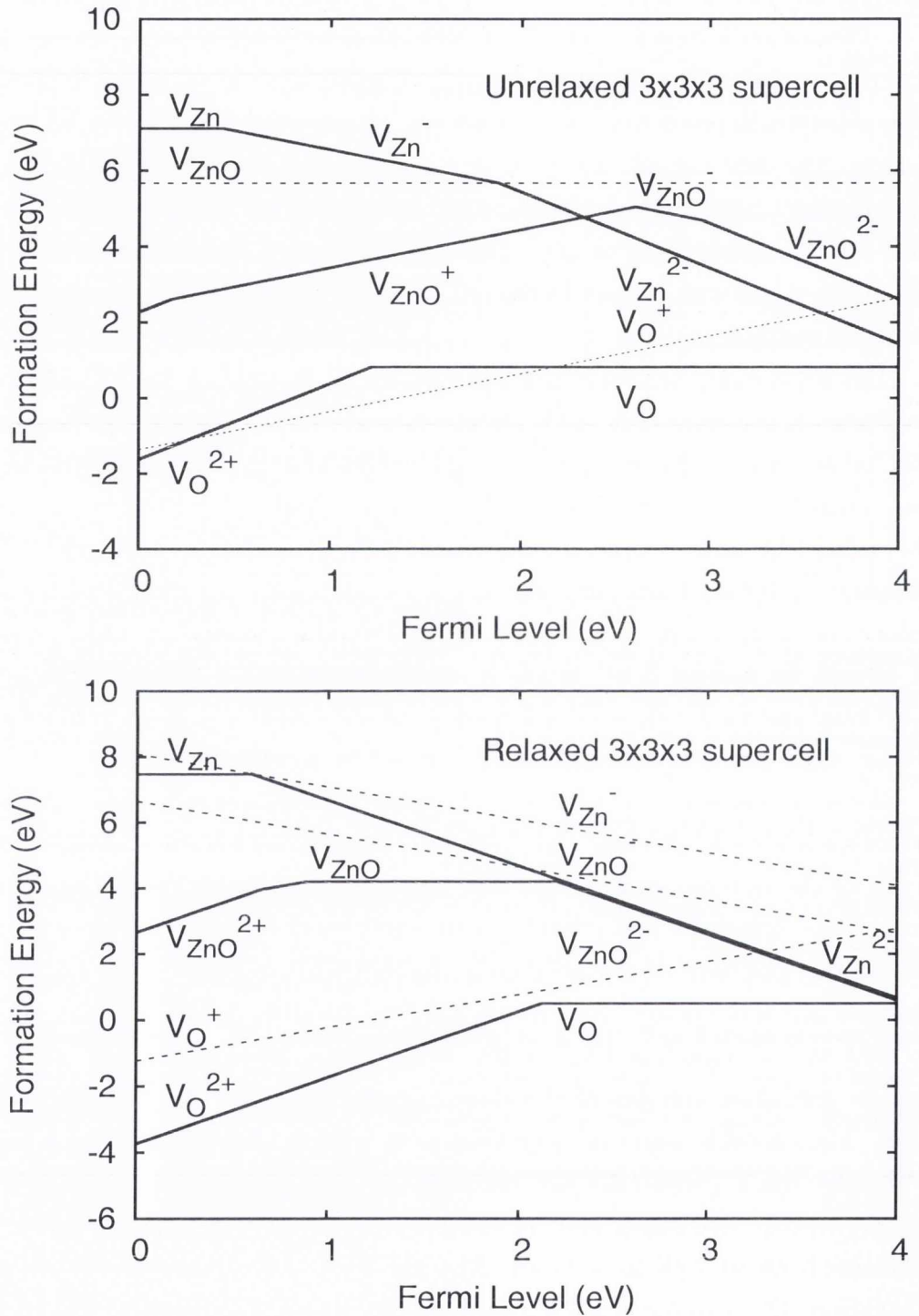


Figure 6.1: Defect formation energies as a function of Fermi level position for V_O , V_{Zn} and V_{ZnO} . These two diagrams show formation energies for a $3 \times 3 \times 3$ supercell when the crystal structure is unrelaxed (top) and fully relaxed (bottom).

these two states. This signifies that for this defect the transition levels among these three states are the same (See Table. 6.3). In other words the V_{Zn}^- state has the same probability of occurrence as the other two charge states. The V_{Zn}^{2-} state exists over a large range of Fermi level positions and indicates that V_{Zn} is likely to trap two electrons in an n-type atmosphere. This supports the PAS observations by Tuomisto *et al* [89, 104], mentioned in Chapter 2. The pair vacancy V_{ZnO} , on the other hand, has five charge states, out of which, the V_{ZnO}^- state is unstable. The V_{ZnO}^{2-} state has the largest range of stability at the higher values of fermi-level. The V_{ZnO}^+ and V_{ZnO}^{2+} states have a lower formation energy than the neutral V_{ZnO} , but exist for low fermi-levels (Fig. 6.1).

Since relaxation of crystal structure massively affects the formation energies, the energetics of the relaxation process were investigated further. The relaxation energy is a quantity that can give us information about the energy cost associated with the relaxation process. The relaxation energy can be defined by,

$$E_{Rel} = (E_{TOT}^{unrelaxed}(X^q) - E_{TOT}^{relaxed}(X^q)) \quad (6.1)$$

where $E_{TOT}^{unrelaxed}(X^q)$ is a supercell containing a defect at charge state q . Atomic positions of this supercell are fixed to bulk equilibrium atomic positions. $E_{TOT}^{relaxed}(X^q)$ is the total energy of the same system but fully relaxed. E_{Rel} gives the energy cost for relaxing the supercell with a defect in a particular charge-state. From the definition of formation energy (Eqn. 4.1) we can say that the relaxation energy is simply,

$$E_{Rel} = E_{unrelaxed}^f(X^q) - E_{relaxed}^f(X^q) \quad (6.2)$$

When the system is charged ($q \neq 0$), the shift of fermi level contributes to the formation energy expression (Eqn. 4.1). The relaxation of a neutral defect supercell was started with relaxed bulk atomic positions with the defect atom removed. Then a charge, either a hole or an electron, was inserted in the supercell and relaxed again in a singly charged state. This was repeated with a second charge inserted and we get the relaxed structures of doubly occupied (2-) or empty (2+) defects. Every time the supercell is relaxed in a new charge state, the total energy difference of the system before and after relaxation represents the relaxation energy associated with defect charging. This quantity can be defined as,

$$E'_{Rel}(q'/q) = E_{TOT}^{unrelaxed}(X^{q'}) - E_{TOT}^{relaxed}(X^q) \quad (6.3)$$

where q and q' are two different charge states of the defect X . $E_{TOT}^{unrelaxed}(X^{q'})$ does not correspond to the fully unrelaxed ideal crystal structure but to the same crystal structure that corresponds to $E_{TOT}^{relaxed}(X^q)$. Therefore for a neutral vacancy starting with the bulk atomic positions, $E'_{Rel} = E_{Rel}$. This quantity helps us to understand the energy cost associated with relaxation between different charge-states of a defect. In the next section we will discuss the transition levels of the defects. E'_{Rel} gives an estimate of the energy cost of the lattice to relax when the defect charge state changes. The implication of this quantity in predicting defect related optical properties is discussed in the next section. Table 6.2 shows the comparison of formation energies and relaxation energies for each defect state. For one particular defect, E'_{Rel} denotes the relaxation energy of the particular charge state given in the column heading with respect to the charge state of the column to its left. E'_{Rel} for the neutral vacancies ($q = 0$) are the absolute relaxation energies and are same as E_{Rel} . Note that the relaxation energies are much smaller than the formation energy change upon relaxation.

Table 6.2: Relaxation energies for intrinsic defects in different charge states in eV. Comparison is made with the formation energies with relaxed and non-relaxed geometries. E'_{Rel} values of a column shows the relaxation energy between that column and the column at its left (see text)

	V_O	V_O^+	V_O^{2+}	V_{Zn}	V_{Zn}^-	V_{Zn}^{2-}	V_{ZnO}	V_{ZnO}^-
Formation energy (Non-relaxed)	1.3	-0.9	-1.12	7.4	7.8	9.7	5.9	9.7
Formation energy (Relaxed)	0.5	-1.2	-3.7	7.5	8.1	8.7	4.2	6.6
Relaxation energy (E'_{Rel})	0.3	0.8	1.1	0.5	0.4	0.4	1.4	0.6

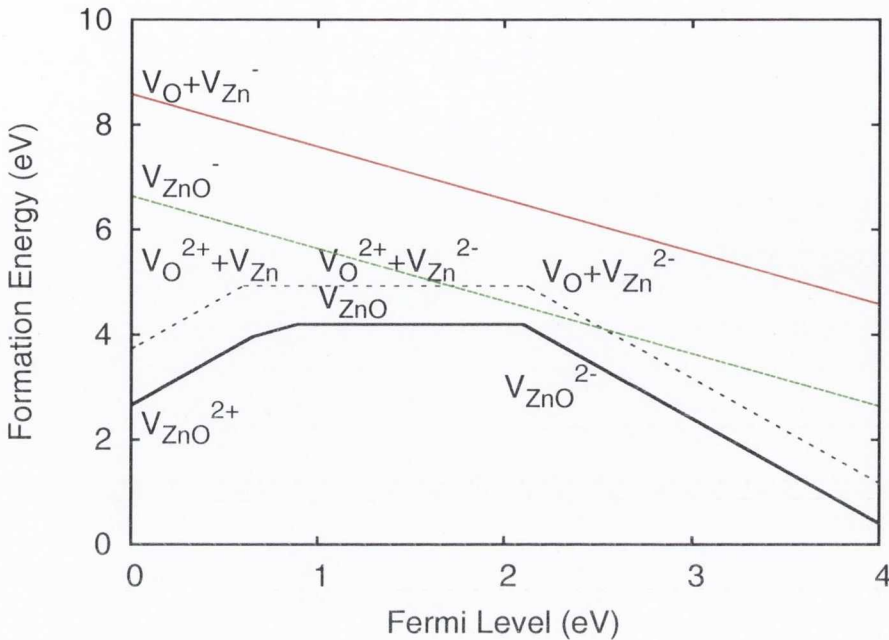


Figure 6.2: V_{ZnO} pair vacancy formation energies as a function of fermi level position compared with V_O and V_{Zn} . V_{ZnO}^- has a formation energy about 2 eV lower than the separated $V_O + V_{Zn}^-$.

Fig. 6.2 shows the V_{ZnO} vacancy formation energy with respect to fermi level. The values were obtained from a relaxed $3 \times 3 \times 3$ supercell. The combined formation energy of V_O and V_{Zn} is also plotted in the same diagram. Note that the formation energy of a Schottky V_{ZnO} pair vacancy defect is lower for all charge states than the combined formation energy of $V_O + V_{ZnO}$. Formation energy of a V_{ZnO}^- is lower by about 2 eV than that of combined $V_O + V_{Zn}^-$. This agrees with the binding energy calculation results for a pair defect described at the beginning Chapter 5, where we saw that the total energy of a supercell with a V_{ZnO}^- defect is lower by 2 eV than that of the same supercell with separate $V_O + V_{Zn}^-$.

6.2 Defect transition levels

The transition levels are estimated from total energies using equations 4.10 and 4.11. The relationship between transition levels and formation energies is estab-

lished in Eqn. 4.8. The values of transition levels relative to the valence band maximum (E_V) are given in Table 6.3. The value of the energy band gap E_g is required in the equations 4.10 and 4.11. The band gap was also calculated from total energies of charged bulk ZnO systems using Eqn.4.14 and was found to be 3.7 eV for the supercell-size $3 \times 3 \times 3$ that has been used in most of the formation energy and transition level calculations. When we compare this value of band gap to the value obtained from single particle eigenvalues, we have 3.3 eV. The experimental band gap is 3.4 eV [56]. The band gap is clearly overestimated in this method and requires an explanation. The above value of 3.7 eV was obtained using charged $3 \times 3 \times 3$ supercells with three different calculations with charge states: neutral, (charge 0) an extra hole (charge +1) and one extra electron (charge -1). Total energies of these three differently charged supercells are required for calculating E_g using Eqn. 4.14. The electronic concentration differs for this type of calculation for supercells of different size and due to the use of periodic boundary conditions, the extra charge in the supercell as well as the compensating background charge interact with their periodic images, adding contributions to the total energy. This phenomenon is discussed in Chapter 4 and can be solved by Makov-Payne correction (Eqn.4.18) [155]. The strength of this interaction reduces as a polynomial function of reciprocal of supercell size and thus the value of E_g slowly falls as the supercell size increases. Along with the $3 \times 3 \times 3$ supercell, the same calculation for E_g was repeated for a $2 \times 2 \times 2$ and a $4 \times 4 \times 4$ supercell. The value of E_g is plotted against $1/L$, L being the supercell length 2, 3 and 4 (See Fig. 6.3). If only the first term of Eqn. 4.18 is considered, E_g can be extrapolated in a linear fashion. The linear extrapolation tells us that the band gap for an infinitely large supercell (at $L = \infty$, interactions between periodic images are zero) is 3.2 eV, thus in better agreement with the experimental result.

The Hubbard- U value of a defect can be calculated from the transition levels and is discussed later in this chapter. An estimate of Hubbard- U is necessary in order to confirm whether a defect acts as a paramagnetic centre and may promote ferromagnetism in a Hubbard model described in Chapter 2. The transition energy values are also important as they can give an estimation of the optical absorption/emission energy in the energy spectrum of a particular defect-related

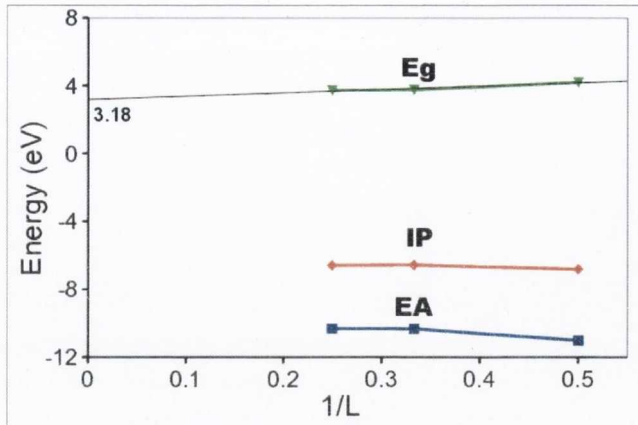


Figure 6.3: Estimation of band gap using total energies. Extrapolation towards infinitely large supercell has been shown by thin black line.

system. A number of absorption/emission signals have been observed in ZnO thin film spectra that do not come from pure bulk ZnO. For example, ZnO thin films prepared by molecular beam epitaxy show a green and a yellow luminescence respectively in oxygen-rich and Zn-rich growth conditions [11]. Naturally the green and yellow luminescence were attributed to transitions of charge trapped in Zn and O F-centre vacancies respectively [11]. Kohan *et al* [64] tried to explain the green luminescence from transition level calculations using LDA and since then a significant number of works have been made in predicting the optical transition levels from first principles calculations. The optical transition energies were estimated from the transition levels with the aid of the Frank-Condon principle [69, 168]. Vidya *et al* [111] however, pointed out that the thermodynamic transition energy is not exactly the same as the optical transition energy, but the difference is close to that when the atomic relaxation energy associated with the transition is low. When an F-centre is involved in an optical process, the optical transition energy is the ionization energy of the F-centre. The transition level $\epsilon(q'/q)$ for unrelaxed supercells in charge states q' and q represents the ionization energy of a particular defect. When the supercell is relaxed with charges q and q' , the transition level $\epsilon(q'/q)$ represents the energy cost to ionize the defect from charge state q to charge state q' at equilibrium of crystal forces. When the charge state of a defect changes from q to q' , the crystal structure is relaxed with the

initial charge state q . As the charge state changes to q' , the crystal structure relaxes until it comes to equilibrium for the final charge state q' . However, the optical recombination is much faster (order of 10^{-15} second¹) than the atomic relaxation process (order of 10^{-12} second) and the energy associated with the optical transition is not as the same as the transition level at equilibrium. The energy associated with an optical transition is therefore the transition energy cost from an initial charge state q with a fully relaxed crystal structure to the final charge state q' with the same crystal structure (fully relaxed with the initial charge state q). Since the transition energy $\epsilon(q'/q)$ represents the transition energy in equilibrium with crystal structures fully relaxed with both of the charge states, in order to estimate the optical transition energy $\epsilon(q'/q)_{opt}$ from $\epsilon(q'/q)$ we have to add the energy cost to relax the crystal structure when the charge state changes from q to q' , which is E'_{Rel} (Eqn.6.3). The quantity E'_{Rel} can be identified with the Frank-Condon shift [71]. Thus,

$$\epsilon(q'/q)_{opt} = \epsilon(q'/q) + E'_{Rel}(q'/q) \quad (6.4)$$

Table 6.3 shows a comparison of transition levels (TL) done in this work and other works. Note that LDA/LDA+U calculations underestimate transition levels. Transition level values are calculated with a relaxed $3 \times 3 \times 3$ supercell and therefore represent transition energies at equilibrium. From Table 6.3 and Table 6.2 we can predict the origin of the anomalies observed in the ZnO photoluminescence [11, 169]. For example, the origin of the green luminescence, associated with an energy of 2.4 eV [11], remained a topic of major controversy. Some first principles calculations attributed the green luminescence to the (+/0) transition in V_O [69, 71, 111] and in this work we also find the $\epsilon(+/0)_{opt}$ for V_O to be 2.5 eV (using Eqn. 6.4 from values in Tables 6.3 and 6.2, $\epsilon(+/0)$ (1.7 eV) + $E'_{Rel}(+/0)$ (0.8 eV) = 2.5 eV). However the green luminescence is found in Zn-poor films [11] and more likely to be related to V_{Zn} . Therefore Vidya *et al* [111] suggested that the green luminescence is more likely to be from a (2+/+) transition in V_{ZnO} defect which was found also have an optical transition energy of 2.5 eV

¹The order of magnitude of the electronic recombination time can be estimated from Heisenberg's uncertainty principle $\Delta E \Delta t \approx \hbar$. $\hbar = 4.135 \times 10^{-15}$ eV and ΔE being in the order of 1 eV, $O(\Delta t) \sim 10^{-15}$ s.

6.2 Defect transition levels

Table 6.3: Transition levels in eV relative to E_V . A fully relaxed $3 \times 3 \times 3$ supercell is used for these calculations.

Defect	q $'$ /q	LDA ¹	LDA+U ¹	B3LYP ²	B3LYP ³	HSE ⁴
V _O	+/0	0.1	0.5	1.7	1.8	
	2+/ $+$	1.0	1.4	2.5	2.7	
	2+/0			2.1	2.2	2.2
V _{Zn}	-/0	0.1	0.1	0.6		0.9
	2-/-	0.3	0.4	0.6		2.5
	2-/0			0.6		
V _{ZnO}	2+/0			1.5		
	2+/ $+$			0.9		
	+/0			0.6		
	-/0			2.4		
	2-/-			1.9		
	2-/0			2.2		

[111]. The shift from green to blue luminescence at a high-intensity laser incident pulse [106] was previously attributed to the (-/0) and (2-/-) transition of the site inversion defect O_{Zn} [111]. From the results of this work we can suggest that the blue luminescence may also be attributed to the (2-/-) transition of the V_{ZnO} defect. The optical transition energy of this transition is 2.7 eV ($\epsilon(2-/-)$ (1.9 eV) + $E'_{Rel}(2-/-)$ (0.8 eV) = 2.7 eV) and V_{ZnO} has a lower formation energy than O_{Zn} [111].

There is also a yellow luminescence observed at 2.37 eV [40, 169] in O-rich samples. Presumably this is caused by Zn vacancies but none of the V_{Zn} optical transition energies estimated in this work agrees with this. Vidya *et al* identified this yellow luminescence with the (+/2+) transition of V_{ZnO}^{Radial} which is a different configuration of the V_{ZnO} Schottky defect shown in Fig. 5.6.

¹Ref.[90]

²This work, all values correspond to calculation converged down to 10^{-3} eV, rounded off to 10^{-1} eV for comparison.

³Ref[71]

⁴Ref[63]

6.2.1 Transition levels from single particle eigenvalues

In the above section, transition level values discussed are obtained from total energy (TE) calculations but they can also be estimated from single particle eigenvalues (SPE) derived from the same density matrix used to obtain the total energy in the same computation procedure. Janak's theorem is used to obtain the values of transition energies with respect to E_V . The details of this method are discussed in Chapter 4; Eqn. 4.9 and Eqn. 4.17 are used to estimate the transition level values. The energy eigenvalues of the relevant states at the Γ -point are obtained from the electronic band diagrams shown in Fig. 5.13. The transition is between the filled and empty levels for electrons and the other way around for holes, so either the majority or the minority levels are to be considered for the measurement of $\epsilon_{h+1}(N)$ and $\epsilon_{h+1}(N+1)$ in spin polarised systems. e.g., for transitions such as (+/0) or (-/0) the majority and the minority levels are considered, respectively, for the spin polarised +1 or -1 systems [71].

In Chapter 4, we have discussed that using a single-point (Γ) eigenvalue instead of averaging over all k-points may cause inaccurate results in this method. However, results show that (Table 6.4) the estimations of the transition levels are in broad agreement with the TL values estimated using TE method. Transition energy values are tabulated in Table 6.4.

Table 6.4: Transition levels in eV relative to E_V , using B3LYP. Comparison is made between the total energy and single-particle eigenvalue methods obtained using fully relaxed (Rel) and unrelaxed(NRel) 3x3x3 supercell. The deviation of SPE values from TE values are given by ξ . Absolute deviations from the mean values of ξ are also shown. Note that all TE values correspond to calculation converged down to 10^{-4} eV, rounded off to 10^{-1} eV for comparison with SPE values which are correct down to 1st decimal places only.

Defect	q/q'	TE Method		SPE method		Error ($\xi = \epsilon(SPE) - \epsilon(TE)$)			
		Rel	NRel	Rel	NRel	$\xi(\text{Rel})$	$ \xi - \bar{\xi} (\text{Rel})$	$\xi(\text{NRel})$	$ \xi - \bar{\xi} (\text{NRel})$
V_O	+/0	1.7	2.2	1.5	1.3	-0.2	0.1	-0.9	0.6
	2+/-	2.5	0.3	2.1	0.4	-0.4	0.3	0.1	0.4
	2+/0	2.1	2.4	1.8	2.1	-0.3	0.2	-0.3	0.0
V_{Zn}	-/0	0.6	0.4	0.2	0.9	-0.4	0.3	0.5	0.8
	2-/-	0.6	1.9	0.4	0.8	-0.2	0.1	-1.1	0.8
	2-/0	0.6	1.2	0.4	1.0	-0.2	0.1	-0.2	0.1
V_{ZnO}	2+/0	1.5	3.6	2.0	3.9	0.5	0.6	0.3	0.6
	2+/-	0.9	2.0	1.0	1.4	0.1	0.2	-0.6	0.3
	+/0	0.6	3.8	0.8	2.5	0.2	0.3	-1.3	1.0
	-/0	2.4	1.9	1.9	2.0	-0.5	0.4	0.1	0.4
	2-/-	1.9	3.2	2.2	2.9	0.3	0.4	-0.3	0.0
	2-/0	2.2	2.6	2.1	2.5	-0.1	0.0	-0.1	0.2

Fig. 6.4 depicts the comparison between the transition levels obtained from the two different methods for both relaxed and unrelaxed crystal structures. Note that the TL values calculated from the two methods are not exactly the same. In both of the TE and SPE methods the transition levels are obtained using the relaxed systems for all charge states. The data is shown in Table 6.4.

The deviation (ξ) in the SPE TL values are calculated with respect to the TE values and given in Table 6.4. The absolute maximum errors for relaxed ($\xi(\text{Rel})$) and unrelaxed TL values ($\xi(\text{NRel})$) are 0.5 and 1.3 eV, respectively. The standard deviations (root mean square deviation) in $\xi(\text{Rel})$ and $\xi(\text{NRel})$ are 0.3 and 0.6 eV, respectively. Note that for the unrelaxed values the error and its deviation are almost double that of the relaxed values. The absolute mean deviation (AMD) for each of the values are also shown in Table. 6.4. The maximum AMD for unrelaxed values (1.0 eV) is almost double of that of the relaxed values (0.6 eV). From these statistics we can see that, although the TE and SPE values are quite close, the errors are not negligible. If we compare these values with optical recombination energies, these errors are larger than the energy that is needed to shift the luminescence colour from green to yellow (~ 0.2 eV). Therefore predictions of optical transition energies from TL calculations made using the current framework of SPE method will not be accurate.

TL values calculated using the TE method are believed to be more accurate for certain reasons. Firstly, the TE method includes contributions to the total energy from all k-points sampled in the Brillouin zone while in the SPE method uses the eigenvalue at the Γ -point only. The estimation would be more accurate and appropriate if instead of obtaining the eigenvalue at the Γ -point only, it was averaged over all the k-points by integrating it over a Monkhorst-Pack net. The assumption is that the dispersion of the eigenvalues will not change much upon relaxation. We can see in Fig. 5.12 and Fig. 5.13 that the dispersion does change in some cases with lattice relaxation. From these diagrams, the average error for using the Γ -point-only approximation was estimated to be 0.2 eV. This error is large enough and comparable to the standard errors we get from comparing the two methods.

Secondly, the TE values are in better agreement with other published results than the SPE values and also can account for some of the photoluminescence

experiment results previously explained by other first-principles studies. The advantage of using the SPE method is, the SPE method is simple and computationally much less expensive than the TE method. Only two SCF calculations with a defect in two charge states are sufficient to calculate the TL using SPE method, where, in TE method, two bulk supercells of equal dimension containing the same amount of charges with the defect supercell are also needed to be computed. Thus the computational expense in the TE method is double of that in the SPE method. Moreover, calculating charged bulk supercells requires large k-point grids as they are metallic systems and difficult to converge, especially when using a hybrid functional.

From the above discussions, we can draw the conclusion that for an accurate estimation of transition energy $\epsilon(q'/q)$, the supercells must be fully relaxed in their respective charge states. However, in a rapid electron-exchanging system such as optical recombination, both the total energies of the system in q and q' charge states should have the initial charge state (q) geometry. This is applicable in the estimation of optical transition energies.

6.3 Calculation of Hubbard U

The Hubbard- U is the Coulomb repulsive energy cost to add an electron to an already half-filled defect level and can be calculated from the difference in transition levels $\epsilon(2 - /-)$ and $\epsilon(-/0)$.

$$U = \epsilon(2 - /-) - \epsilon(-/0) \tag{6.5}$$

Using this equation, U values for the three intrinsic defects V_O , V_{Zn} and V_{ZnO} are obtained from the transition level values shown in Table 6.4. The U values are tabulated in Table 6.5 for both relaxed and unrelaxed crystal structures.

In Table 6.5 one can see that all three defects are positive- U with large U -values when the crystal structures are unrelaxed but as the structure is relaxed all three vacancies become negative- U or zero- U (for V_{Zn}). The value of U for V_O is -0.8 eV in comparison to -1.3 eV calculated using LDA by Lany and Zunger [69]. However, in a rapid electron-exchange system, where the electrons

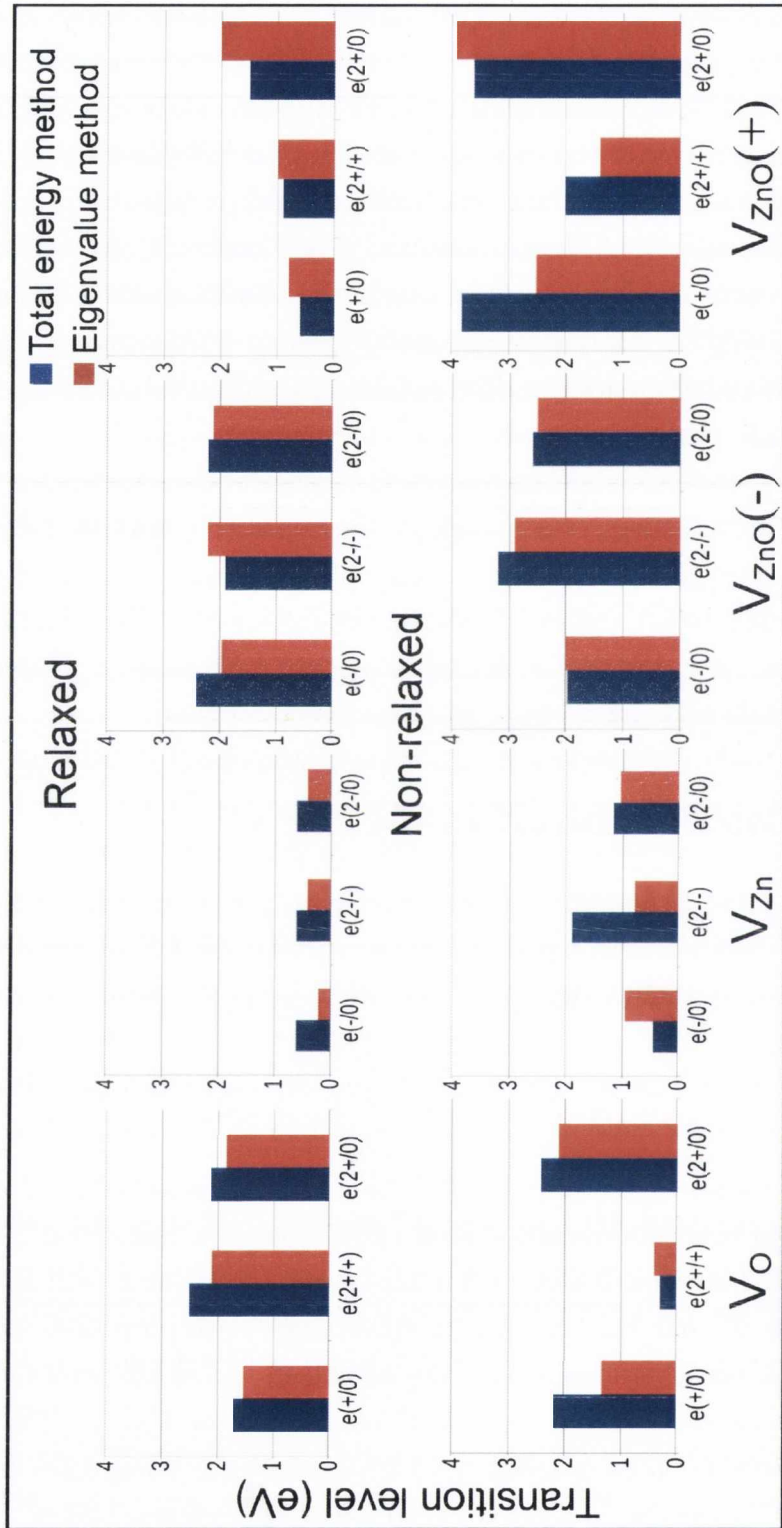


Figure 6.4: Comparison of transition levels obtained from total energy and single particle eigenvalue methods.

Table 6.5: Hubbard-U values in eV for defects.

Defect	TE method		SPE method	
	Relaxed	Non-relaxed	Relaxed	Non-relaxed
V_O	-0.8	1.9	-0.6	-0.9
V_{Zn}	0.0	1.5	0.2	-0.1
V_{ZnO}	-0.6	1.3	0.3	0.9

hop in and out of a vacancy faster than the lattice relaxation time ($\sim 10^{-12}$ s), the value of U may be recalculated using the relaxed crystal structure of 1- state of the respective defect for both 1- and 2- states, in a similar manner the optical transition energy was obtained (Eqn. 6.4). The value of U in such a case can simply be obtained by adding the relaxation energy $E'_{Rel}(2-/ -)$. Hence the value of U in a rapid electron exchange system, say U_{rees} for the three vacancies are from Table 6.5 and 6.2: $U_{rees}(V_O) = -0.8 + 0.8 = 0.0$ eV, $U_{rees}(V_{Zn}) = 0.0 + 0.4 = 0.4$ eV, and $U_{rees}(V_{ZnO}) = -0.6 + 0.8 = 0.2$ eV.

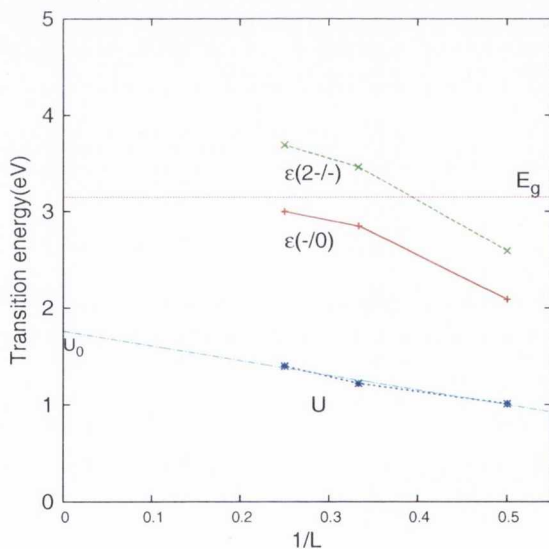


Figure 6.5: The transition energies $\epsilon(-/0)$ and $\epsilon(2 - / -)$ and the value of Hubbard-U for the V_{ZnO} defect with unrelaxed crystal structure. Values for different supercell sizes are plotted with respect to inverse of supercell size L . Value of the band gap E_g for infinitely large supercell ($L \rightarrow \infty$) is shown.

The electronic concentration changes with supercell size and thus changes the transition levels and U-value. We show in Fig. 6.5 that the U value slowly rises with supercell size and is linear with the inverse of the supercell-size L. This is because as the supercell gets larger the Coulomb interaction between the periodic images of the defect-trapped electron decreases and the on-site interaction dominates. The transition energies $\epsilon(-/0)$ and $\epsilon(2-/-)$ and the value of Hubbard-U for the V_{ZnO} defect are obtained using supercells of sizes $2 \times 2 \times 2$, $3 \times 3 \times 3$ and $4 \times 4 \times 4$. We discussed the Makov-Payne correction scheme [155] for the interaction of image charges due to the periodic boundary conditions of supercell methods in Chapter 4, which states that the energy contribution due to this interaction can be described by Eqn. 4.18. If we consider only the 1st term of Eqn. 4.18, the interaction energy between periodic images is inversely proportional to the supercell length L ($\Delta E \propto 1/L$). In this case L = 2, 3 and 4 for supercell sizes $2 \times 2 \times 2$, $3 \times 3 \times 3$ and $4 \times 4 \times 4$ respectively and the corresponding Hubbard-U values are plotted in Fig. 6.5. The U-value has been linearly extrapolated to infinite supercell-size ($1/L = 0$) and the value of U obtained, $U_0 = 1.8$ eV at $1/L = 0$. We can also see that the Hubbard-U value of 1.7 eV obtained for a $4\sqrt{3} \times 2\sqrt{3} \times 2$ supercell using total energies with different spin-configurations (see Chapter 7 for details) also fits with this extrapolation.

The supercells used for these calculations are all unrelaxed. When the crystal structure is relaxed with a charged supercell, the interactions between the periodic images of the charges are of different strength for different-sized supercells and the contribution to the transition level estimation are changed in a non-linear fashion. The true nature of the interaction between charges and their dependence on supercell size in this case can be derived statistically but needs more than just three different-sized supercells as used here. A practical obstacle in doing so is as the supercell-size becomes larger, the structure-relaxation calculation becomes extremely expensive. So a relationship between the energy contribution due to interaction between periodic images of charge during lattice structure relaxation was not possible by fitting the transition energy as a function of supercell-size in the current work and may be a subject for future work.

6.4 Conclusion

The results for the estimation of formation energies, transition levels and Hubbard- U of the intrinsic vacancy defects of ZnO were described in this chapter. Comparison has been made with other published results. The transition levels were calculated from two different methods, from the total energies of bulk and defected system and from the single-particle eigenvalue shift. A quantitative comparison between the results from the two methods shows that they roughly agree with each other but the deviation between the values is also considerable. The effect of lattice relaxation is discussed, which is substantial on defect charging. Estimation of U shows that none of the three vacancy defects are positive U once the geometry is relaxed. Hence none of these defects may act as a paramagnetic F-centre with a finite spin. A small positive U of 0.4 and 0.2 eV may occur for V_{Zn} and V_{ZnO} , respectively, if the electron exchange is faster than lattice relaxation time ($\sim 10^{-12}$ s).

In the next chapter we continue discussion on estimation of Hubbard U , but from the defect-defect interaction instead from a single defect. Also the defect-transition metal impurity interaction is explored by calculating the exchange coupling constants.

Chapter 7

Interaction of Defect-trapped Electrons, Transition Metal Doping

In the previous chapter we discussed the formation energies, transition levels and Hubbard - U values for intrinsic vacancy defects V_O , V_{Zn} and V_{ZnO} . A drastic effect of crystal structure relaxation is shown on defect charging. The value of Hubbard - U was calculated from the transition levels and a large reduction of the U -value was observed upon lattice relaxation.

In this chapter, we discuss defect-defect and defect - transition metal (TM) impurity interactions and consider any possibility of defect-related magnetism in intrinsic and TM-doped ZnO. We continue the discussion of Hubbard- U as a starting point, by estimating the U -value for V_{ZnO} from the interaction of two V_{ZnO} defects.

The Hubbard- U for V_{ZnO} is calculated here from the total energy difference of different defect level occupations where two V_{ZnO} defects are interacting in a partially filled system. To simulate the interaction between two defects, two V_{ZnO} defects were created, 11Å apart, in an unrelaxed $4\sqrt{3}\times 2\sqrt{3}\times 2$ supercell with 192 atoms. The total electron-trapping capacity of this system is then up to 4 electrons. At 1/4-filling, there is one electron to be shared between every two defects. The ground state was found to be a spin-polarised ($S=1/2$) state and the first excited state is unpolarised (spin 0). Note that only the second

term in the Hubbard Hamiltonian (Eqn. 2.13), $\frac{1}{2} \sum_i U n_{i\uparrow} n_{i\downarrow}$ is considered. In order to estimate the value of U , we need to obtain the energy expectation values of the second term of Eqn. 2.13 in a 1/4-filled system for both the polarised and unpolarised states. We can write the eigenfunctions for the polarised and unpolarised state in terms of Bloch wavefunctions. For an N -electron system, the wavefunction of a spin polarised state with one electron per two defects (1/4-filling) is given by,

$$\psi_{pol}(\mathbf{r}_1, \mathbf{r}_2, \dots, \mathbf{r}_N) = \frac{1}{\sqrt{N}} \prod_k^{k < k_{F,pol}} \phi_{\mathbf{k}\uparrow B}(\mathbf{r}_n) \quad (7.1)$$

$k_{F,pol}$ is the magnitude of the Fermi wavevector for the spin-polarised state which, in this case, is that of a single, fully occupied majority band. The minority band is empty. Spin orientation σ is indicated by \uparrow and \downarrow . B denotes a bonding state (A is used to denote anti-bonding states). We can define the wavefunction for the unpolarised state in a similar fashion,

$$\psi_{unpol}(\mathbf{r}_1, \mathbf{r}_2, \dots, \mathbf{r}_N) = \frac{1}{\sqrt{N}} \prod_k^{k < k_{F,unpol}} \phi_{\mathbf{k}\uparrow B}(\mathbf{r}_n) \phi_{\mathbf{k}\downarrow B}(\mathbf{r}_m) \quad (7.2)$$

The magnitude of $k_{F,unpol}$ in this case is that of a pair of half-filled bands, one for each spin-orientation. $\phi_{\mathbf{k}\sigma}(\mathbf{r})$ are Bloch wavefunctions, which are expanded in a pair of defect orbitals. For a single electron,

$$\phi_{\mathbf{k}\sigma B}(\mathbf{r}) = \frac{1}{\sqrt{2}} [\varphi_{i1}(\mathbf{r} - \mathbf{s}_1 - \mathbf{R}_i) + \varphi_{i2}(\mathbf{r} - \mathbf{s}_2 - \mathbf{R}_i)] e^{i\mathbf{k}\cdot\mathbf{R}_i} \chi(\sigma) \quad (7.3)$$

$\chi(\sigma)$ is an eigenspinor. $\phi_{\mathbf{k}\sigma B}(\mathbf{r})$ is a bonding combination of φ_{i1} and φ_{i2} , which are defect orbitals at sites \mathbf{s}_1 and \mathbf{s}_2 in the i th defect supercell.

The normalisation of these orbitals is,

$$\langle \varphi_{is} | \varphi_{jt} \rangle = \delta_{ij} \delta_{st} \quad (7.4)$$

so that the wavefunctions ψ_{pol} and ψ_{unpol} are normalised on a single supercell. Now we can obtain the matrix elements of either state for the second term of the Hubbard Hamiltonian $\hat{H}_1 = U \hat{n}_{i\uparrow} \hat{n}_{i\downarrow}$ (i labels a defect site). The matrix element

$\langle \psi_{pol} | \hat{H}_1 | \psi_{pol} \rangle$ is zero since there are no spin $\sigma = \downarrow$ electrons and operation of \hat{n}_\downarrow yields zero. The matrix element for the unpolarised state is,

$$\langle \psi_{unpol} | \hat{H}_1 | \psi_{unpol} \rangle = \frac{1}{N} \langle \phi_{\mathbf{k}\uparrow B}(\mathbf{r}_n) \phi_{\mathbf{k}\downarrow B}(\mathbf{r}_m) | \frac{1}{2} U \hat{n}_{is\uparrow} \hat{n}_{is\downarrow} | \phi_{\mathbf{k}\uparrow B}(\mathbf{r}_p) \phi_{\mathbf{k}\downarrow B}(\mathbf{r}_q) \rangle \quad (7.5)$$

By plugging in the expressions of $\phi(\mathbf{r})$ given in Eqn. 7.3, and applying the normalisation, we get factors $N/2$ from number of terms, $1/4$ from normalisation of orbitals φ and 2 for number of sites per cell. So the matrix element becomes,

$$\langle \psi_{unpol} | \hat{H}_1 | \psi_{unpol} \rangle = \frac{1}{N} \frac{U}{2} \frac{N}{2} \frac{1}{4} 2 = \frac{U}{8} \quad (7.6)$$

Therefore, the energy splitting between the two states is $U/8$. This can also be shown by calculating the charge population for each of the spin states. From Fig. 7.1, in the spin $1/2$ spin-polarised state, the populations of α and β spins on defects 1 and 2 are $n_{1\alpha} = n_{2\alpha} = 1/2$ and $n_{1\beta} = n_{2\beta} = 0$, giving an energy expectation value of $U(1/2 + 1/2)(0) = 0$. In the unpolarised state, the populations are $n_{1\alpha} = n_{2\alpha} = 1/4$ and $n_{1\beta} = n_{2\beta} = 1/4$, which yields an energy of $U(1/4)(1/4)(2) = U/8$ (the factor of 2 is for the number of sites). Hence the energy difference between the two states is $U/8$. From the supercell calculation with two defects and one electron, we have the energy difference of 147 meV between two states. Therefore $U = 147 \times 8 = 1176$ meV. For a half-filled system we have one electron per defect. This is a trivial case of Hubbard model where, for positive values of U , we get a Heisenberg antiferromagnet.

At $3/4$ -filling, there are three electrons per defect pair which can give a spin-polarised state or an unpolarised state. The spin-polarised state contains a filled bonding band of the form of Eqn. 7.3 and a majority spin band (Fig. 7.1). This new band is anti-bonding in character. Therefore,

$$\phi_{\mathbf{k}\sigma A}(\mathbf{r}) = \frac{1}{\sqrt{2}} [\varphi_{i1}(\mathbf{r} - \mathbf{s}_1 - \mathbf{R}_i) - \varphi_{i2}(\mathbf{r} - \mathbf{s}_2 - \mathbf{R}_i)] e^{i\mathbf{k} \cdot \mathbf{R}_i} \chi(\sigma) \quad (7.7)$$

This state is essentially degenerate with the state in Eqn. 7.3 because the hopping parameter t is small compared to U . The spin-polarised and unpolarised states for this case are given by,

$$\psi_{pol}(\mathbf{r}_1, \mathbf{r}_2, \dots, \mathbf{r}_{3N}) = \frac{1}{\sqrt{3N}} \prod_k^{k < k_{F,pol}} \phi_{\mathbf{k}\uparrow B}(\mathbf{r}_n) \phi_{\mathbf{k}\downarrow B}(\mathbf{r}_m) \phi_{\mathbf{k}\uparrow A}(\mathbf{r}_p) \quad (7.8)$$

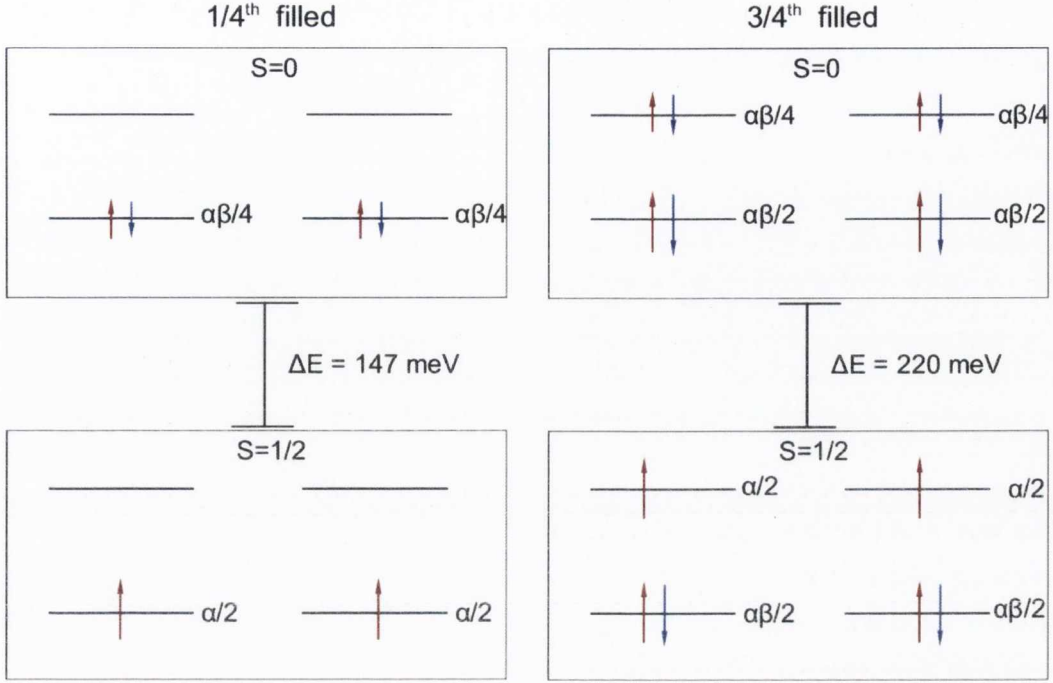


Figure 7.1: Estimation of U from different spin-population configurations of one (left) and three electrons (right) in two V_{ZnO} defects. Up and down arrows denote α and β spin populations. Length of the arrows vaguely depict population strength.

and

$$\psi_{unpol}(\mathbf{r}_1, \mathbf{r}_2, \dots, \mathbf{r}_{3N}) = \frac{1}{\sqrt{3^N}} \prod_{k < k_{F,unpol}} \phi_{\mathbf{k}\uparrow B}(\mathbf{r}_n) \phi_{\mathbf{k}\downarrow B}(\mathbf{r}_m) \phi_{\mathbf{k}\uparrow A}(\mathbf{r}_p) \phi_{\mathbf{k}\downarrow A}(\mathbf{r}_q) \quad (7.9)$$

In the unpolarised case, the Fermi level lies in the middle of the $\phi_{\mathbf{k}\sigma A}$ band. The matrix elements for the Hubbard- U term can be obtained from the charge population in the exactly same manner as previously done for 1/4-filling. From Fig. 7.1, we can see that in the spin 1/2 state, the populations of α and β spins are $n_{1\alpha} = n_{2\alpha} = 1/2 + 1/2 = 1$ (for both bands) and $n_{1\beta} = n_{2\beta} = 1/2$, therefore,

$$\langle \psi_{pol} | \hat{H}_1 | \psi_{pol} \rangle = U \left(\frac{1}{2} \right) (2) = U \quad (7.10)$$

For the unpolarised state, the populations are $n_{1\alpha} = n_{2\alpha} = 1/4 + 1/2 = 3/4$

and $n_{1\beta}=n_{2\beta}=1/4+1/2=3/4$, which yields

$$\langle \psi_{unpol} | \hat{H}_1 | \psi_{unpol} \rangle = U \left(\frac{3}{4}\right) \left(\frac{3}{4}\right) (2) = \frac{9U}{8}. \quad (7.11)$$

Hence the energy difference between the two states turns out to be $\frac{9}{8}U - U = \frac{1}{8}U$ again. From the supercell calculation we get the energy difference of 220 meV, yielding $U=1760$ meV.

At complete-filling, all states are filled and there is no spin-polarised state of the defect. The value of U determined for V_{ZnO} by this method (1.76 eV) is near to the value obtained from TE transition levels (Table 6.5) for unrelaxed supercells (1.2 eV) but overestimated. The reason behind the overestimation is that U is dependent on supercell-size and linearly decreases with increment of $1/L$, reciprocal of supercell size. This implies that the value of U increases with supercell size (Fig. 6.5). In the related discussion we will see that for a bigger supercell such as the one used in this calculation ($4\sqrt{3}\times 2\sqrt{3}\times 2$ which is almost double the size of $3\times 3\times 3$ that yields $U = 1.2$ eV) the value of U is quite nicely in agreement with the U -value estimated from the TE-transition level method.

Note that the above calculations are done with an unrelaxed $4\sqrt{3}\times 2\sqrt{3}\times 2$ supercell. The calculation to estimate the Hubbard- U of V_{ZnO} from total energies of different spin-configuration was repeated and the crystal structure of the supercells were fully relaxed with each spin configuration. The Hubbard- U from the energy difference of the relaxed supercell was -0.2 eV. This is in agreement with the data in Table 6.5 that the defect U -value turns negative when the crystal structure is relaxed. We have discussed in the previous chapter that for a rapid electron-exchange system, the Hubbard - U value for V_{Zn} and V_{ZnO} may be positive but the ratio U/t would not be large. The negative- U behaviour of V_{ZnO} is visualized in the wavefunction isosurface drawn using the relaxed structure shown in Fig. 7.2. We can see that the ground state represents one doubly occupied and one empty vacancy instead of two singly occupied vacancies. This signifies that a doubly occupied and an empty vacancy system is energetically preferable over a two-singly-occupied-vacancy system. This has been shown in the previous chapter from the estimation of U from the TE values that $U = \epsilon(2-/-) - \epsilon(-/0)$ is negative.

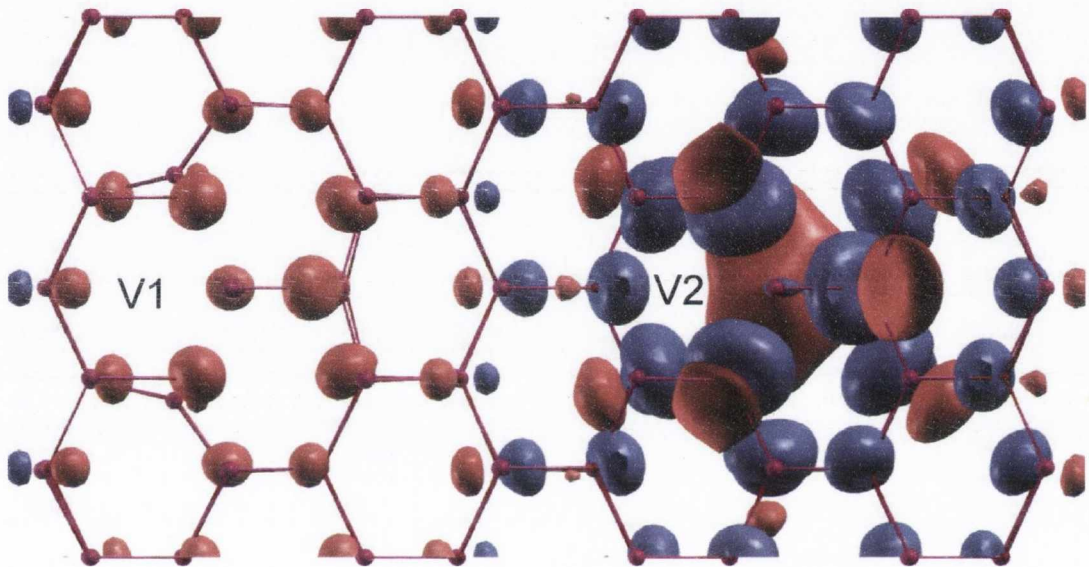


Figure 7.2: Wave function isosurface of V_{ZnO} defect-trapped electron in a $4\sqrt{3}\times 2\sqrt{3}\times 2$ supercell with two V_{ZnO} defects (marked V1 and V2) and two electrons in a relaxed crystal structure showing that in the ground state the two electrons reside on one vacancy and the other one remains empty. This implies a negative $-U$, otherwise, we should get both the defects half-filled (Heisenberg antiferromagnet).

The U -values for V_O and V_{ZnO} were not estimated using the interaction between defects as this method involves large supercells and is extremely expensive regarding computer-time, especially when full relaxation of crystal structure is involved.

7.0.1 Magnesium oxide (MgO)

MgO is one of the oxides that was observed showing room-temperature ferromagnetic order for thin films grown in low oxygen partial pressure [66]. This phenomenon was observed in thin films with high impurity levels and therefore the true origin of ferromagnetism may not only be the intrinsic defects. Khalid *et al* [170] have shown that for ZnO and MgO thin films with vacancies and impurities, the Curie temperature of an FM sample depends on accumulation of defects and impurities at surfaces and does not depend on the intrinsic ferromagnetic impurity content (TM:Fe or Co). EPR spectroscopy shows a large resonance signal for trapped electrons for off-stoichiometric thin films [170], which is very similar to that of ZnO which was discussed in Chapter 2. A surface calculation presented by Ricci *et al* [65] also suggested the possibility of anion-cation MgO divacancies as surface electron traps which act as paramagnetic centres. Calculations were carried out in this work in order to estimate the Hubbard- U for the MgO divacancy in bulk MgO. A $6 \times 6 \times 6$ supercell was constructed from the cubic MgO unit cell with lattice constant $a = 4.21 \text{ \AA}$ [56]. Two MgO divacancies and three extra electrons were created in this supercell and the energy difference ΔE was obtained between the spin-1/2 and the spin-0 metallic state. Following the exact same procedure used for ZnO, the Hubbard- U can be estimated to be $U = 8\Delta E$. The spin-1/2 state was found to be the ground state and for the unrelaxed $6 \times 6 \times 6$ supercell U was found to be 3.1 eV.

However the calculations were done with unrelaxed supercells and the relaxation calculation could not be performed because of the large size of the supercell. Since in earlier work the surface divacancies there found to be positive- U even when the crystal structure is relaxed [65], the question remains whether V_{MgO} in bulk remains positive- U upon lattice relaxation and may be the subject of future work.

7.1 Implication of Hubbard model of ferromagnetism

We have discussed the Hubbard model of ferromagnetism proposed by Nagaoka [122] in Chapter 2. The magnetic phase diagrams based on this model are obtained by several groups using different finite-temperature algorithms such as QMC [68], DMFT [124], SDA [123] and HTSE [67].

U values are the TE method numbers from Table 6.5 and the hopping parameter t for the three defect levels can be estimated from the band width W (obtained from the band-diagram shown in Fig 5.12). Hence, an attempt can be made to explain the defect-related ferromagnetism by comparing the value of U/t to published Hubbard-model phase diagrams and inquire whether they fall in the ferromagnetic phase. First we will see the results for the unrelaxed crystal structure. Each defect has 6 neighbours and therefore $t = W/6$. The t -values obtained for V_O , V_{Zn} and V_{ZnO} defects are 62 meV, 35 meV and 96 meV, respectively, for an unrelaxed $3 \times 3 \times 3$ supercell. Therefore, for V_{ZnO} we have $U/t \sim 25$. According to an HTSE calculation on Hubbard model [67], the Curie temperature of this system may fall in the range 800K - 1300K. However, in practice thin film defects are presumably separated by more than 11\AA , as used here. U will not depend strongly on defect separation but t will decrease rapidly. According to the phase diagrams for both ordered [68, 123, 124, 171] and disordered [125] lattices, reducing t to half ($= 34$ meV) will decrease the Curie temperature but the system may retain the parallel spin-alignment.

However, when the crystal structures are relaxed, Hubbard- U values for all three defects become negative (zero for V_{Zn}). We have discussed before that the crystal structure must be relaxed when a charged defect is present in order to calculate TL or U -values. Hence we conclude that in equilibrium, the intrinsic vacancy defects in ZnO (V_O , V_{Zn} and V_{ZnO}) have negative U (zero U for V_{Zn}) and can not take part in ferromagnetism described by the model based on the Hubbard model, discussed in Chapter 2. We have shown in the previous chapter that even in a rapid electron exchange system, we may have positive values of U , but these values are too small (0.0 eV, 0.4 eV and 0.2 eV for V_O , V_{Zn} and V_{ZnO} respectively) to satisfy the proposed model.

7.2 Interaction between defects and transition metal impurities

We have discussed in Chapters 1 and 2 that dilute amounts (4-7%) of transition metal (TM) ions doped in oxides such as ZnO, In₂O₃ etc were found to induce ferromagnetism in otherwise non-magnetic oxides [12, 13, 15]. Many experiments suggest a possible correlation between defects and ferromagnetism [15, 17]. Hence it is important to investigate the mechanism of interaction between the vacancy defects of ZnO and TM impurities. In this work, Co²⁺ ions are substituted for Zn²⁺ ions at all unique sites of the supercell close to a V_{ZnO}⁻ or V_{Zn}⁻ vacancy site. A 3×3×2 supercell with 72 atoms was used. Substitution of two Zn atoms with Co atoms is used to calculate the exchange constant between the two Co atoms. This gives a Co concentration $x \sim 5.5\%$ which is similar to the concentration used in most DMS related experiments. For all these Co²⁺ substitutions, calculations were performed with the Co²⁺ magnetic moment parallel and antiparallel to the vacancy-trapped spin. The energy difference between the parallel and antiparallel spin configurations of the Co²⁺ ion and defect-trapped electron give an estimate for the magnetic coupling energy of these two magnetic centres.

The occupied e_g levels that couple with the defect-spin in s-d exchange are separated from the empty t_{2g} levels by approximately 5 eV. This energy difference is underestimated in LSDA calculations [44, 59] and is thought to be slightly overestimated in the B3LYP calculation used here [36].

A list of the calculated values of coupling energies are given in Table 6.1. We can see that the interaction between the Co²⁺ ions and defect is strong when the Co²⁺ ion substitutes the Zn²⁺ ions nearest to the defect and then dies rapidly with separation between the Co²⁺ ion and the defect site. Strong coupling (> 10 meV) exists within a radius of 5 Å from the defect centre. The defect wavefunction is s-like (Fig. 5.10) and it overlaps with the Co²⁺ d-states and couples via a short range s – d exchange. However, the V_{ZnO}⁻ trapped electron wavefunction is not spherically symmetric (Fig. 5.10), causing the anomaly in a direct relationship between linear distance and coupling strength of a Co²⁺ ion and a trapped electron (Table 7.1). Calculations for coupling energy were also performed with

7.2 Interaction between defects and transition metal impurities

pairs of Co^{2+} ions in the absence of any vacancy defects to obtain the interaction between Co^{2+} ions. The coupling energy values are listed in Table 7.2. The interaction between the near-neighbour Co^{2+} ions are all antiferromagnetic as expected [59, 157]. This is a superexchange interaction and decays abruptly beyond nearest neighbours (Table 7.2). In Table 7.2 a comparison is made between coupling energies calculated in this work and by the LSDA+U method [172]. The values for near-neighbour Co^{2+} ions in the same basal plane and in adjacent planes are 12 and 0.1 meV, respectively. In comparison LSDA+U yields 16 and 6 meV, respectively [172].

Table 7.1: Total energy difference $\Delta E = E_{\uparrow\uparrow} - E_{\uparrow\downarrow}$ between a V_{ZnO}^- or V_{Zn}^- and a Co^{2+} ion substituted in various distance d from the vacancy site.

$d_{\text{Co}-V_{\text{ZnO}}^-}$ (Å)	$\Delta E_{\text{Co}V_{\text{ZnO}}^-}$ (meV)		$d_{\text{Co}-V_{\text{Zn}}^-}$ (Å)	$\Delta E_{\text{Co}V_{\text{Zn}}^-}$ (meV)	
	Non-relaxed	Relaxed		Non relaxed	Relaxed
1.98	394.00		3.26	-78.60	
3.25	4.66	18.88	3.30	0.42	
3.80	1.86		4.54	-4.24	
3.80	-6.40		5.16	-8.00	
4.59	14.80		5.59	2.18	
4.95	0.02		5.64	-1.22	
5.00	25.40	40.37	5.69	-8.00	
5.90	1.01		7.63	1.36	0.39
5.95	0.30		-	-	
6.50	1.54		-	-	
6.74	2.70	2.40	-	-	

When calculations were performed with pairs of Co^{2+} ions and a negatively charged defect, it was found that the coupling energy is a sum of the antiferromagnetic coupling energy between the Co^{2+} pairs and the individual coupling energies between each Co^{2+} ion with the defect spin. This can be summarised by the Ising Hamiltonian given by,

Table 7.2: AFM coupling between two Co^{2+} ions.

$d_{\text{Co-Co}}$ (Å)	ΔE_{CoCo}^1 (meV)	ΔE_{CoCo}^2 (meV)
3.20	12.2	16.0
4.57	0.10	6.0
5.61	0.58	
5.63	0.28	
7.66	0.02	

$$H^{\text{Ising}} = \sum_{i < j} J^{\text{Co}_i\text{V}} S_{\text{Co}_i}^z S_{\text{V}}^z + J^{\text{Co}_i\text{Co}_j} S_{\text{Co}_i}^z S_{\text{Co}_j}^z \quad (7.12)$$

where summation is made over pairs of spin centres: two Co^{2+} ions and a defect. $J^{\text{Co}_i\text{V}}$ and $J^{\text{Co}_i\text{Co}_j}$ are the coupling energies between Co^{2+} - vacancy electron and Co^{2+} - Co^{2+} ions, respectively. This equation was validated for V_{ZnO} and V_{Zn} vacancy defects. We can see from Table 7.1 that the interaction between negatively charged V_{ZnO} and V_{Zn} and Co^{2+} ions nearby are AFM and FM, respectively. The AFM interaction between V_{ZnO} and Co^{2+} ions is due to an $s - d$ exchange between the s -like defect wavefunction and the Co^{2+} $-3d$ orbitals. V_{Zn} , on the other hand, when negatively charged, the electron is localised on the neighbouring dangling O- $2p$ states. These states overlap with Co^{2+} $-3d$ levels at short range and the exchange is direct $p - d$ exchange, leading to a very short-range FM coupling. The difference between the wavefunctions of V_{ZnO} and V_{Zn} can be seen in Fig. 5.10.

Most calculations were performed using Co ions substituted at Zn sites with no lattice relaxation except for some particularly interesting configurations of Co^{2+} substitutions. The relaxation calculation is expensive and thus is not repeated for all Co^{2+} substitution configurations. The coupling energies between Co^{2+} ions and the defect-trapped spin with relaxed crystal structure for some of the Co^{2+} substitution configurations are given in Table 7.1. The relaxation energy and displacements for Co_{Zn} substitution are much smaller than that of

¹This work

²Ref. [172]

the vacancy defect creation. This is because of the small difference in the ionic radii of Co^{2+} and Zn^{2+} . As the defect and its surrounding atomic coordinates relax, the interaction between the Co^{2+} ion and the defect-spin becomes subtly stronger in close and mid ranges.

7.3 Conclusion

A study on defect-defect and defect-TM impurity interaction in ZnO host is described in this chapter. The value of Hubbard- U for the V_{ZnO} vacancy defect was estimated using a spin-configuration method. The value of U for both relaxed and unrelaxed supercells are in agreement with the values estimated in Chapter 6 using transition levels. Calculations with $\text{Zn}_{1-x}\text{Co}_x\text{O}$ ($x \sim 0.05$) show AFM interaction between Co^{2+} ion pairs when they are nearest neighbours. V_{ZnO}^- and V_{Zn}^- interact with a Co^{2+} ion via AFM and FM interactions, respectively, when the Co^{2+} ion is in the vicinity of the vacancy defect. In the case of V_{ZnO}^- , the range of the AFM defect- Co^{2+} interaction is larger than $\text{Co}^{2+} - \text{Co}^{2+}$ or $V_{\text{Zn}}^- - \text{Co}^{2+}$ interactions. This is because of the large s -like wavefunction associated with V_{ZnO}^- allows it to interact with a Co^{2+} ion via $s - d$ exchange in a range greater than the near-neighbour distance.

Chapter 8

Effect of Acceptor Doping in Magnetite Below Verwey Transition

Magnetite (Fe_3O_4) has the inverse spinel crystal structure [75]. At room temperature magnetite has cubic symmetry with space group $Fd\bar{3}m$. Fe_3O_4 undergoes a first order metal-insulator phase transition known as the Verwey transition [74, 173] at around 123K. Below the Verwey temperature, T_V , the cubic symmetry distorts, resulting in reduction of symmetry to a monoclinic phase with space group Cc . High resolution X-ray [77, 174] and neutron diffraction [73, 77], along with muon spectroscopy [76] and resonant soft X-ray scattering [175] experiments report evidence of charge order in the low temperature phase. The charge and magnetic order in the spinel ferrite magnetite is expressed as $\text{Fe}_{A1}^{3+}[\text{Fe}^{2+}\text{Fe}^{3+}]_{B1}\text{O}_4$ in the Verwey model [74]. The Verwey transition results in lattice site displacements of up to 0.07 Å [73] according to X-Ray Diffraction (XRD) experiments which reduces the symmetry from a higher cubic symmetry to a lower monoclinic one. However, it was found that a smaller $P2/c$ unit cell than the full Cc cell could account for all diffraction peaks characteristic of the Cc cell [73]. The dimension of the $P2/c$ cell is $a_c/\sqrt{2} \times a_c/\sqrt{2} \times 2a_c$, where a_c ($=8.394\text{Å}$ [73]) is the lattice parameter of the cubic $Fd\bar{3}m$ phase. The $P2/c$ cell is shown in Fig. 8.1. Like most of the mixed valence oxides the Fe^{2+} - Fe^{3+} mixed valence ions are stacked in tetrahedral and octahedral environments. Incomplete cancellation

of the B site magnetic moments by antiparallel A site cation moments results in ferrimagnetism. The total experimental ferromagnetic moment per unit formula is $4.07 \mu_B$ at room temperature [176] which is close to the theoretical value of $4.00 \mu_B$.

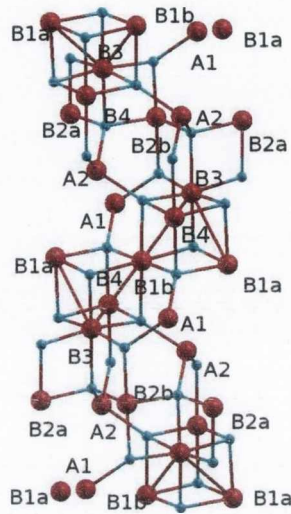


Figure 8.1: Crystal structure of magnetite in the $P2/c$ cell below the Verwey transition temperature. Different iron sites are labelled.

The electrical conductivity drops by two orders of magnitude below the Verwey temperature [73, 177] and an optical band gap of 0.14 eV opens up [177]. Interestingly, there is little conductivity below the Verwey transition, which is believed to arise from the hopping of charge carriers in Fe^{2+} - Fe^{3+} charge-ordered system [77, 78, 174, 175].

Some recent experiments on conductivity below the Verwey transition show sharp switching behaviour in the $I - V$ characteristic curve of nano-crystalline Fe_3O_4 samples [178]. A linear increase is observed in the switching voltage as the temperature goes below the Verwey temperature. A steadily increasing threshold energy for electron excitation as the temperature goes down suggests existence of an energy barrier associated with a small polaron hopping transport mechanism. The hopping mechanism is rather complicated and involves the electron phonon interaction [179, 180] and thus cannot be interpreted directly from a band structure calculation. Since the hopping levels are hybridized O-2p and $\text{Fe}^{2+}/\text{Fe}^{3+}$ -

3d [175] clustering at the top of the valence band, manipulation of these levels with substitutional impurities can shed light on the nature of electron-phonon coupling and transport associated with small-polaron hopping. Doping with acceptor agents may oxidise Fe_B^{2+} ions to Fe_B^{3+} , subsequently removing the hopping levels from the top of the valence band. This process strongly depends on the substitution sites and simulations were performed to seek out the most probable choice based on minimum total energy and convergence of DFT potential upon different site substitutions.

In a recent publication Rowan *et al* [137] have shown that B3LYP calculations on the monoclinic insulating magnetite were able to reproduce the charge order observed in experiments [73, 76, 175]. The lattice and electronic structure as well as the vibrational spectrum of pure magnetite was studied [137, 181] using the B3LYP hybrid DFT. This method has been proven quite effective in comparison to the experimental results available [73, 77, 177]. However, the band gap (= 0.9 eV) using B3LYP with the standard Hartree-Fock (HF) exchange parameter of 0.2 (Eqn. 3.15) is still overestimated over the experimental value of 0.14 eV [177]. As we already know from the discussion in Chapter 3 that the HF exchange overestimates the band gap, using a lower fraction of HF exchange in the exchange-correlation potential described in Eqn. 3.15 may reduce the band gap nearer to the experimental result. In this work, the HF parameter was fixed to 0.15 which yields a band gap of 0.4 eV for pure magnetite which is closer to the experimental value. This HF parameter was used for all calculations described here. The total density of states (DOS) of magnetite calculated with HF exchange parameter of 0.15 is shown in Fig. 8.2 compared with the DOS calculated with HF exchange parameter of standard 0.2. Fig. 8.3 depicts the electronic band structure of the pure magnetite calculated using HF exchange parameter of 0.15. The Fe^{2+} bands that create the VBM have been shown. Tuning the B3LYP parameter to correct the band gap only may lead to incorrect predictions of some other parameters such as lattice parameters and magnetic exchange coupling constants. However, lattice relaxation calculations reveal that turning down the HF exchange fraction does not change the lattice parameters and bondlengths more than 0.01 Å (Lattice parameters are in better agreement with experiment when $A=0.15$ is used). The changes in $\text{Fe}_A\text{-Fe}_B$ AFM exchange constants are of

the order of ~ 0.05 eV. Turning the HF exchange parameter below 0.15 reduces lattice parameters drastically and the convergence of the SCF calculation becomes difficult to achieve.

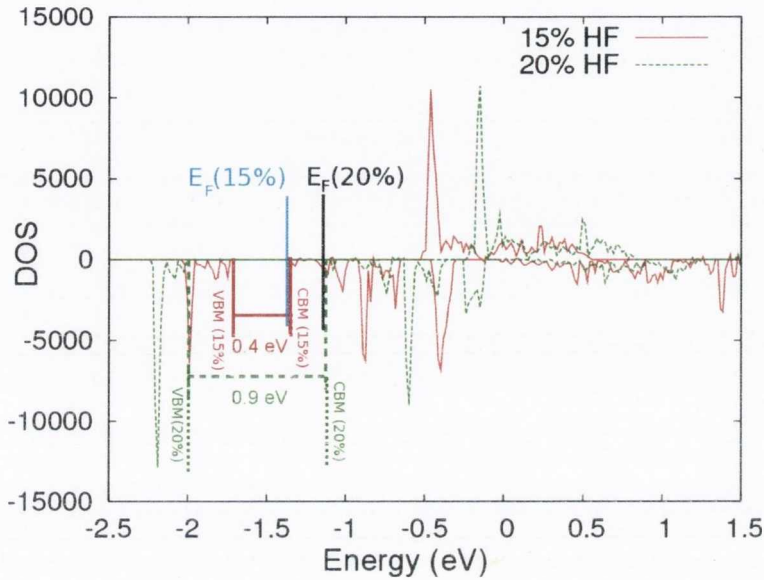


Figure 8.2: Density of states of Fe₃O₄ with HF exchange parameters 20% and 15%. Respective band gaps and Fermi levels are also shown.

8.1 Acceptor doped magnetite

We have discussed previously that doping with acceptor impurities oxidises the Fe_B²⁺ ions to Fe_B³⁺ and reduce the mixed-valence hopping. Depending on the impurity concentration, a control over the mixed-valence hopping can be exerted. In this work, electronic structure calculations were carried out with lithium (Li) and nitrogen (N) substituting the Fe and oxygen sites, respectively. Different substitution sites were tested to find out which site would be energetically favourable for substitution.

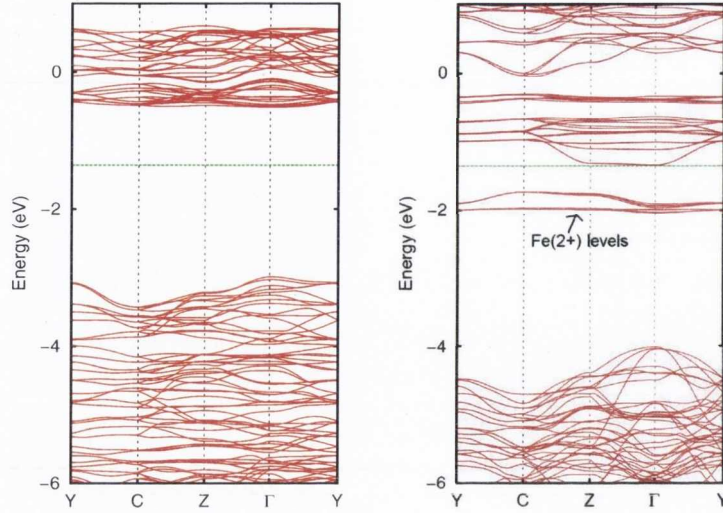


Figure 8.3: Majority and minority band structure of Fe_3O_4 with HF exchange parameter of 0.15. Dashed green line marks the fermi level.

8.1.1 Lithium ferrite: $\text{Li}_{0.5}\text{Fe}_{2.5}\text{O}_4$ and $\text{Li}_{0.625}\text{Fe}_{2.375}\text{O}_4$

A number of experiments observed that substituting Fe by lithium in magnetite does not change its crystal structure by a large amount [79, 182]. In Lithium ferrite ($\text{Li}_{0.5}\text{Fe}_{2.5}\text{O}_4$) all of the Fe^{2+} are oxidised to Fe^{3+} and the mixed-valence hopping is expected to be terminated. This causes opening up of a large band-gap. Hall effect measurements show that the conduction is normally n-type at room temperature [79]. However, one experimental study on off-stoichiometric $\text{Li}_{0.5}\text{Fe}_{2.5}\text{O}_4$ with a large concentration of oxygen vacancies showed that limited p-type conduction can be observed below T_V [79]. The magnetization in $\text{Li}_{0.5}\text{Fe}_{2.5}\text{O}_4$ is $2.5 \mu_B$ per unit formula (per $\text{Li}_{0.5}\text{Fe}_{2.5}\text{O}_4$) theoretically but is found to be as high as $3.0 \mu_B$ in experiment [79]. The A and B iron sites are antiparallel to each other but due to the fact that the A sites are only one-third of the Fe atoms, Fe_3O_4 has a finite ferrimagnetic moment.

Since the magnetic moment is reduced in $\text{Li}_{0.5}\text{Fe}_{2.5}\text{O}_4$, it is assumed that the A-site Fe_A^{3+} ions are not substituted. Different B-site iron ions were substituted by Li ions to find out the energetically favourable substitution. Total energy calculations reveal that substitution by Li^+ ions on a $\text{Fe}_{B4}^{2+}\text{-Fe}_{B3}^{3+}$ chain is most

8.1 Acceptor doped magnetite

favourable (See Fig. 8.1). The ground state is 0.8 eV deeper than substitutions on a $\text{Fe}_{B1}^{2+}\text{-Fe}_{B2}^{3+}$ chain. The difference in the total energies for different substitution sites are shown in Table. 8.1. Since Li substitution on the B4 sites corresponds to the lowest ground state among all different substitution, the energy difference is shown with respect to the substitution on B4 sites.

Table 8.1: Total energy differences between B4 and other iron sites substituted by Li. $\Delta(BX) = E_{Tot}(BX) - E_{Tot}(B4)$, $X = 1, 2, 3$. All values are in eV. The maximum changes in bond lengths upon substitution ($\Delta(\text{Bondlength})_{max}$) and band gaps are also shown for different site substitutions.

	B1	B2	B3	B4
$\Delta(BX)$ (eV)	0.8	1.1	0.3	0.0
$\Delta(\text{Bondlength})_{max}$ (Å)	0.08	0.11	0.15	0.03
Band gap (eV)	2.44	2.31	2.55	2.55

One of the reasons behind B4 site substitution having the lowest ground state is that the B4 sites have the largest bond lengths and can be easily substituted by a large Li^+ ion. Lattice relaxation calculations also suggest that Li substitution on the B3 site results in large changes in bond lengths with a maximum of 0.15 Å, about 7.5%. In the case of a B4 site substitution, the maximum bond-length change is 0.03 Å.

The total spin density of Li-ferrite with B4 site substitution is shown in Fig. 8.4 viewed along the c -axis. The spin density of pure magnetite is also shown for comparison. We can see that the oxygen atoms neighbouring to the Li atoms are pushed further from the Li atoms. Also the orientation of the Fe-3d orbitals signifies that in $\text{Li}_{0.5}\text{Fe}_{2.5}\text{O}_4$ the highest filled level in the energy spectrum is represented by a different Fe-3d level than that of Fe_3O_4 . This is because of the removal of the Fe_{B1}^{2+} levels from the VBM. The VBM in $\text{Li}_{0.5}\text{Fe}_{2.5}\text{O}_4$ consists of the dispersive Fe_{A1}^{3+} levels (Fig. 8.5).

Over-doping of Li in Li-ferrite generates extra holes in the system. Below T_V the holes are either bound to the charge order or may trigger p-type conduction. This was simulated by adding one extra lithium ion per $\text{Li}_{0.5}\text{Fe}_{2.5}\text{O}_4$ supercell to change the configuration to $\text{Li}_{0.625}\text{Fe}_{2.375}\text{O}_4$. This system has two extra holes

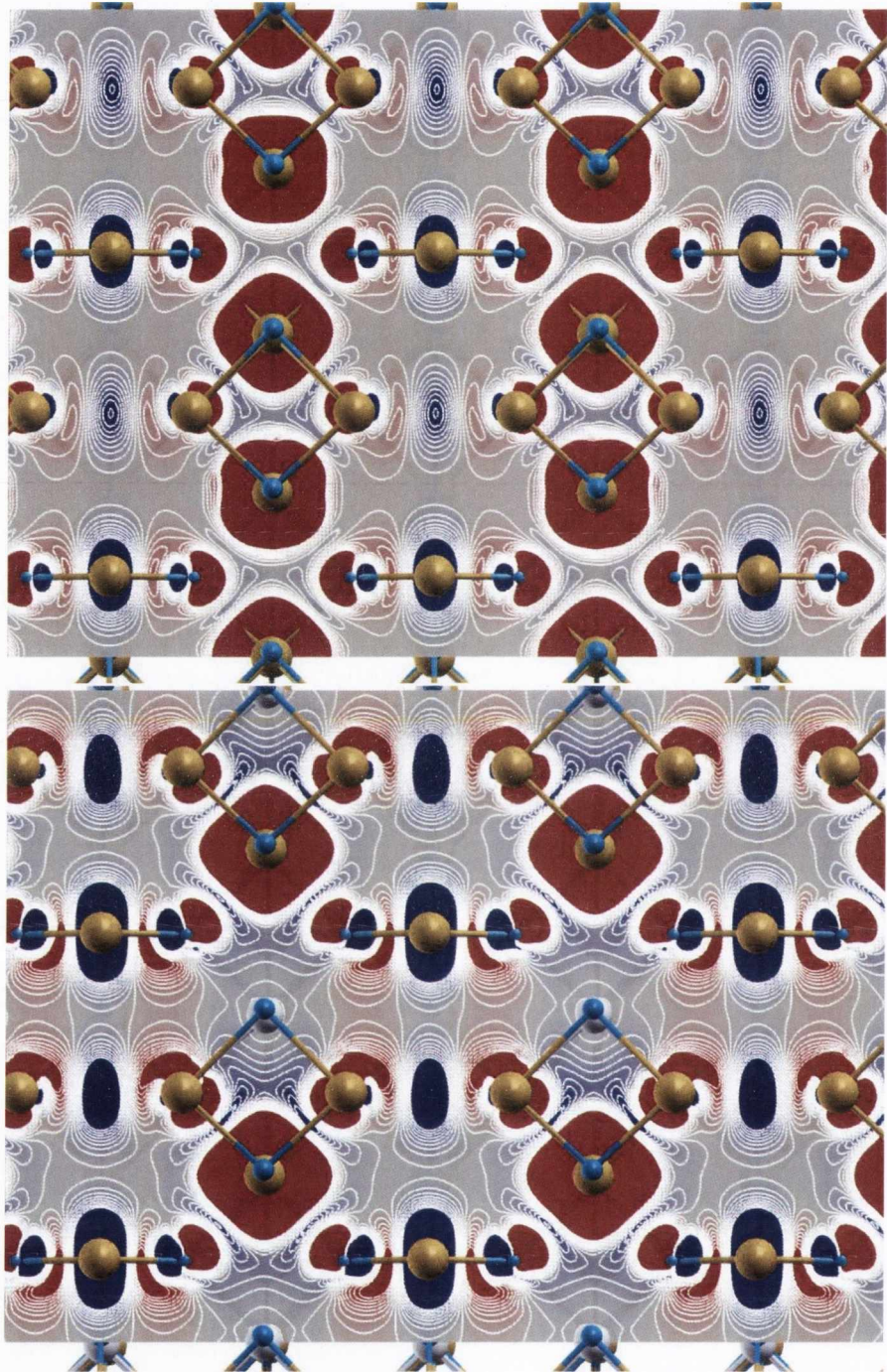


Figure 8.4: Spin densities of pure magnetite (top) and lithium ferrite (bottom). Gold, cyan and silver spheres denote Fe, O and Li atoms, respectively. Note that the iron d -orbital-orientation has changed in $\text{Li}_{0.5}\text{Fe}_{2.5}\text{O}_4$.

which are associated with deep empty levels in majority spin. The band structure of $\text{Li}_{0.625}\text{Fe}_{2.375}\text{O}_4$ is shown in Fig. 8.5, compared with that of $\text{Li}_{0.5}\text{Fe}_{2.5}\text{O}_4$.

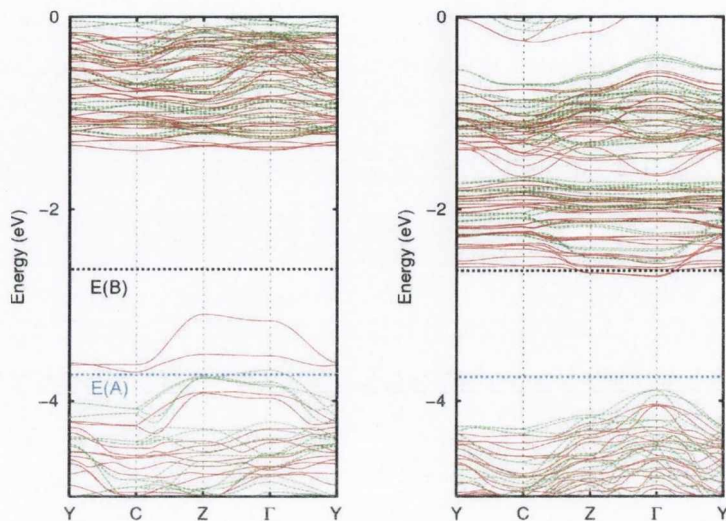


Figure 8.5: Majority and minority band structure of $\text{Li}_{0.625}\text{Fe}_{2.375}\text{O}_4$ (red) superposed on conventional lithium ferrite ($\text{Li}_{0.5}\text{Fe}_{2.5}\text{O}_4$) (green). E(A) and E(B) denote the Fermi levels for $\text{Li}_{0.625}\text{Fe}_{2.375}\text{O}_4$ and $\text{Li}_{0.5}\text{Fe}_{2.5}\text{O}_4$, respectively

The spin density of $\text{Li}_{0.625}\text{Fe}_{2.375}\text{O}_4$ along the ca plane (viewed along the b -axis) is shown in Fig. 8.6. We can see that the deep hole levels in Fig. 8.5 are associated with localized oxygen 2p orbitals neighbouring the B3 site where the extra Li atom was implanted. These localised holes form a bound polaron. Formation of polarons in hole-doped magnetite was predicted in earlier works [137] also.

8.1.2 Nitrogen substituted magnetite $\text{Fe}_3\text{O}_{3.5}\text{N}_{0.5}$

The effect of nitrogen substitution in oxygen sites (N_O) was tested in this work. Nitrogen acts as an acceptor agent by oxidising the Fe^{2+} ions. When all oxygen atoms in symmetric sites were substituted by nitrogen atoms, we have $\text{Fe}_3\text{O}_{3.5}\text{N}_{0.5}$. These symmetric sites can be denoted as A1', A2', B1', B2', B3' and B4', named after the neighbouring Fe site designation. In practice, preparation of $\text{Fe}_3\text{O}_{3.5}\text{N}_{0.5}$ in a single crystallographic phase is yet not achieved in experiments but research is

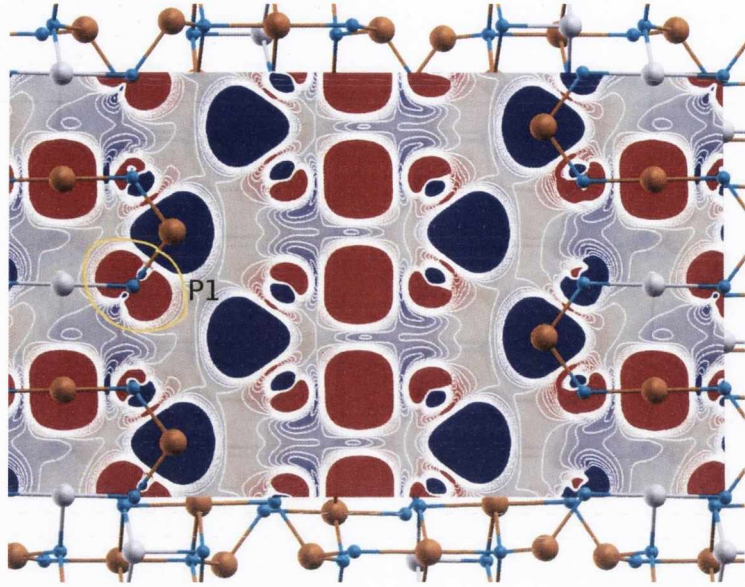


Figure 8.6: Spin density of $\text{Li}_{0.625}\text{Fe}_{2.375}\text{O}_4$ viewed along the b -axis. The polaronic holes localised in an oxygen $2p$ -like orbital is shown as P1. The colour scheme is same as Fig. 8.4.

in progress [183]. Substitution of $B3'$ O-sites (next to Fe_{B3}) are found energetically most favourable. The total energy of this substitution is lower than $B1'$, $B2'$ and $B4'$ sites by 1.1, 1.3 and 0.4 eV, respectively. Therefore the electronic band diagram and geometry optimization calculations were carried out with $\text{Fe}_3\text{O}_{3.5}\text{N}_{0.5}$ for only $B3'$ O-sites substituted by N. The lone electron of nitrogen oxidises the Fe_{B4}^{2+} ions to Fe_{B4}^{3+} . Unlike $\text{Li}_{0.5}\text{Fe}_{2.5}\text{O}_4$, in $\text{Fe}_3\text{O}_{3.5}\text{N}_{0.5}$ the Fe^{2+} ions are partially oxidised and Fe ions on the $B1$ sites remain in the $2+$ state. Therefore the band gap is almost the same as in pure magnetite. Interestingly, although the N_O levels are filled, there is a large magnetic moment of $0.32 \mu_B$ per N_O . The ferrimagnetic moment magnitudes are reordered. The $B3'$ sites neighbour the antiferromagnetic Fe A2 sites (Fig. 8.1) and increase the electronic density in the A2- $B3'$ bond. This results in reduction of magnetic moments of Fe A2 ions, increasing the total ferrimagnetic moment to $5\mu_B$ /unit formula (for pure magnetite the moment is $4\mu_B$ /unit formula).

The electronic band structure of $\text{Fe}_3\text{O}_{3.5}\text{N}_{0.5}$ with $B3'$ O-sites substituted is shown in Fig. 8.7. The N_O levels are coupled with Fe_{B2}^{3+} levels at the top of the

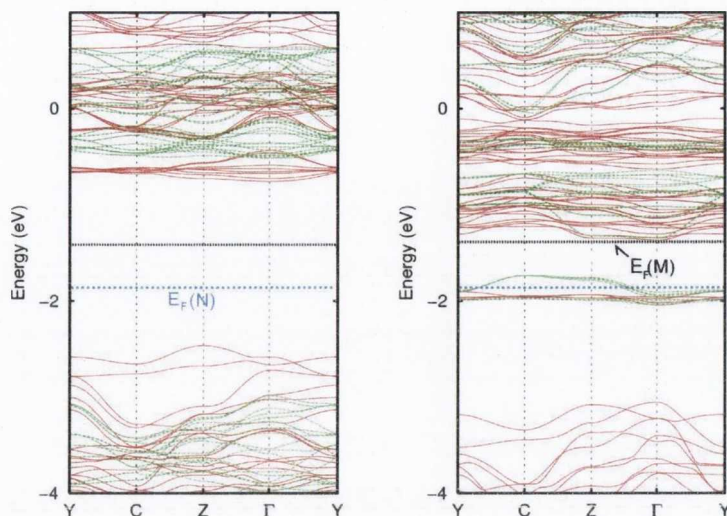


Figure 8.7: Majority(left) and Minority band structures of $\text{Fe}_3\text{O}_{3.5}\text{N}_{0.5}$ (solid/red) superposed on those of pure magnetite (green/dashed). Fermi levels are shown by $E_F(\text{N})$ and $E_F(\text{M})$ for $\text{Fe}_3\text{O}_{3.5}\text{N}_{0.5}$ and Fe_3O_4 , respectively.

valence band (Fig. 8.7) that governs the transitions since the $\text{Fe}_B^{2+}\text{-Fe}_B^{3+}$ hopping is partially terminated by the oxidation of Fe_{B4}^{2+} . Deeper levels from Fe-B site minority electrons rise up in the vicinity of the Γ -point while the corresponding empty bands become degenerate.

8.2 Conclusion

From the calculations carried out on Li and N impurity doping in Fe_3O_4 below the Verwey transition, we can predict that depending on the doping concentration, a manipulation over the mixed-valence hopping conduction and magnetic moments can be achieved. Formation of small polarons by hole doping is predicted. The energy needed for small polaron hopping in the charge-ordered structure may be calculated by inserting a hole in different oxygen sites of either a B1'-B2' chain or a B3'-B4' chain. This may be the subject of future work.

Chapter 9

Conclusions

In this work, the crystal and electronic structures of intrinsic vacancy defects and certain impurities in oxides ZnO and Fe₃O₄ have been studied using first principles calculations. Total energy and electronic structure calculations were done on the Zn cation vacancy (V_{Zn}), O anion vacancy (V_O) and the ZnO pair vacancy (V_{ZnO}). B3LYP hybrid DFT was found in the literature to be accurate and appropriate for these wide-gap oxides in many other studies and was used in this work. V_{ZnO}^- and V_O^+ exhibit a deep dispersive band by trapping electrons in an s-like wavefunction above the valence band maximum while V_{Zn} traps one to two electrons in dangling O-2p states with a flat band. The trapped electron state in V_{ZnO}^- was found to be capable of interacting at a range exceeding 10Å. At a partial band filling, more than half-filling, the defect-trapped electrons couple in a parallel spin alignment when a positive Hubbard- U is associated with the defect. From this observation, an attempt is made here to explain the defect-related ferromagnetism observed in ZnO and other oxide semiconductors.

Defects are sometimes thought to have a correlation with the ferromagnetism observed in dilute magnetic semiconductors (DMS). Transition metal (TM) ion doping in ZnO was tested by substituting Zn²⁺ by Co²⁺ ions and the interactions between defects and TM ions are investigated. Co²⁺ ions interact with the defect-trapped spin in V_{ZnO} via short-range AFM $s-d$ exchange while the interaction between V_{Zn}^- and Co²⁺ ions were found to be ferromagnetic and limited to the nearest neighbour range. Co²⁺ ions in ZnO mutually interact via AFM superexchange interaction when substituted as nearest neighbours.

In order to estimate the Hubbard- U of the defects and to justify the stability of the defects in different charge occupancies, formation energies and transition levels of each intrinsic vacancy defect in every possible charge-state were estimated. The estimations were done using both relaxed and unrelaxed (ideal) crystal geometries. Relaxation of crystal structure makes a large difference to the total energy of a defect system. This is because the system has to be restored to equilibrium for each different charge state. Thus the formation energies and the transition levels must be calculated with relaxed crystal structures for each respective defect/charge-state.

Some experiments observed a correlation between the concentration of different vacancy defects and anomalous (green / yellow / blue) photoluminescence in ZnO (normally UV-band gap). To verify the role of electron-trapping intrinsic vacancy defects in this phenomenon, estimation of optical transition levels between different defect charge-states was carried out from the transition levels. These calculations need special attention regarding relaxation because one has to consider the fact that the optical recombination process is three orders of magnitude faster than the crystal relaxation and thus the relevant crystal structure must be used for the estimation of optical transition energies, which is different from the transition levels in equilibrium. A number of first-principles calculations have been done in the past to explain the experimental observation of anomalous photoluminescence in off-stoichiometric ZnO thin films. In the current work, alongside of verification of the previous results, predictions were made on the role of complex pair vacancy in optical processes.

Transition levels were calculated using two different methods; from total energies of the two states involved in a transition and from the eigenvalues of those states using Janak's theorem. The two methods return results in rough agreement with each other. The deviations of the transition level values between the two methods were calculated. The standard (root-mean-square) and mean deviations for the unrelaxed values were found to be almost double that for relaxed values. A notable fact is that the deviations are much larger than the difference between the optical transition energies corresponding to two different photoluminescence colours. Therefore a high level of precision and accuracy is needed if predictions

are intended on the photoluminescence colour, based on the transition levels of the F-centres.

Finally, Hubbard- U values for the three intrinsic vacancy defects V_O , V_{Zn} and V_{ZnO} were calculated from the transition levels for both relaxed and unrelaxed geometries. The defects have a large positive U when the crystal structure is unrelaxed but as the relaxation takes place U becomes negative (zero for V_{Zn}). Therefore, they cannot act as paramagnetic centres and according to the model of ferromagnetism proposed here, these defects may not take part in room temperature ferromagnetism of ZnO thin films. However, in a rapid electron-exchange system where the defect occupation changes faster than the crystal relaxation, Hubbard- U may be positive, but too small to predict Ferromagnetic alignment of defect-trapped spins according to the Hubbard model.

Hubbard- U for the MgO pair vacancy (V_{MgO}) was also estimated and a large U was found for unrelaxed crystal structure. The relaxation is expensive and was not carried out.

First principles electronic structure calculations were used to study acceptor doped Fe_3O_4 (magnetite) below the Verwey transition. The electronic structure of lithium ferrite was investigated with different site substitution and found to be insulating below the Verwey transition, preserving a strong magnetic moment. Over-doping with Li produces localized small polaron states but more studies are required in order to predict possibilities of magnetic interaction and electrical conductivity mediated by small polaron hopping. Nitrogen substitution for oxygen leads to partial cancellation of mixed valence hopping, widening magnetite band-gap and increasing FM moment of magnetite.

9.1 Future Work

The analysis of the results and discussion following have raised many questions. A source of paramagnetism was not found in the intrinsic vacancy defects of ZnO. It also remained unresolved whether the Hubbard model can be applied to the defect-related ferromagnetism of oxides such as MgO.

The two different methods used to estimate the transition levels do not give identical results and the current framework of the single-particle eigenvalue (SPE)

method is believed not to be as accurate as the total energy (TE) method. The SPE method can be corrected by summing over the eigenvalues over all k-points instead of using the Γ -point only approximation. Hence the optical recombination energies can be more correctly predicted and comparisons can be made with photoluminescence experiment results.

EPR /ODEPR experiments are very helpful in characterising defects in oxide semiconductors but cannot be directly compared with first-principles calculation results. A simulation code to calculate the EPR g-tensor may be useful here. The Quantum Espresso plane-wave code [150] has been developed for the calculation of g-tensor using the gauge-included projector-augmented wave method (GIPAW) [184] but can not calculate the g-tensor for wide-gap oxides accurately. Development of a GIPAW algorithm, based on a localized orbital basis code, so that hybrid DFT calculations may be carried out, will be greatly beneficial in understanding the nature of electron-trapping defects in wide-gap oxides.

Copper aluminate (CuAlO_2) is a transparent *p*-type semiconductor with a direct band gap close to ZnO (3.5 eV [185]). This material has the potential to be a *p*-type counterpart of ZnO in a *p*–*n* junction optical device. It would be useful to investigate whether the methods used for ZnO to calculate defect transition levels are also applicable in CuAlO_2 , and therefore establishing a generalisation of these methods.

The possibility of formation of small polarons in magnetite below the Verwey transition temperature by hole doping has been predicted in this work. The possibility of electrical transport by small-polaron hopping or magnetic exchange between the polarons are yet to be calculated. The activation barrier potential for the small polaron hopping can be calculated by inserting a hole in different oxygen sites and by minimising the total energy of the lattice and the electronic system with the hole in those different sites. Hence the results from vibrational spectrum calculation can be used to identify the phonon modes responsible for small polaron hopping.

Appendix A

Details of Calculations

B3LYP hybrid DFT in the CRYSTAL simulation package [147] was used for most of the calculations in this work. Quantum Espresso [150] was used for some calculations to compare results obtained using a plane-wave code as CRYSTAL is a Gaussian-orbital code. CRYSTAL can be used to perform DFT calculations using a number of different functionals such as LDA, LDA+U, GGA, GGA+U, Hartree-Fock and B3LYP hybrid DFT. In this work B3LYP Hybrid DFT with constant Hartree-Fock weight factor of 0.2 (See Eqn. 3.15) was used. For Fe_3O_4 with the low temperature distorted-inverse-spinel structure, Hartree-Fock weighting of 0.15 was used as it gives better agreement with the experimental band gap. Supercells of different sizes were used, designated for different purposes and are described in the following.

The lattice parameters were predicted using B3LYP hybrid DFT. Starting with a unit cell with lattice parameters derived from X-ray diffraction experiment results, the crystal structure was relaxed using B3LYP hybrid DFT until the total energy was minimised with respect to a tolerance of 10^{-4} Å of lattice displacement. For ZnO, the calculated lattice parameters of the wurtzite primitive crystal cell are $a = b = 3.28$ Å, $c = 5.27$, $\alpha = \beta = 90^\circ$, $\gamma = 120^\circ$ compared to experimental values with which the calculation was started, $a = b = 3.25$, $c = 5.21$ Å, $\alpha = \beta = 90^\circ$, $\gamma = 120^\circ$ [56]. Note that B3LYP overestimates the lattice parameters, but they are not far from the experimental results.

From this basic unit cell of ZnO, a number of different supercells were generated for different purposes. For the band-structure calculation and to test the

effect of transition metal doping, a monoclinic supercell was used with dimension $3 \times 3 \times 2$ (72 atoms), with space group Cm(8). Monoclinic $2\sqrt{3} \times 2\sqrt{3} \times 2$ supercell with 96 atoms and a $4\sqrt{3} \times 2\sqrt{3} \times 2$ supercell with 192 atoms are used to calculate Hubbard U and defect-defect interaction in long range. These supercells have orthogonal lattice vectors unlike the integer-multiple-of-the-unit-cell ones. The space group is Pm(6). The same supercells were also used to produce wavefunction isosurface figures shown in Fig. 5.10. Trigonal $2 \times 2 \times 2$, $3 \times 3 \times 3$ and $4 \times 4 \times 4$ supercells with space group P3m1 (156) were used in formation energy and transition level calculations. These supercells have 32, 108 and 256 atoms respectively. We know from the discussion in Chapter 3, the energy contribution due to the periodic boundary condition of a supercell is inversely proportionate to the cube-root of the supercell volume (length dimension of supercell). Hence the dimension parameter L in Eqn. 4.18 can be taken as 2, 3 and 4 for the supercells $2 \times 2 \times 2$, $3 \times 3 \times 3$ and $4 \times 4 \times 4$ respectively.

A high k-point density was necessary to obtain converged total energies for metallic states. A $6 \times 6 \times 6$ Monkhorst-Pack net was used for self-consistent field calculations; a denser $12 \times 12 \times 12$ net was used for total energy evaluations. However for a $4 \times 4 \times 4$ supercell lower k-point densities, $4 \times 4 \times 4$ and $8 \times 8 \times 8$ had to be used to keep the computational expense affordable.

Tolerances for lattice sum convergence within the CRYSTAL program were chosen to be 8, 8, 8, 8 and 16. Convergence of each calculation was observed, based on minimisation of total energy. A total energy minimisation tolerance of 10^{-7} Hartree (10^{-6} eV) was used throughout.

Fe_3O_4 (Magnetite) features an insulating state with a monoclinic crystal structure below Verwey transition temperature ($\sim 123\text{K}$). A monoclinic inverse-spinel ferrite structure was used with lattice parameters $a = 5.94 \text{ \AA}$, $b = 5.92 \text{ \AA}$, $c = 16.77 \text{ \AA}$, $\alpha = \gamma = 90.000^\circ$, $\beta = 90.2365^\circ$. A $4 \times 4 \times 4$ Monkhorst-Pack net was used for all calculation with magnetite. Lattice sum tolerances of 7, 7, 7, 7 and 14 were maintained throughout. Convergence of calculations observed down to 10^{-7} Hartree (10^{-6} eV) with respect to total energy.

Appendix B

Basis Sets

The Gaussian orbital basis sets are used in the CRYSTAL codes (Versions CRYSTAL03, CRYSTAL06 and CRYSTAL09 are used). These are all-electron basis sets describing the orbitals that generate the wavefunction and the density function to start the DFT SCF calculations. The basis set orbitals can be linearly combined with the wavefunction calculated at the end of each SCF cycle. The amount of mixing of the calculated and original (basis set) wavefunctions can be controlled for better convergence. A localized orbital basis set such as the ones used here are more useful than a plane-wave basis set since explicit Hartree-Fock exchange is involved in B3LYP exchange-correlation functional. We have discussed the criteria for choosing the basis sets in Chapter 3. These basis sets are tested for convergence and slightly modified in cases where slow convergence with large oscillations is observed. Convergence of the total energy to 10^{-7} Hartree was observed throughout. In the particular case of a vacancy defect system, a ghost basis is inserted in the place of the removed atom. A ghost basis is a function without a nuclear charge and zero electrons. This is an essential step for localised orbital basis as removal of an atomic basis creates an empty space and a part of real space inaccessible to any charge due to a lack of wavefunction. Substituting the atomic basis with a ghost basis allows the SCF calculation to reproduce the electronic density redistribution caused by the defect. The ghost basis function is essentially the same as the atom removed, but without any charge in it. A basis is required for defect calculations that will converge to the bulk atomic wavefunction quickly and also will be able to converge quick enough to the desired defect

wavefunction from a ghost basis. Both the O and Zn basis were modified for this purpose. The O - basis was used in several oxides and used as the standard basis for previous publications [36, 137].

The data provided here are the prefactors and exponents of Gaussian functions of the form given by,

$$\Psi(\mathbf{r}) = \sum_i C_i e^{a_i(\mathbf{r}-\mathbf{r}_A)^2} \quad (\text{B.1})$$

The exponents a_i 's and the prefactors C_i 's are the elements of the 1st and 2nd columns respectively of the i-th row of the tables given below. \mathbf{r}_A is the atomic position.

Lithium(Li)

Basis set generated by Civalleri *et al* [186].

3	2			
0	0	6	2.	1.
	840.0	0.00264		
	217.5	0.00850		
	72.3	0.0335		
	19.66	0.1824		
	5.044	0.6379		
	1.5	1.0		
0	1	1	1.	1.
	0.510	1.0	1.0	

Carbon (C)

Basis set generated by Gatti *et al* [187].

6	4			
0	0	6	2.0	1.0
	.3047524880D+04	.1834737130D-02		
	.4573695180D+03	.1403732280D-01		
	.1039486850D+03	.6884262220D-01		
	.2921015530D+02	.2321844430D+00		
	.9286662960D+01	.4679413480D+00		
	.3163926960D+01	.3623119850D+00		
0	1	3	4.0	1.0
	.7868272350D+01	-.1193324200D+00	.6899906660D-01	
	.1881288540D+01	-.1608541520D+00	.3164239610D+00	
	.5442492580D+00	.1143456440D+01	.7443082910D+00	
0	1	1	0.0	1.0
	.1687144782D+00	.1000000000D+01	.1000000000D+01	
0	3	1	0.0	1.0
	.8000000000D+00	.1000000000D+01		

Nitrogen (N)

Basis set Generated by Gatti *et al* [187].

7	4			
0	0	6	2.0	1.0
	0.417351E+04	0.183477D-02		
	0.627458E+03	0.139946D-01		
	0.142902E+03	0.685866D-01		
	0.402343E+02	0.232241E+00		
	0.128202E+02	0.469070E+00		
	0.439044E+01	0.360455E+00		
0	1	3	5.0	1.0
	0.116264E+02	-0.114961E+00	0.675797D-01	
	0.271628E+01	-0.169117E+00	0.323907E+00	
	0.772218E+00	0.114585E+01	0.740895E+00	
0	1	1	0.0	1.0
	0.212031E+00	0.100000E+01	0.100000E+01	
0	3	1	0.0	1.0
	0.800000E+00	0.100000E+01		

Oxygen (O)

Basis set generated by Towler *et al* [188].

8	4			
0	0	8	2.0	1.0
	8020.0	0.00108		
	1338.0	0.00804		
	255.4	0.05324		
	69.22	0.1681		
	23.90	0.3581		
	9.264	0.3855		
	3.851	0.1468		
	1.212	0.0728		
0	1	4	7.0	1.0
	49.43	-0.00883	0.00958	
	10.47	-0.0915	0.0696	
	3.235	-0.0402	0.2065	
	1.217	0.379	0.347	
0	1	1	0.0	1.0
	0.4764	1.0	1.0	
0	1	1	0.0	1.0
	0.1802	1.0	1.0	

Magnesium (Mg)

Basis set generated by McCarthy *et al* [189].

12	6			
0	0	8	2.0	1.0
	68370.0	0.0002226		
	9661.0	0.001901		
	2041.0	0.011042		
	529.6	0.05005		
	159.17	0.1690		
	54.71	0.36695		
	21.236	0.4008		
	8.719	0.1487		
0	1	5	8.0	1.0
	143.7	-0.00671	0.00807	
	31.27	-0.07927	0.06401	
	9.661	-0.08088	0.2092	
	3.726	0.2947	0.3460	
	1.598	0.5714	0.3731	
0	1	1	0.0	1.0
	1.297	1.0	1.0	
0	1	1	2.0	1.0
	0.688	1.0	1.0	
0	1	1	0.0	1.0
	0.28	1.0	1.0	
0	3	1	0.0	1.0
	0.500	1.0		

Alluminum (Al)

Basis set generated by Catti *et al* [190].

13	6			
0	0	8	2.0	1.0
	70510.0	0.000226		
	10080.0	0.0019		
	2131.0	0.0110		
	547.5	0.0509		
	163.1	0.1697		
	54.48	0.3688		
	19.05	0.3546		
	5.402	0.0443		
0	1	5	8.0	1.0
	139.6	-0.01120	0.0089	
	32.53	-0.1136	0.0606	
	10.23	-0.0711	0.1974	
	3.810	0.5269	0.3186	
	1.517	0.7675	0.2995	
0	1	1	0.0	1.0
	1.21	1.0	1.0	
0	1	1	2.0	1.0
	0.59	1.0	1.0	
0	1	1	1.0	1.0
	0.15	1.0	1.0	
0	3	1	0.0	1.0
	0.51	1.0		

Iron (Fe)

Basis set generated by Catti *et al* [191].

26	7			
0	0	8	2.0	1.0
	315379.0	0.000227		
	45690.0	0.0019		
	9677.3	0.0111		
	2520.88	0.0501		
	759.746	0.1705		
	262.964	0.36924		
	102.801	0.4033		
	42.9733	0.1434		
0	1	6	8.0	1.0
	798.262	-0.0052	0.00850	
	191.162	-0.068	0.0608	
	63.6885	-0.1314	0.2114	
	25.3625	0.2517	0.3944	
	10.7338	0.6433	0.398	
	3.764	0.2825	0.2251	
0	1	4	8.0	1.0
	48.1434	0.0122	-0.0215	
	17.4579	-0.2278	-0.085	
	6.9972	-0.8801	0.201	
	3.0791	0.9755	1.3024	
0	1	1	0.0	1.0
	1.3137	1.0	1.0	
0	1	1	0.0	1.0
	0.5625	1.0	1.0	
0	3	4	5.0	1.0
	30.4821	0.0583		
	8.692	0.2591		
	3.1008	0.5162		
	1.1709	0.5656		
0	3	1	0.0	1.0
	0.4345	1.0		

Cobalt (Co)

Basis set generated by Dovesi *et al* [192].

27	7			
0	0	8	2.0	1.0
	341701.0	0.000227		
	48850.0	0.001929		
	10400.9	0.0111		
	2718.99	0.0501		
	819.661	0.1705		
	283.878	0.3692		
	111.017	0.4033		
	46.4757	0.1433		
0	1	6	8.0	1.0
	855.558	-0.0054	0.0088	
	206.504	-0.0684	0.062	
	69.0516	-0.1316	0.2165	
	27.2653	0.2616	0.4095	
	11.5384	0.6287	0.3932	
	4.2017	0.2706	0.225	
0	1	4	8.0	1.0
	51.5542	0.0182	-0.0287	
	18.9092	-0.2432	-0.0937	
	7.7251	-0.849	0.2036	
	3.5428	0.8264	1.4188	
0	1	1	0.0	1.0
	1.4914	1.0	1.0	
0	1	1	0.0	1.0
	0.6031	1.0	1.0	
0	3	4	7.0	1.0
	29.9009	0.0617		
	8.1164	0.2835		
	2.6433	0.529		
	0.8869	0.4976		
0	3	1	0.0	1.0
	0.3011	1.0		

Zinc (Zn)

Basis set generated by Jaffe *et al* [193].

30	8			
0	0	8	2.0	1.0
	417016.5	0.00023		
	60504.2	0.00192		
	12907.9	0.01101		
	3375.74	0.04978		
	1018.11	0.16918		
	352.55	0.36771		
	138.19	0.40244		
	57.851	0.14386		
0	1	6	8.0	1.0
	1079.2	-0.00620	0.00889	
	256.52	-0.07029	0.06384	
	85.999	-0.13721	0.22039	
	34.318	0.26987	0.40560	
	14.348	0.59918	0.41370	
	4.7769	0.32239	0.34974	
0	1	4	8.0	1.0
	60.891	0.00679	-0.00895	
	25.082	-0.08468	-0.03333	
	10.620	-0.34709	0.08119	
	4.3076	0.40633	0.56518	
0	1	1	0.0	1.0
	1.6868	1.0	1.0	
0	1	1	0.0	1.0
	0.62679	1.0	1.0	
0	1	1	0.0	1.0
	0.15033	1.0	1.0	
0	3	4	10.0	1.0
	57.345	0.02857		
	16.082	0.15686		
	5.3493	0.38663		
	1.7548	0.47766		
0	3	1	0.0	1.0
	0.51592	1.0		

References

- [1] S. M. Hu *Mater. Sci. Eng.*, vol. R13, p. 105, 1994. 1
- [2] H. Bracht *Mater. Res. Bull.*, vol. 25, p. 22, 2000. 1
- [3] F. Matsukura, H. Ohno, A. Shen, and Y. Sugawara, "Transport properties and origin of ferromagnetism in GaMnAs," *Phys. Rev. B*, vol. 57, p. R2037, 1998. 1
- [4] S. Guha, J. M. Depuydt, and M. A. Hasse *Appl. Phys. Lett.*, vol. 63, p. 3107, 1993. 1
- [5] D. C. Look, "Progress in ZnO materials and devices," *J. Elec. Mater.*, vol. 35, no. 6, p. 1299, 2006. 1, 5, 9, 15, 23, 47, 64, 75
- [6] Y. Alivov, J. E. Van Nostrand, D. C. Look, M. V. Chukichev, and B. M. Ataev, "Observation of 430 nm electroluminescence from ZnO/GaN hetero-junction light-emitting deodes.," *Appl. Phys. Lett.*, vol. 83, p. 2943, 2003. 1, 9
- [7] A. Nakamura, T. Ohashi, K. Yamamoto, J. Ishihara, T. Aoki, J. Temmyo, and H. Gotoh *Appl. Phys. Lett.*, vol. 90, p. 093512, 2007. 1
- [8] Y. Ryu, T.-S. Lee, J. A. Lubguban, H. W. White, B. J. Kim, Y. S. Park, and C. J. Youn *Appl. Phys. Lett.*, vol. 88, p. 241108, 2006. 1
- [9] C. Yuen, S. F. Yu, E. S. P. Leong, H. Y. Yang, S. P. Lau, N. S. Chen, and H. H. Hng, "Low-loss and directional output ZnO thin-film ridge waveguide random lasers with MgO capped layer," *Appl. Phys. Lett.*, vol. 86, p. 031112, 2005. 1

-
- [10] J. W. Fergus *J. Mater. Science*, vol. 38, p. 4259, 2003. 1
- [11] Y. W. Heo, D. P. Norton, and S. J. Pearton, "Origin of green luminescence in ZnO film grown by molecular beam epitaxy," *J. Appl. Phys.*, vol. 98, p. 073502, 2005. 1, 5, 9, 15, 23, 27, 61, 67, 91, 92
- [12] T. Dietl, H. Ohno, F. Matsukura, J. Cibert, and D. Ferrand *Science*, vol. 287, p. 1019, 2000. 1, 3, 28, 76, 110
- [13] K. Sato and H. Katayama-Yoshida, "First principles materials design for semiconductor spintronics," *Semicond. Sci. Technol.*, vol. 17, p. 367, 2002. 1, 3, 110
- [14] K. R. Kittilstved, N. S. Norberg, and D. R. Gamelin, "Chemical manipulation of high T_C ferromagnetism in ZnO dms," *Phys. Rev. Lett.*, vol. 94, p. 147209, 2005. 1, 28
- [15] J. M. D. Coey, M. Venkatesan, and C. B. Fitzgerald, "Donor impurity band exchange in dilute ferromagnetic oxides," *Nat. Mater.*, vol. 4, p. 173, 2005. 1, 5, 6, 16, 28, 29, 30, 33, 62, 67, 79, 110
- [16] T. Dietl *Nature*, vol. 2, p. 646, 2003. 1
- [17] M. Venkatesan, C. B. Fitzgerald, J. G. Lunney, and J. M. D. Coey, "Anisotropic ferromagnetism in substituted zinc oxide," *Phys. Rev. Lett.*, vol. 93, p. 177206, 2004. 1, 5, 7, 16, 21, 48, 61, 62, 64, 79, 110
- [18] N. H. Hong, J. Sakai, and V. Brizé, "Observation of ferromagnetism at room temperature in ZnO thin films," *J. Phys. Condens. Matter*, vol. 19, p. 036219, 2007. 2, 5, 16, 28, 33, 62, 66
- [19] N. H. Hong, J. Sakai, and F. Gervais, "Magnetism due to oxygen vacancies and/or defects in undoped semiconducting and insulating oxide thin films," *J. Magn. Magn. Mater.*, vol. 316, p. 214, 2007. 2, 5, 16, 28, 66
- [20] T. C. Kaspar, T. Droubay, S. M. Heald, P. Nachimuthu, C. M. Wang, V. Shutthanandan, C. A. J. D. R. Gamelin, and S. A. Chambers, "Lack of

REFERENCES

- ferromagnetism in n-type cobalt-doped ZnO epitaxial thin films,” *New J. Phys.*, vol. 10, p. 055010, 2008. 2, 6, 79
- [21] R. M. Nieminen, “Issues in first-principles calculations for defects in semiconductors and oxides,” *Modelling Simul. Mater. Sci. Eng.*, vol. 17, p. 084001, 2009. 2, 15, 25, 28, 55, 57
- [22] W. Kohn and L. J. Sham *Phys. Rev.*, vol. 140, p. A1133, 1965. 3, 38, 39
- [23] M. P. Allen and D. J. Tildesley, *Computer Simulation of Liquids*. Oxford University Press, 1987. 3, 35
- [24] B. T. Thole, P. Carra, F. Sette, and G. van der Laan, “X-ray circular dichroism as a probe of orbital magnetization,” *Phys. Rev. Lett.*, vol. 68, pp. 1943–1946, Mar 1992. 3, 35
- [25] S. Bhattacharya, C. Majumdar, and G. P. Das, “3d Transition metal decorated B-C-N composite nanostructures for efficient hydrogen storage: A first-principles study,” *Bull. Mater. Sci.*, vol. 32, no. 3, p. 353, 2009. 3
- [26] S. Baroni and R. Resta, “Ab initio calculation of the macroscopic dielectric constant in silicon,” *Phys. Rev. B*, vol. 33, no. 10, p. 7017, 1986. 3
- [27] Z. Q. Chen, S. J. Wang, M. Maekawa, A. Kawasuso, H. Naramoto, X. L. Yuan, and T. Sekiguchi, “Thermal evolution of defects in as-grown and electron-irradiated ZnO studied by positron annihilation,” *Phys. Rev. B*, vol. 75, p. 245206, 2007. 4, 39, 40
- [28] J. P. Pickett *Rev. Mod. Phys.*, vol. 61, p. 433, 1989. 4, 39, 40
- [29] V. I. Anisimov, S. Y. Ezhov, I. S. Elfimov, I. V. Solovyev, and T. M. Rice, “Singlet semiconductor to ferromagnetic metal transition in FeSi,” *Phys. Rev. Lett.*, vol. 76, no. 10, pp. 1735–1738, 1996. 4, 39, 40
- [30] J. P. Perdew, K. Burke, and M. Ernzerhof, “Generalized Gradient approximation made simple,” *Phys. Rev. Lett.*, vol. 77, p. 3865, 1996. 4, 26, 41

- [31] H. J. Kulik, M. Cococcioni, D. A. Scherlis, and N. Marzari, "Density functional theory in transition-metal chemistry: A self-consistent hubbard u approach," *Phys. Rev. Lett.*, vol. 97, p. 103001, Sep 2006. 4
- [32] L. Hedin *Phys. Rev.*, vol. 139, p. A796, 1965. 4
- [33] J. Heyd, G. E. Scuseria, and M. Ernzerhof, "Hybrid functionals based on a screened coulomb potential," *J. Chem. Phys.*, vol. 118, p. 8207, 2003. 4, 27, 41, 85
- [34] A. D. Becke *J. Chem. Phys.*, vol. 98, p. 5648, 1993. 4, 26, 27, 40
- [35] P. J. Stephens, F. J. Devlin, C. F. Chabalowski, and M. J. Frisch *J. Phys. Chem.*, vol. 98, p. 11623, 1994. 4
- [36] C. H. Patterson, "Role of defects in ferromagnetism in $\text{Zn}_{1-x}\text{Co}_x\text{O}$: a hybrid density functional calculation," *Phys. Rev. B*, vol. 74, p. 144432, 2006. 4, 6, 7, 17, 22, 26, 27, 39, 40, 41, 62, 66, 84, 85, 110, 131
- [37] R. L. Martin and F. Illas, "Antiferromagnetic exchange interactions from hybrid DFT," *Phys. Rev. Lett.*, vol. 79, p. 1539, 1997. 4, 41
- [38] F. Cora, M. Alfredsson, G. Mallia, D. S. Middlemiss, W. C. Mackrodt, R. Dovesi, and R. Orlando, "The performance of hybrid density functionals in solid state chemistry," *Structure and Bonding*, vol. 113, pp. 171–232, 2004. 4, 40, 41, 84
- [39] A. Chakrabarty and C. H. Patterson, "Defect-trapped electrons and ferromagnetic exchange in ZnO ," *Phys. Rev. B*, vol. 84, p. 054441, 2011. 4, 7, 15, 17, 22, 41
- [40] X. L. Wu, G. G. Siu, C. L. Fu, and H. C. Ong *Appl. Phys. Lett.*, vol. 78, p. 2285, 2001. 5, 23, 93
- [41] L. S. Vlasenko and G. D. Watkins, "Optical detection of EPR in RT electron irradiated ZnO ," *Phys. Rev. B*, vol. 71, p. 125210, 2005. 5, 15, 17, 18

-
- [42] C. Sudakar, P. Kharel, G. Lawes, R. Suryanarayanan, R. Naik, and V. M. Naik, "Raman spectroscopic studies of oxygen defects in Co-doped ZnO films exhibiting room temperature ferromagnetism," *J. Phys. Cond. Mat.*, vol. 19, p. 026212, 2007. 5, 6
- [43] K. R. Kittilstved and D. R. Gamelin, "Activation of high Tc ferromagnetism in Mn²⁺-doped ZnO using amines," *J. Am. Chem. Soc.*, vol. 127, p. 5292, 2005. 5, 6, 33, 62, 64
- [44] A. J. Behan, A. Mokhtari, H. J. Blythe, D. Score, X.-H. Xu, J. R. Neal, A. M. Fox, and G. A. Gehring, "Two Magnetic Regimes in Doped ZnO Corresponding to a Dilute Magnetic Semiconductor and a Dilute Magnetic Insulator," *Phys. Rev. Lett.*, vol. 100, p. 047206, 2008. 6, 16, 61, 80, 110
- [45] C. D. Pemmaraju, R. Hanafin, T. Archer, and S. Sanvito, "Impurity-Ion pair induced high-temperature ferromagnetism in Co-doped ZnO," *Phys. Rev. B*, vol. 78, p. 054428, 2008. 6, 26, 30, 64, 79
- [46] M. Venkatesan, C. B. Fitzgerald, and J. M. D. Coey, "Ferromagnetism in HfO₂," *Nature*, vol. 430, p. 630, 2004. 6
- [47] N. H. Hong, J. Sakai, N. Poirot, and V. Brize, "Room temperature ferromagnetism observed in undoped semiconducting and insulating oxide thin films," *Phys. Rev. B*, vol. 73, p. 132404, 2006. 6
- [48] M. M. Cruz, R. C. da Silva, N. Franco, and M. Godinho, "Ferromagnetism induced in rutile single crystals by argon and nitrogen implantation," *J. Phys. Cond. Mat.*, vol. 21, p. 206002, 2009. 6
- [49] N. H. Hong, N. Poirot, and J. Sakai, "Ferromagnetism observed in pristine SnO₂ thin films," *Phys. Rev. B*, vol. 77, p. 033205, 2008. 6
- [50] R. C. Barklie (*Private Communications*). 6, 18, 19, 61
- [51] R. C. Barklie and S. Wright, "EPR of defects in HfO₂ and ZrO₂ powders and films," *J. vac. Sci. Technol. B*, vol. 27, p. 317, 2009. 6

- [52] S. Wright and R. C. Barklie, "EPR characterization of defects in m-HfO₂," *J. Mater. Science*, vol. 18, p. 743, 2007. 6, 19
- [53] A. Zubiaga, F. Plazaola, J. Garcia, F. Tuomisto, V. Munoz-Sanjose, and R. tena Zaera, "Positron annihilation lifetime spectroscopy of ZnO bulk samples," *Phys. Rev. B*, vol. 76, p. 85202, 2007. 6, 61, 62
- [54] J. Schulman and W. Compton, *Color centers in solids*. Pergamon, 1962. 6
- [55] E. Seebauer and M. Kratzer, *Charged Semiconductor Defects, Structure, Thermodynamics and Diffusion*. Springer, 2009. 6, 7, 12, 13, 15, 16, 24, 59, 62, 67
- [56] "Data in Science and Technology; Semiconductors Other than Group IV Elements and III-V Compounds, O. Madelung, Ed.," 6, 9, 27, 41, 90, 108, 128
- [57] A. Janotti and C. G. V. de Walle, "Fundamentals of zinc oxide as a semiconductor," *Rep. Prog. Phys.*, vol. 72, p. 126501, 2009. 6
- [58] D. C. Look and B. Clafin, "p-type doping and devices based on ZnO," *Phys. Stat. Sol.*, vol. 241, p. 624, 2004. 6
- [59] A. Walsh, J. L. D. Silva, and S.-H. Wei, "Theoretical Description of Carrier Mediated Magnetism in Cobalt Doped ZnO," *Phys. Rev. Lett.*, vol. 100, p. 256401, 2008. 6, 79, 110, 111
- [60] H. Raebiger, S. Lany, and A. Zunger, "Electronic structure, donor and acceptor transitions and magnetism of 3d impurities in In₂O₃ and ZnO," *Phys. Rev. B*, vol. 79, p. 165202, 2009. 6
- [61] J. Hubbard *Proc. Roy. Soc. A*, vol. 276, p. 238, 1963. 7, 8, 30, 32
- [62] F. A. Selim, M. H. Weber, D. Solodovnikov, and K. G. Lynn, "Nature of Native Defects in ZnO," *Phys. Rev. Lett.*, vol. 99, p. 085502, 2007. 7, 18, 21, 23, 61, 62, 67

REFERENCES

- [63] F. Oba, A. Togo, I. Tanaka, J. Paier, and G. Kresse, "Defect energetics in ZnO: A hybrid Hartree-Fock density functional study," *Phys. Rev. B*, vol. 77, p. 245202, 2008. 7, 15, 25, 27, 84, 85, 93
- [64] A. F. Kohan, G. Ceder, D. Morgan, and C. G. V. de Walle, "First principles study of native point defects in ZnO," *Phys. Rev. B*, vol. 61, p. 15019, 2000. 7, 8, 15, 17, 22, 24, 25, 26, 27, 39, 57, 62, 64, 66, 84, 85, 91
- [65] D. Ricci, G. Pacchioni, P. V. Sushko, and L. Shluger, "Electron trapping at neutral divacancy sites on MgO surface," *J. Chem. Phys.*, vol. 117, no. 6, p. 2844, 2002. 8, 15, 19, 20, 108
- [66] M. Kapilashrami, J. Xu, K. V. Rao, L. Belova, E. Carlegrim, and M. Fahlman, "Experimental evidence for ferromagnetism at room temperature in MgO thin films," *J. Phys. Cond. Mat.*, vol. 22, p. 345004, 2010. 8, 108
- [67] J. A. Henderson, J. Oitmaa, and M. C. B. Ashley, "High temperature expansion for the single band hubbard model," *Phys. Rev. B*, vol. 46, p. 6328, 1992. 9, 33, 109
- [68] J. Wahle, N. Blümer, J. Schlipf, K. Held, and D. Vollhardt, "Microscopic conditions favoring itinerant ferromagnetism," *Phys. Rev. B*, vol. 58, p. 12749, 1998. 9, 33, 109
- [69] S. Lany and A. Zunger *Phys. Rev. B*, vol. 72, p. 035215, 2005. 9, 25, 91, 92, 97
- [70] S. Lany and A. Zunger, "Dopability, intrinsic conductivity and non-stoichiometry of transparent conducting oxides," *Phys. Rev. Lett.*, vol. 98, p. 045501, 2007. 9, 56, 64
- [71] F. Gallino, G. Paccioni, and C. D. Valentin, "Transition levels of defect centers in ZnO by hybrid functionals and localized basis set approach," *J. Chem. Phys.*, vol. 133, p. 144512, 2010. 9, 54, 92, 93, 94

- [72] C. Freysoldt, J. Neugebauer, and C. V. de Walle, "Fully ab-initio finite-size corrections for charged-defect supercell calculations," *Phys. Rev. Lett.*, vol. 102, p. 016402, 2009. 10, 57
- [73] J. P. Wright, J. P. Attfield, and P. G. Radaelli *Phys. Rev. B*, vol. 66, p. 214422, 2002. 10, 114, 115, 116
- [74] E. J. W. Verwey *Nature*, vol. 144, p. 327, 1939. 10, 114
- [75] M. Iizumi, T. F. Koetzle, G. Shirane, S. Chikazumi, M. Matsui, and S. Todo *Acta Crystallogr., Sect. B: Struct. Crystallogr. Cryst. Chem.*, vol. B38, p. 2121, 1982. 10, 114
- [76] M. Bimbi, G. Allodi, R. D. Renzi, C. Mazzoli, and H. Berger, "Muon spin spectroscopy evidence of a charge density wave in magnetite below the verwey transition," *Phys. Rev. B*, vol. 77, p. 45115, 2008. 10, 114, 116
- [77] J. P. Wright, J. P. Attfield, and P. G. Radaelli *Phys. Rev. Lett.*, vol. 87, p. 266401, 2001. 10, 114, 115, 116
- [78] S. F. Alvarado, W. Eib, F. Meier, D. T. Pierce, K. Sattler, H. C. Siegmann, and J. O. Remeika *Phys. Rev. Lett.*, vol. 34, p. 6319, 1975. 10, 115
- [79] R. Gunning *14th International Conference on Solid Films and Surfaces*, 2008. 10, 118
- [80] F. A. Kroger and H. J. Vink *Solid St. Phys. Adv. Res. Appl.*, vol. 3, p. 307, 1956. 13
- [81] J. Maier *Prog. Solid State Chem.*, vol. 23, p. 171, 1995. 13
- [82] K. L. Duncan and E. D. Wachsman *Ionics*, vol. 13, no. 127, 2007. 14
- [83] R. A. Huggins *Solid State Ionics*, vol. 143, no. 3, 2001. 14
- [84] H. L. Tuller and S. R. Bishop, "Tailoring material properties through defect engineering," *Chem. Lett.*, vol. 39, p. 1226, 2010. 15

- [85] H. H. Rose, "Optics of high performance electron microscopes," *Sci. Technol. Adv. Mater.*, vol. 9, no. 1, p. 014107, 2008. 15
- [86] D. C. Look, J. W. Hemsky, and J. R. Sizelove, "Residual native shallow donor in ZnO," *Phys. Rev. Lett.*, vol. 82, p. 2552, 1999. 15
- [87] D. C. Look, G. C. Farlow, P. Reunchan, S. Limpijumnong, S. B. Zhang, and K. Nordlund, "Evidence for native defect donors in n-type ZnO," *Phys. Rev. Lett.*, vol. 95, p. 225502, 2005. 15, 61
- [88] S. Wright and R. C. Barklie, "EPR characterization of defects in m-HfO₂ and ZrO₂ powders," *J. Appl. Phys.*, vol. 106, p. 103917, 2009. 15, 18, 19
- [89] F. Tuomisto, V. Ranki, K. Saarinen, and D. C. Look, "Evidence of the zn vacancy acting as the dominant acceptor in n-type ZnO," *Phys. Rev. Lett.*, vol. 91, p. 205502, 2003. 15, 21, 22, 87
- [90] A. Janotti and C. G. V. de Walle, "Native point defects in ZnO," *Phys. Rev. B*, vol. 76, p. 165202, 2007. 15, 19, 40, 84, 93
- [91] A. Zubiaga, F. Plazaola, J. Garcia, F. Tuomisto, V. Munoz-Sanjose, and R. Tena-Zaera, "Positron annihilation lifetime spectroscopy of ZnO bulk samples," *Phys. Rev. B*, vol. 76, p. 85202, 2007. 15, 22, 68
- [92] G. Bouzerar and T. Ziman, "Model for vacancy-induced d0 ferromagnetism in oxide compounds," *Phys. Rev. Lett.*, vol. 96, p. 207602, 2006. 16, 28, 33
- [93] A. Kaminski and S. D. Sarma, "Polaron percolation in diluted magnetic semiconductors," *Phys. Rev. Lett.*, vol. 88, p. 247202, 2002. 16, 28, 29
- [94] Y. Kim and S. Kang *J. Phys. Chem.*, vol. 114, no. 7874, 2010. 16
- [95] C. Kittel *Phys. Rev.*, vol. 71, p. 270, 1948. 17
- [96] L. S. Vlasenko and G. D. Watkins, "Optical detection of EPR for intrinsic defects produced in ZnO by 2.5 MeV electron irradiation in situ at 4.2K," *Phys. Rev. B*, vol. 72, p. 035203, 2005. 17, 18, 19

-
- [97] J. M. Smith and W. E. Vehse, "A search for ferromagnetism in TM doped piezoelectric ZnO," *Phys. Lett.*, vol. 31A, p. 147, 1970. 17
- [98] Y. V. Gorelkinskii and G. D. Watkins, "Defects produced in zno by 2.5 mev electron irradiation at 4.2k: study by odepr," *Phys. Rev. B*, vol. 69, p. 115212, 2004. 17
- [99] J. E. Wentz, J. W. Orton, and P. Auzins, "ESR studies of radiation effects in inorganic solids," *Disc. Far. Soc.*, vol. 31, p. 140, 1961. 18, 19
- [100] K.-C. To, A. M. Stoneham, and B. Henderson, "ESR from a vacancy pair center in MgO," *Phys. Rev.*, vol. 181, p. 1237, 1969. 18, 19
- [101] D. Galland and A. Hervé *Phys. Lett.*, vol. 33A, p. 1, 1970. 18
- [102] W. E. Carlos, E. R. Glaser, and D. C. Look, "Magnetic resonance studies of ZnO," *Physica B*, vol. 308-310, p. 976, 2001. 19
- [103] A. Dupasquier and A. M. Jr., eds., *Positron Spectroscopy of Solids*. IOS Press, Amsterdam, 1995. 21
- [104] F. Tuomisto, K. Saarinen, D. C. Look, and G. C. Farlow, "Introduction and recovery of point defects in electron-irradiated ZnO," *Phys. Rev. B*, vol. 72, p. 085206, 2005. 21, 22, 29, 87
- [105] A. Zubiaga, F. Tuomisto, V. A. Coleman, and C. Jagadish *Appl. Surf. Sci.*, vol. 255, p. 234, 2008. 21, 22
- [106] S. A. Studenikin and M. Cocivera *J. Appl. Phys.*, vol. 91, p. 5060, 2002. 23, 93
- [107] M. Liu, A. Kitai, and P. Mascher *J. Lumin.*, vol. 54, p. 35, 1992. 23
- [108] M. Mikami, T. Eto, J. Wang, and Y. M. M. Isshiki *J. Cryst. Growth*, vol. 276, p. 389, 2005. 23
- [109] D. Reynolds, D. C. Look, and B. Jogai *J. Appl. Phys.*, vol. 89, p. 6189, 2001. 23

-
- [110] Y. G. Wang, S. P. Lau, X. H. Zhang, H. W. L. ad S. F. Yu, B. K. Tay, and H. H. Hng *Chem. Phys. Lett.*, vol. 375, p. 113, 2003. 23
- [111] R. Vidya, P. Ravindran, H. Fjellvag, B. Svensson, E. Monakhov, M. Ganchenkova, and R. Nieminen *Phys. Rev. B*, vol. 83, p. 045206, 2011. 23, 25, 27, 91, 92, 93
- [112] P. Rinke, A. Qteish, D. Bimberg, J. Neugebauer, and M. Scheffler, “Exciting prospects for solids: Exact-exchange based functionals meet quasiparticle energy,” *Physica Status Solidi (b)*, vol. 245, no. 5, p. 929, 2008. 25
- [113] A. Liechtenstein, V. I. Anisimov, and J. Zaanen *Phys. Rev. B.*, vol. 52, p. R54667, 1995. 26
- [114] V. I. Anisimov, I. S. Elfimov, N. Hamada, and K. Terakura *Phys. Rev. B*, vol. 54, p. 4387, 1996. 26
- [115] J. P. Perdew and A. Zunger, “Self-interaction correction to density functional approximations for many-electron systems,” *Phys. Rev. B*, vol. 23, p. 5048, 1981. 26
- [116] P. Rinke, A. Janotti, A. Scheffler, and C. V. de Walle *Phys. Rev. Lett.*, vol. 102, p. 026402, 2009. 26
- [117] S. Lany and A. Zunger, “Assessment of correction methods for the band gap problem and for finite size effects in supercell defect calculations: ZnO and GaAs,” *Phys. Rev. B*, vol. 78, p. 235104, 2008. 26
- [118] C. V. de Walle and J. Neugebauer *J. Appl. Phys.*, vol. 95, p. 3851, 2004. 26, 48
- [119] L. Curtiss, K. Raghavachari, G. Trucks, and J. Pople *J. Chem. Phys.*, vol. 94, p. 7221, 1991. 27, 40
- [120] P. Agoston, K. Albe, R. M. Nieminen, and M. J. Puska *Phys. Rev. Lett.*, vol. 103, no. 245501, 2009. 27, 28

-
- [121] M. J. Calderon and S. D. Sarma *Annals of Physics*, vol. 322, p. 2618, 2007. 29
- [122] Y. Nagaoka, "Ferromagnetism in a narrow, almost half-filled s-band," *Phys. Rev.*, vol. 147, no. 1, p. 392, 1966. 32, 33, 109
- [123] T. Herrmann and W. Nolting, "Magnetism in the single band hubbard model," *J. Magn. Magn. Mater.*, vol. 170, p. 253, 1997. 33, 109
- [124] M. Ulmke, "Ferromagnetism in the Hubbard model on fcc-type lattices," *Eur. Phys. J. B*, vol. 1, p. 301, 1998. 33, 109
- [125] E. Nielsen and R. N. Bhatt, "Search for ferromagnetism in doped semiconductors in the absence of transition metal ions," *Phys. Rev. B*, vol. 82, p. 195117, 2010. 34, 109
- [126] L. Thomas, "The calculation of atomic fields," *Proc. Cambridge Phil. Soc.*, vol. 23, no. 5, p. 542, 1927. 35
- [127] E. Fermi *Rend. Accad. Naz. Lincei*, vol. 6, no. 602, 1927. 35
- [128] P. Hohenberg and W. Kohn *Phys. Rev.*, vol. 12, p. 69, 1964. 35, 38
- [129] M. Nolan, "Defects in Cu_2O , CuAlO_2 and SrCu_2O_2 ," *Thin Solid Films*, vol. 516, no. 22, p. 8130, 2008. 39
- [130] C. Lee, W. Yang, and R. G. Parr *Phys. Rev. B*, vol. 37, p. 785, 1988. 40
- [131] S. H. Vosko, L. Wilk, and M. Nusair *Can. J. Phys.*, vol. 58, p. 1200, 1980. 40
- [132] X. Feng, "Electronic structures and ferromagnetism of Cu and Mn doped ZnO ," *J. Phys. Condens. Matt.*, vol. 16, p. 4251, 2004. 40, 41, 84
- [133] A. D. Becke *J. Chem. Phys.*, vol. 98, p. 5648, 1998. 40
- [134] X.-B. Feng and N. M. Harrison, "Electronic structure of CaCuO_2 from the b3lyp hybrid density functional," *Phys. Rev. B*, vol. 69, p. 132502, 2004. 40

-
- [135] M. Neef, K. Doll, and G. Zwicknagl *J. Phys. Cond. Mat.*, vol. 18, p. 7437, 2006. 40
- [136] F. Pascale, C. Zicovich-Wilson, F. Lopez, B. Civalleri, R. Orlando, and R. Dovesi, "The calculation of the vibration frequencies of crystalline compounds and its implementation in the crystal code," *J. Comput. Chem.*, vol. 25, p. 888, 2004. 40
- [137] A. D. Rowan, C. H. Patterson, and L. V. Gasparov, "Hybrid density functional theory applied to magnetite: Crystal structure, charge order and phonons," *Phys. Rev. B*, vol. 79, p. 205103, 2009. 40, 41, 42, 116, 121, 131
- [138] N. Kaltsoyannis and J. McGrady, *Principles and Applications of Density Functional Theory in Inorganic Chemistry I*. Springer, 2004. 41
- [139] J. Paier, M. Marsman, and G. Kresse, "Why does the B3LYP hybrid functional fail for metals," *J. Chem. Phys.*, vol. 127, no. 2, p. 024103, 2007. 41
- [140] J. Hafner *J. Comput. Chem.*, vol. 29, p. 2044, 2008. 41
- [141] J. Heyd, G. E. Scuseria, and M. Ernzerhof, "Erratum: hybrid functionals based on a screened coulomb potential," *J. Chem. Phys.*, vol. 124, p. 219906, 2006. 41
- [142] J. P. Perdew and Y. Wang *Phys. Rev. B*, vol. 45, p. 13244, 1992. 41
- [143] J. M. Seminario, *Recent Developments and Applications of Modern Density Functional Theory*. Elsevier, 1996. 41
- [144] J. K. Perry, J. Tahir-Kheli, and W. A. Goddard, "Antiferromagnetic band structure of La_2CuO_4 : B3LYP calculations," *Phys. Rev. B*, vol. 63, p. 144510, 2001. 41

- [145] I. D. R. Moreira and R. Dovesi, "Periodic approach to the electronic structure and magnetic coupling in KCuF_3 , K_2CuF_4 , and $\text{Sr}_2\text{CuO}_2\text{Cl}_2$ low-dimensional magnetic systems," *Int. J. Quant. Chem.*, vol. 99, p. 805, 2004. 41
- [146] C. H. Patterson, "Comparison of hybrid density functional, hartree-fock and GW calculations on NiO," *Int. J. Quant. Chem.*, vol. 106, p. 3383, 2006. 41
- [147] R. Dovesi, V. R. Saunders, C. Roetti, R. Orlando, C. M. Zicovich-Wilson, F. Pascale, B. Civalleri, K. Doll, N. M. Harrison, I. Bush, P. D'Arco, and M. Llunell, "Crystal06 user's manual, university of torino, torino," 2007. 42, 60, 128
- [148] H. Monkhorst and J. D. Pack *Phys. Rev. B*, vol. 13, p. 5188, 1976. 43
- [149] G. Kresse and J. Furthmüller *Phys. Rev. B*, vol. 54, p. 11169, 1996. 44
- [150] P. Giannozzi, S. Baroni, N. Bonini, M. Calandra, R. Car, C. Cavazzoni, D. Ceresoli, G. L. Chiarotti, M. Cococcioni, I. Dabo, A. Dal Corso, S. de Gironcoli, S. Fabris, G. Fratesi, R. Gebauer, U. Gerstmann, C. Gougoussis, A. Kokalj, M. Lazzeri, L. Martin-Samos, N. Marzari, F. Mauri, R. Mazzarello, S. Paolini, A. Pasquarello, L. Paulatto, C. Sbraccia, S. Scandolo, G. Sclauzero, A. P. Seitsonen, A. Smogunov, P. Umari, and R. M. Wentzcovitch, "Quantum espresso: a modular and open-source software project for quantum simulations of materials," *J. Phys. Cond. Mat.*, vol. 21, no. 39, p. 395502 (19pp), 2009. 44, 57, 127, 128
- [151] L. Turi and J. J. Dannenberg *J. Phys. Chem.*, vol. 97, p. 2488, 1993. 45
- [152] C. H. Patterson, "Exciton: A code for excitations in materials," *Mol. Phys.*, vol. 108, p. 3181, 2010. 45
- [153] A. Kokalj *Comp. Mater. Sci.*, vol. 28, p. 155, 2003. 46
- [154] J. A. Dean, *Lange's Handbook of Chemistry*. New York: McGraw-Hill, 14th edition ed., 1992. 49

REFERENCES

- [155] G. Makov and M. C. Payne, "Periodic boundary conditions in ab-initio calculations," *Phys. Rev. B*, vol. 51, p. 4014, 1995. 49, 56, 90, 100
- [156] J. F. Janak *Phys. Rev. B*, vol. 18, p. 7165, 1978. 52, 83
- [157] P. Gopal and N. A. Spaldin, "Magnetic interactions in transition-metal-doped ZnO: An ab initio study," *Phys. Rev. B*, vol. 74, p. 094418, 2006. 57, 64, 111
- [158] N. D. M. Hine, K. Frensch, W. M. Foulkes, and M. Finnis *Phys. Rev. B*, vol. 79, p. 024112, 2009. 57
- [159] H. Schlegel *Theoret. Chim. Acta*, vol. 66, p. 333, 1984. 59
- [160] P. Pulay *Mol. Phys.*, vol. 17, p. 197, 1969. 59
- [161] B. Civalleri, P. D'Arco, R. Orlando, V. Saunders, and R. Dovesi *Chem. Phys. Lett.*, vol. 348, p. 131, 2001. 59
- [162] C. Liu, F. Yun, and H. MorkoÁ, "Ferromagnetism of ZnO and GaN: A Review," *J. Mat. Sci.: Materials in Electronics*, vol. 16, p. 555, 2005. 62
- [163] H. Hsu, J. C. A. Huang, Y. H. Huang, Y. F. Liao, M. Z. Lin, C. H. Lee, J. F. Lee, S. F. Chen, L. Y. Lai, and C. P. Liu, "Evidence of oxygen vacancy enhanced room-temperature ferromagnetism in Co-doped ZnO," *Appl. Phys. Lett.*, vol. 88, p. 242507, 2006. 64
- [164] X.-C. Liu, E.-W. Shi, Z.-Z. Chen, B.-Y. Chen, T. Zhang, L.-X. Song, K.-J. Zhou, M.-Q. Cui, W.-S. Yan, Z. Xie, B. He, and S.-Q. Wei, "Effect of oxygen partial pressure on the local structure and magnetic properties of Co-doped ZnO films," *J. Phys. Cond. Mat.*, vol. 20, p. 025208, 2008. 64
- [165] M. Opel, K. W. Nielsen, S. Bauer, S. T. B. Goennenwein, J. C. Cezar, D. Schmeisser, J. Simon, and W. Mader, "Nanosized superparamagnetic precipitates in cobalt-doped ZnO," *Eur. Phys. J. B.*, vol. 63, p. 437, 2008. 79

-
- [166] P. Erhart, K. Albe, and A. Klein, "First-principles study of intrinsic point defects in ZnO: Role of band structure, volume relaxation, and finite-size effects," *Phys. Rev. B*, vol. 73, p. 205203, 2006. 84
- [167] S. B. Zhang, S. H. Wei, and A. Zunger, "Intrinsic n-type versus p-type doping asymmetry and the defect physics of ZnO," *Phys. Rev. B*, vol. 63, p. 075205, 2001. 84
- [168] S. Lany and A. Zunger *Phys. Rev. B*, vol. 93, p. 156404, 2004. 91
- [169] T. M. Borseth, B. Svensson, A. Y. Kuznetsov, P. Klason, Q. X. Zhao, and M. Willander *Appl. Phys. Lett.*, vol. 89, p. 262112, 2006. 92, 93
- [170] M. Khalid, A. Setzer, M. Ziese, P. Esquinazi, D. Spemann, A. Poppl, and E. Goering *Phys. Rev. B*, vol. 81, p. 214414, 2010. 108
- [171] T. Herrmann and W. Nolting, "Ferromagnetism in the Hubbard model: influence of the lattice structure," *Sol. St. Commun.*, vol. 103, p. 351, 1997. 109
- [172] T. Chanier, M. Sargolzaeia, I. Ophale, R. Hayn, and K. Koepernik *Phys. Rev. B*, vol. 73, p. 134418, 2006. 111, 112
- [173] F. Walz, "The Verwey Transition - a topical review," *J. Phys. Condens. Matter*, vol. 14, p. R285, 2002. 114
- [174] G. K. Rozenberg, M. P. Pasternak, W. M. Xu, Y. Amiel, M. Hanfland, M. Amboage, R. D. Taylor, and R. Jeanloz, "Origin of the verwey transition in magnetite," *Phys. Rev. Lett.*, vol. 96, p. 045705, 2006. 114, 115
- [175] D. J. Huang, H.-J. Lin, J. Okamoto, K. S. Chao, H.-T. Jeng, G. Y. Guo, C.-H. Hsu, C.-M. Huang, D. C. Ling, W. B. Wu, C. S. Yang, and C. T. Chen, "Charge-orbital ordering and verwey transition in magnetite measured by resonant soft x-ray scattering," *Phys. Rev. Lett.*, vol. 96, p. 096401, 2006. 114, 115, 116
- [176] P. Weiss *Ann. de Physique*, vol. 12, p. 279, 1929. 115

- [177] S. K. Park, T. Ishikawa, and Y. Tokura *Phys. Rev. B*, vol. 58, p. 3717, 1998. 115, 116
- [178] S. Lee, A. Fursina, J. Mayo, C. T. Yavuz, V. Colvin, R. Sofin, I. Shvets, and D. Natelson, "Electrically driven phase transition in magnetite nanostructures," *arXiv:0711.1869v1 [cond-mat.mtrl-sci]*, 2007. 115
- [179] A. Kozłowski, Z. Kakol, and Z. Tarnawski, "Magnetite: the correlated electron-phonon system," *Acta Physica polonica A.*, vol. 111, p. 537, 2007. 115
- [180] S. Ciuchi and S. Fratini *arXiv:0810.0397v1[cond-mat.str-el]*, 2008. 115
- [181] C. H. Patterson and A. D. Rowan, "Electronic structure and vibrational spectra of magnetite," *AIP Conference proceedings*, vol. 963, p. 371, 2007. 116
- [182] V. A. M. Brabers *The Handbook of Magnetic Materials (Chapter 3)*, vol. 8, 1995. 118
- [183] C. McGuinness (*Private Communications*). 122
- [184] C. J. Pickard and F. Mauri *Phys. Rev. Lett.*, vol. 88, p. 086403, 2002. 127
- [185] J. Tate, H. L. Ju, J. C. Moon, A. Zakutayev, A. P. Richard, J. Russell, and d. H. McIntyre, "Origin of p-type conduction in single-crystal CuAlO₂," *Phys. Rev. B.*, vol. 80, p. 165206, 2009. 127
- [186] B. Civalieri, A. Ferrari, M. Lluell, R. Orlando, M. Merawa, and P. Ugliengo, "Cation selectivity in alkali-exchanged chabazite: an ab-initio periodic study," *Chem. Mater.*, vol. 15, p. 3996, 2003. 131
- [187] C. R. C. Gatti, V.R. Saunders, "Crystal-field effects on the topological properties of the electron-density in molecular-crystals - the case of urea," *J. Chem. Phys.*, vol. 101, p. 10686, 1994. 132

-
- [188] M. D. Towler, N. L. Allan, N. M. Harrison, V. R. Saunders, W. C. Mackrodt, and E. Aprà, "Ab initio study of MnO and NiO," *Phys. Rev. B*, vol. 50, p. 5041, 1994. 133
- [189] M. I. McCarthy and N. M. Harrison, "Ab initio determination of the bulk properties of MgO," *Phys. Rev. B*, vol. 49, p. 8574, 1994. 134
- [190] M. Catti, G. Valerio, R. Dovesi, and M. Causa, "Quantum-mechanical calculations of the solid-state equilibrium $\text{MgO} + \alpha\text{-Al}_2\text{O}_3 \rightleftharpoons \text{MgAl}_2\text{O}_4$ (spinel) versus pressure," *Phys. Rev. B*, vol. 49, p. 14179, 1994. 135
- [191] M. Catti, G. Valerio, and R. Dovesi, "Theoretical study of electronic, magnetic and structural properties of $\alpha\text{-Fe}_2\text{O}_3$ (hematite)," *Phys. Rev. B*, vol. 51, p. 7441, 1995. 136
- [192] R. Dovesi, F. Freyria-Fava, C. Roetti, and V. R. Saunders, "Structural, electronic and magnetic properties of KMF_3 (M=Mn, Fe, Co, Ni)," *Faraday Disc.*, vol. 106, p. 173, 1997. 137
- [193] J. E. Jaffe and A. C. Hess, "HF study of phase changes in ZnO at high pressure," *Phys. Rev. B*, vol. 48, p. 7903, 1993. 138